Electron Transport and Performance Degradation in Novel Solar Technologies

By

DAVIS GUSTAV UNRUH

DISSERTATION

Submitted in partial satisfaction of the requirements for the degree of

DOCTOR OF PHILOSOPHY

in

PHYSICS

in the

OFFICE OF GRADUATE STUDIES

of the

UNIVERSITY OF CALIFORNIA

DAVIS

Approved:

Prof. Gergely T. Zimányi, Chair

Prof. Richard T. Scalettar

Prof. Dong Yu

Committee in Charge

2021

Contents

Electron Transport and Performance Degradation in Novel Solar Technologies

Abstract

While traditional c-Si solar cells still dominate the photovoltaic market, progress in further increasing their power conversion efficiencies or otherwise lowering operation costs has been relatively stagnant. As such, photovoltaic research focuses predominantly on novel solar technologies, also known as emerging solar technologies, each of which has demonstrated pathways toward a combination of high effiency and low cost which would allow them to supplant c-Si and change the solar technology landscape.

Two such novel solar technologies are nanoparticle and silicon heterojunction solar cells. The issues facing the widespread adoption of these two technologies are quite different. In nanoparticle solar cells, extraction of photogenerated carriers is inhibited by low carrier mobilities. Driving NP solids toward band-like transport is crucial to preventing electron/hole pairs from recombining before they can be collected. In contrast, silicon heterojunctions have already demonstrated very high conversion efficiencies, but exhibit high levels of unexplained performance degradation. Determining the degradation pathways and developing strategies for degradation minimization will be crucial to their widespread adoption.

This dissertation presents theoretical studies of both solar technologies. Beginning with NP solids, carrier transport studies are carried out in NP solids which examine the underlying physics governing transport, as well as determining the extent to which defects inhibit extended band-like transport. Continuing to silicon heterojunctions, comprehensive simulations model defect formation pathways and measure the corresponding energy barriers, in order to determine which pathways lead to the observed long-term degradation in these solar cells. The main chapters in this dissertation, apart from a section describing the NP simulation methods, are discussed briefly below.

First, we simulated electron transport across a binary nanocrystal solid (BNS) of PbSe NCs with diameters of 6.5nm and 5.1nm. We used our Hierarchical Nanoparticle Transport Simulator HINTS to model the transport in these BNSs. The mobility exhibits a minimum at a Large-NC-fraction $f_{\mathrm{LNC}} = 0.25$. The mobility minimum is deep at $T = 80$K and partially smoothed at $T = 300$K. We explain this minimum as follows. As the LNC fraction f_{LNC} starts growing from zero, the few

LNCs act as traps for the electrons traversing the BNS because their relevant energy level is lower. Therefore, increasing the f_{LNC} concentration of these traps decreases the mobility. As increasing f_{LNC} reaches the percolation threshold f_{LNC}=f_P, the LNCs form sample-spanning networks that enable electrons to traverse the entire BNS via these percolating LNC networks. Transport through the growing percolating LNC networks drives the rapid growth of the mobility as f_{LNC} grows past f_P. Therefore, the electron mobility exhibits a pronounced minimum as a function of f_{LNC}, centered at $f_{\mathrm{LNC}} = f_P$. The position of the mobility minimum shifts to larger LNC fractions as the electron density increases. We have studied the trends of this mobility minimum with temperature, electron density, charging energy, ligand length, and disorder. We account for the trends by a "renormalized trap model", in which capturing an electron renormalizes a deep LNC trap into a shallow trap or a kinetic obstacle, depending on the charging energy. We verified this physical picture by constructing and analyzing heat maps of the mobile electrons in the BNS.

Next, we showed that nanoparticle (NP) solids are an exciting platform to seek new insights into the disordered Mott-Hubbard physics. We further developed HINTS to build from localized states to describe the Disorder-localized and Mott-localized phases, and the transitions out of these localized phases. We also studied the interplay between correlations and disorder in the corresponding multi-orbital Hubbard model at and away from integer filling by Dynamical Mean Field Theory. This approach is complementary to HINTS, as it builds from the metallic phase of the NP solid. The mobility scenarios and phase diagrams produced by the two methods are strikingly similar, and account for the mobilities measured in NP solids.

Third, we analyzed the 3D structure of a 120×38 nm disc-shaped region of a PbSe QD epi-SL using full-tilt high-angle annular dark-field electron tomography. The high spatial resolution of the tomographic reconstruction (0.65 nm) enables determination of the center-of-mass coordinates of all 1,846 QDs in the sample as well as the size and shape of the thousands of epitaxial connections (necks) between the QDs. The tomogram reveals the detailed crystallography and internal positional disorder of the three SL grains that constitute this sample. A map of the neck network is used to quantify relationships between neck number (the number of necks each QD possesses), average neck diameter, QD location in the film, and the nearest neighbor inter-QD distance and

distance distribution. We found a strong positive correlation between neck number and local spatial order, suggesting that future improvements in neck connectivity are likely to simultaneously enhance the overall structural perfection of the epi-SLs. HINTS was employed to estimate the electron mobility of the tomography sample and assess the impact of grain boundaries on charge transport. The electron tomography study established a baseline for the quantitative statistical analysis of structural defects in 3D QD epi-SLs.

Fourth, we developed TRIDENS: the **Tr**ansport **i**n **De**fected **N**anoparticle **S**olids Simulator, that adds three more hierarchical layers to our HINTS code for nanoparticle solar cells. In TRIDENS, we first introduced planar defects, such as twin planes and grain boundaries into individual NP superlattices (SLs) that comprised the order of 10^3 NPs. Then we used HINTS to simulate the transport across tens of thousands of defected NP SLs, and constructed the distribution of the NP SL mobilities with planar defects. Second, the defected NP SLs were assembled into a resistor network with more than 10^4 NP SLs, thus representing about 10^7 individual NPs. Finally, the TRIDENS results were analyzed by finite size scaling to explore whether the percolation transition, separating the phase where the low mobility defected NP SLs percolate from the phase where the high mobility undefected NP SLs percolate, drives a low-mobility-to-high-mobility transport crossover that can be extrapolated to genuinely macroscopic length scales. For the theoretical description, we adapted the Efros-Shklovskii bimodal mobility distribution percolation model. We demonstrated that the ES bimodal theory's two-variable scaling function is an effective tool to quantitatively characterize this low-mobility-to-high-mobility transport crossover.

All four of these NP projects provided crucial insight into our understanding of transport mechanisms in NP solids, and the crucial role that defects play. Collectively this work is important for developing strategies for driving NP solids into the metallic regime and band-like transport.

The rest of the dissertation switches focuses to silicon heterojunction solar cells, which exhibit notable performance degradation. While the exact defect formation pathways are unknown, all degradation pathways can be modeled by electronic defects getting generated by thermal activation across energy barriers over time. To analyze the physics of this degradation, we developed the SolDeg platform to simulate the dynamics of electronic defect generation. First, femtosecond

molecular dynamics simulations were performed to create a-Si/c-Si stacks, using the machine-learning-based Gaussian approximation potential. Second, we created shocked clusters by a cluster blaster. Third, the shocked clusters were analyzed to identify which of them supported electronic defects. Fourth, the distributions of energy barriers that control the generation of these electronic defects were determined. Fifth, an accelerated Monte Carlo method was developed to simulate the thermally activated time dependent defect generation across the barriers. – Our main conclusions are as follows. (1) The degradation of a-Si/c-Si heterojunction solar cells via defect generation is controlled by a broad distribution of energy barriers. (2) We developed the SolDeg platform to track the microscopic dynamics of defect generation across this wide barrier distribution, and determined the time dependent defect density $N(t)$ from femtoseconds to gigaseconds, over 24 orders of magnitude in time, achieved by connecting the results of the femtosecond molecular dynamics simulations to the long time scale kinetic simulations. (3) We have shown that a stretched exponential analytical form can successfully describe the defect generation $N(t)$ over at least ten orders of magnitude in time. (4) We found that in relative terms the open circuit voltage ($V_{\rm oc}$) degrades at a rate of 0.2%/year over the first year, slowing with advancing time. (5) We developed the Time Correspondence Curve to calibrate and validate the accelerated testing of solar cells. We found a compellingly simple scaling relationship between accelerated and normal times $t_{\rm accelerated} \propto t_{\rm normal}^{0.85}$. (6) We ourselves carried out experimental studies of defect generation in a-Si:H/c-Si stacks. We found a relatively high degradation rate at early times, that slowed considerably at longer time scales.

Finally, we developed a Si-H Gaussian approximation potential in order to add H to our simulations of degradation of silicon heterojunctions. The Si-H GAP is able to closely match DFT measurements of microscopic quantities such as energies, forces and virial stresses, and is also able to reproduce structural characteristics such as partial pair correlation functions and the vibrational spectra. Reference structural data taken from Tersoff MD calculations highlights the improvement that is gained by adopting the non-parameterized model and more accurately matching the target potential energy surface. The Si-H GAP is more accurate than any interatomic potential which has come before it, and will be readily usable for the next phase of the project.

Acknowledgments

As my time at UC Davis comes to a close, I would like to thank all the people who have helped me along the way. A PhD is never a solo effort, and I was fortunate to have an outstanding group of mentors, collaborators, friends and family to help me make it to the end. The biggest thanks has to go to my advisor, Prof. Gergely Zimányi, who not only provided me endless research guidance and wisdom, but who was also a mentor to me in how to make the transition into life beyond graduate school. Be it life lessons, or advice on how to give a better presentation, Gergely has always had wisdom to share. Most importantly to me, he is always cheerful, and has often lifted me up when my research was going poorly. I am very fortunate to have had him as my research advisor.

Next, I would like to thank Luman Qu and Chase Hansen. Luman was a part of the Zimányi group when I first joined, and provided the initial version of the HINTS code, as well as numerous insights and tidbits of wisdom. Chase has worked in the group with me for many years (and for a few years it was just the two of us), and has been my go-to person to bounce ideas off of, have research discussions with, and strategize with about how we would move forward. His contribution to the work that has gone into this dissertation has been invaluable.

I would like to thank my many research collaborators on the projects and work documented in this dissertation. Prof. Matt Law at UC Irvine, who spearheaded the UC-wide collaboration on PbSe nanoparticles that I was a part of, and whose experiments were often a source of inspiration for much of my theoretical work on nanoparticles. Profs. Marcelo Rozenberg and Alberto Camjayi, who provided crucial DMFT work to explore the metal-insulator transition in PbSe NPs. Prof. Stephen Goodnick at Arizona State University, whose expertise in modeling solar cells and knowledge about silicon heterojunctions has been invaluable. Prof. Marian Bertoni at Arizona State University, whose experiments on silicon heterojunctions were a foundational inspiration for our work, and whose collaboration on our most recent work has been crucial to our success in ensuring that our models are useful and insightful. Prof. Gábor Csányi at University of Cambridge, who pioneered the development of Gaussian approximation potentials, and who was a crucial knowledge source as I have worked on developing our own Si-H GAP. Finally, I especially would like to give thanks to Reza Vatan Meidanshahi, a member of Prof. Goodnick's group, whose DFT work and knowledge

was crucial to much of our success in modeling degradation in silicon heterojunction solar cells, as well as developing a Si-H interatomic potential.

I would like to extend my gratitude toward the members of my dissertation committee, Profs. Dong Yu and Richard Scalettar, both of whom I have known for many years now, and have provided invaluable comments and suggestions for this dissertation.

Last but not least, I would like to thank my family and friends for their support over the many years of my PhD. I couldn't have done it without them. A special thanks goes out to Rooha Gealani, who has been there for me through the thick and thin of many of these transformative years, and who has had to hear endless practice talks, complaints about research problems, and far too many physics jokes.

CHAPTER 1

Introduction

Novel solar technologies, or emerging photovoltaics (PV), are technologies which have the potential to disrupt c-Si as the primary PV application platform. Typically, such technologies have demonstrated either a capacity for growth in their solar conversion efficiency, or already have high conversion efficiencies but struggle with other issues such as degradation. This dissertation will consider two such technologies: silicon heterojunction (HIT) solar cells, and nanoparticle solar cells. These technologies are interesting for separate reasons. Silicon heterojunction solar cells have now demonstrated higher efficiencies than c-Si solar cells, but still need to overcome issues with long-term open circuit voltage (V_{OC}) degradation before they can widely penetrate the market [**2**].

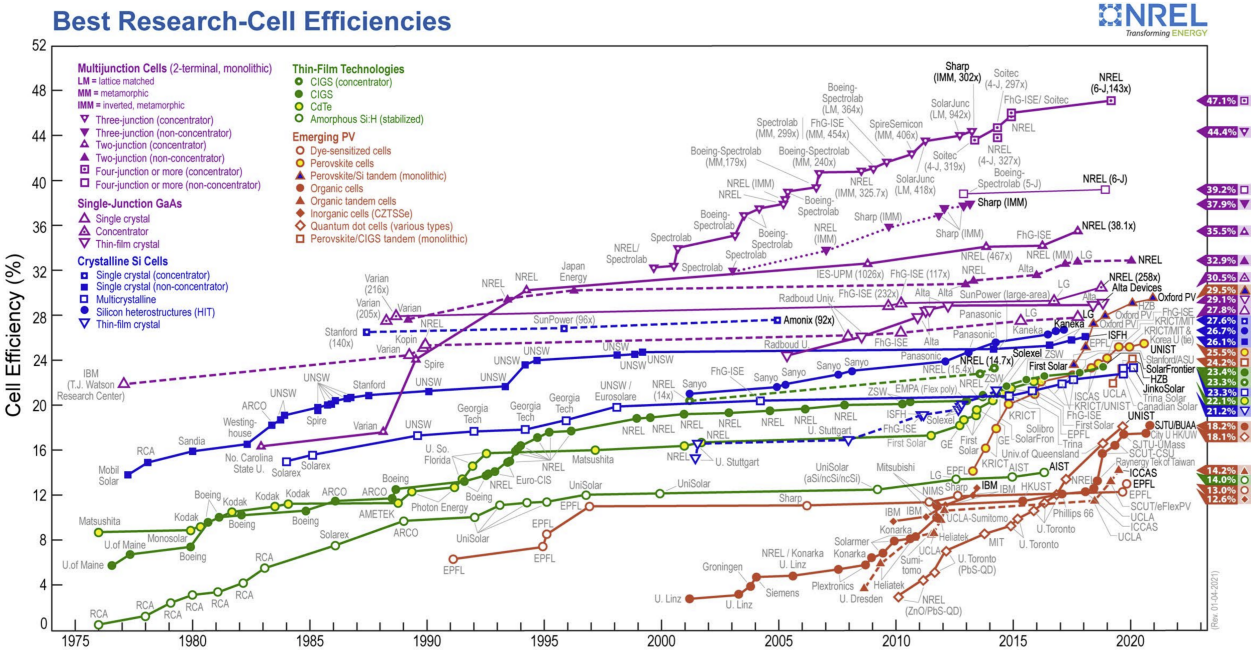

FIGURE 1.1. NREL chart of the best research-cell efficiencies [**1**]. Silicon heterojunction solar cell efficiency is displayed with blue circles, and nanoparticle solar cell efficiency is displayed with hollow orange diamonds.

Meanwhile, nanoparticle solar cells have demonstrated one of the highest growth rates year-over-year in their efficiency, but have not yet reached the efficiency level of c-Si. See Figure 1.1 for a visualization of the annual growth in peak efficiency of each widely studied solar technology. In the rest of this chapter, the interesting physics and problems in each of the two above PV technologies will be described in detail.

1.1. Nanoparticle Solids

Colloidal semiconductor nanoparticles (NPs) are singularly promising nanoscale building blocks for fabricating mesoscale materials that exhibit emergent collective properties. NPs are particles which typically contain between 100 and 10000 atoms, are between 1 and 100 nm in size. While NPs can be synthesized using a variety of methods, colloidal NPs are synthesized from solution in a two-stage process: rapid nanocrystal nucleation followed by slow growth in solution [**3**]. The most common nucleation technique is the hot injection method, where a precursor is rapidly injected into a hot coordinating solvent. The precursor contain organic ligands which bind to the surface of the nucleating NPs, stabilizing the growth and compensating for the large surface-to-volume ratio. Once the desired mean NP diameter is reached, the process is terminated by injecting a stabilizing chemical solution [**3**, **4**]. After this process, the individual NPs consist of an inorganic semiconductor core surrounded by a surface-passivating layer of organic ligand molecules, see for instance Figure 1.2(a). Using different variations of the synthesis process, other various precise shapes can also be achieved, such as rods and disks [**5**]. See Figure 1.2(b) for a visualization of how these different shapes form. The focus of this dissertation is on spherical nanoparticles, also known as quantum dots, which are the most common NP shape.

NPs have high scientific interest because they are well-defined building blocks that can be synthesized with excellent control of composition, size, and shape. In NP solids, electron wavefunctions are localized on the individual NPs. This "quantum confinement" makes the electronic parameters such as the band gap tunable with the NP diameter, and the energetics and the charge transport in NP solids can be tuned by changing the NP size, size distribution, shape, inter-NP spacing, spatial ordering, surface chemistry and defects, and the properties of the matrix between the NPs. There

is a growing interest to use NPs for numerous optoelectronic applications [**7**, **8**], including third generation solar cells [**9**, **10**] light emitting diodes [**11**], and field effect transistors (FET) [**12**, **13**].

NP solids are especially interesting for third generation solar cell concepts because not only does their tunable band gap allow for improved power conversion efficiency, but more importantly NP solids exhibit novel solar energy conversion paradigms which could lead to solar cell efficiencies which surpass the Shockley-Queisser limit of 33%, the maximum theoretical efficiency of a conventional single junction bulk solar cell [**14**]. The Shockley-Queisser limit emerges from two main factors: incoming photons with energies below the band gap cannot be absorbed, and incoming photons with energies well above the band gap create electron-hole pairs which rapidly thermalize by emitting phonons, heating the solar cell and wasting the excess above-band-gap energy. Solutions to these problems are respectively called up-conversion and down-conversion paradigms [**15**].

One such down-conversion paradigm is multiple exciton generation (MEG), in which a high-energy incoming photon excites a high-energy exciton, which then decays into multiple lower-energy excitons [**9**, **17**, **18**, **19**, **20**]. MEG is a pathway which is present in bulk semiconductors, but has very low efficiency [**16**]. In contrast, in NPs it has been shown that quantum confinement enhances the effective Coulomb interaction, decreasing the electronic screening, enabling the possibility of

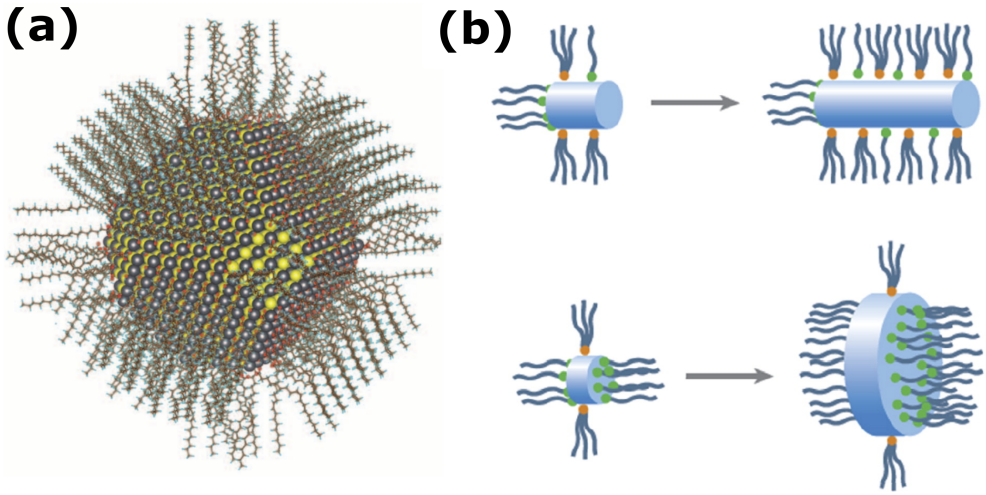

FIGURE 1.2. (a) A visualization of a spherical PbS NP coated in an organic ligand layer [**6**]. (b) Illustration of shape control of nanoparticles through selective organic ligand adhesion to particular crystal facets, slowing the growth of that side relative to others and leading to the formation of rod- or disk-shaped nanoparticles [**5**].

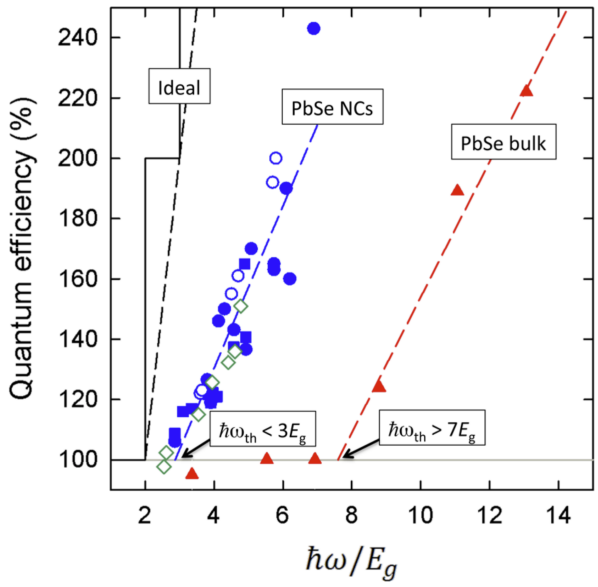

FIGURE 1.3. MEG efficiencies of PbSe NPs (blue and green symbols) and bulk PbSe films (red solid triangles) as a function of $\hbar\omega/E_g$. Taken from Ref. **16**.

an enhanced MEG efficiency. Early work by the Klimov group showed that a strong MEG can be observed in PbSe NP solids [**21**]. This was corroborated by later groups, who showed that in PbSe NPs MEG can enhance the external quantum efficiency above 100% [**22**]. Strong MEG is not unique to PbSe NPs, it has also been observed in numerous other NP systems, including PbS, CdSe, InP, Ge, and Si [**17**, **18**, **20**, **23**, **24**].

A leading up-conversion paradigm is the absorption of sub-band gap photons by an intermediate band located in mid-gap region of the absorption layer. It has been observed that NP solar cells are an ideal platform for implementing this paradigm, complementary to MEG, as the formation of mini-bands in NPs embedded in multilayer heterostructures can separate one or more intragap states from the valence and conduction bands [**25**, **26**]. In principle, intermediate band solar cells can deliver up to 47% efficiency under the AM1.5 spectrum. Utilizing both of the described down-conversion and up-conversion concepts, NP solar cells have been developed with impressive 13-18% power conversion efficiencies [**27**, **28**, **29**, **30**].

One of the factors limiting the utility of NP-based solar cells is the relatively high energetic and spatial disorder of NP solids. This disorder causes decoherence of the electronic wave functions between NCs and inhibits the emergence of new collective mesoscale behavior, resulting instead

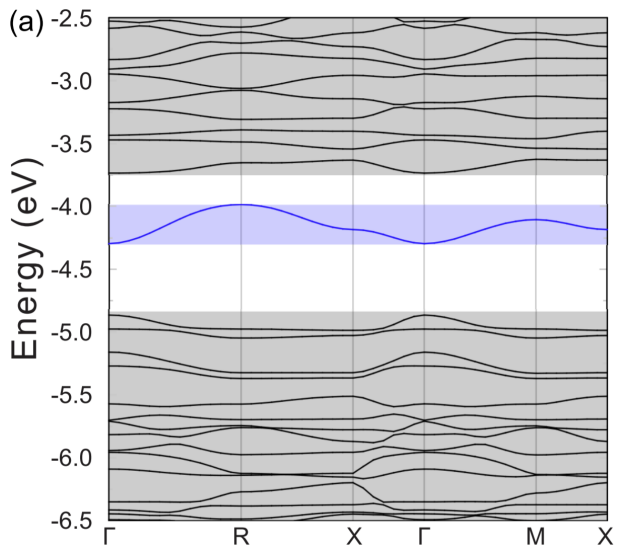

FIGURE 1.4. Illustration of an intermediate band formed in the band structure of CdSe NPs. Taken from Ref. **25**.

.

in weakly-coupled NP films with slow hopping transport. These factors, weak coupling and slow transport, are the primary agents hindering the realization of high-performance NP optoelectronics [**31**, **32**, **33**]. These factors used to limit the hopping mobility in NP solids into the $10^{-4} - 10^{-1}$ cm^2/Vs range. These mobilities are typically measured in FET arrangements. This is orders of mangitude below the mobilities that would be acceptable for electronic applications. Therefore, increasing the mobility and transport in NP solids is one of the central challenges on the way to realize the promise of NP solids.

Various experimental groups managed to boost the mobility by enhancing the inter-NP transition rate with a variety of methods, including: ligand engineering [**34**, **35**, **36**], band-alignment engineering [**37**, **38**], chemical-doping [**39**, **40**], photo-doping [**41**], metal-NP substitution [**42**], epitaxial attachment of NPs [**33**, **43**], and atomic layer deposition methods [**44**]. Encouragingly, these efforts recently translated into notable progress, as NP solids were reported to exhibit band-like, temperature-insensitive mobilities, with values exceeding 10 cm^2/Vs at room temperatures [**40**, **45**, **46**]. It is important to note that some experiments reported data that can be interpreted as evidence for band-like transport. One of these is the relative temperature independence of the observed mobilities, in contrast to hopping insulators where an activated temperature

dependence is expected. However, the absolute values of the mobilities remain relatively low compared to most metals, and this makes conservative commentators stop short of identifying this transport as metallic [**40**, **45**].

On the theoretical front, there have been efforts from several groups to understand electronic transport in NP films and solids. Density functional theory (DFT)-based ab initio calculations of the energy levels of a single NP alone are already limited to only hundreds of atoms for higher-reliability methods, and a few thousands for more approximate methods by prohibitive CPU times. These translate to diameters less than 2-3 nm, whereas experimental NP diameters often exceed 5-6 nm. Next, the accurate computation of the NP-NP transition rates would require the simulation of two NPs. And even if this calculation is completed, it does not address that the NP-NP transport is not metallic but insulating; the disorder of the parameters from NP to NP; and finally the defects of the NP solids. In total, ab initio descriptions alone are very far from being capable of describing transport in NP solids. Clearly, there is a pressing need for developing mesoscopic transport simulations that somehow integrate ab initio calculations.

Shklovskii et al. have developed transport calculations for a NP array in a FET geometry, where they focused on the effects of the Coulomb interaction [**47**]. The interplay of transport and Coulomb interactions was studied in Refs. **47** and **48**, albeit on very small samples. Over the last few years, our group developed the Hierarchical Nanoparticle Transport Simulator (HINTS) platform that starts with an ab initio calculation of the energetics of individual nanoparticles, then forms a NP solid of several hundred NPs, and finally simulates transport across this NP solid by a Kinetic Monte Carlo method [**49**, **50**]. HINTS can simulate 500-2,000 nanoparticles. A reassuring validation of HINTS emerged from simulating the dependence of the mobility of PbSe NP layers as a function of the NP diameter. The results in [**49**, **50**] closely tracked the experimental results of Liu et al., who studied the electron mobility of PbSe layers in a FET geometry [**31**]. More recently, we studied commensuration effects in bilayer NP solids [**51**].

The details of HINTS will be discussed in Chapter 2, and four further applications of HINTS to study various transport problems in NP solids will be presented in Chapters 3-6.

1.2. Silicon Heterojunctions

The world PV market is dominated by c-Si solar cells, with their estimated market share between 90 and 95% [**52**]. This can be attributed to a few reasons. c-Si has long stability, is non-toxic and abundant, has high power conversion efficiency (PCE), and the widespread use of c-Si in the microelectronics industry has lead to well-developed, scaled processing techniques [**53**]. These factors give c-Si a large edge over other semiconductor materials for PV applications. A key focus of current c-Si technological development is cost reduction, as c-Si accounts for 40-50% of the cost of a finished PV module [**54**]. A key pathway toward cost reduction is increasing the PCE, which would lower the levelized cost of electricity (LCOE) of c-Si solar cells.

The main limiting factor in further increasing the PCE in c-Si solar cells is unwanted carrier recombination. In general, solar cells generate electron-hole pairs via absorption of solar photons. This process creates excess minority carriers, which then diffuse across the built-in electric field, and make their way to electrical contacts where ideally they are efficiently collected [**55**]. Two primary sources of unwanted recombination interfere with this process. Surface recombination, which is especially important in thin film devices, and recombination at the metallic contacts. The former source of recombination has been largely eliminated by the introduction of surface passivation layers. However, the latter source of recombination remains an issue in traditional c-Si solar cells, and conventional methods involve a reduction in the capacity to eliminate surface recombination.

Beginning in the late 1980s, a more elegant solution began to be pursued. Rather than dealing separately with the passivation of the surface, and the elimination of unwanted recombination at the contacts, a single passivating contact layer can be introduced which minimizes both of these issues [**54**]. This is achieved by inserting a thin passivating semiconductor layer with a wider bandgap than c-Si, which separates the highly recombinant contacts from the c-Si surface. Charge moves through this buffer layer simultaneously slowly enough that a differential voltage can be built up, but fast enough that recombination prior to carrier collection at the contact is heavily reduced [**53**]. This buffer layer has been described as a semi-permeable membrane for carrier extraction [**54**].

Silicon heterojunction (SHJ) solar cells use hydrogenated amorphous silicon as their buffer layer. In a standard SHJ architecture, seen in Figure 1.5, c-Si is the primary absorber layer, and

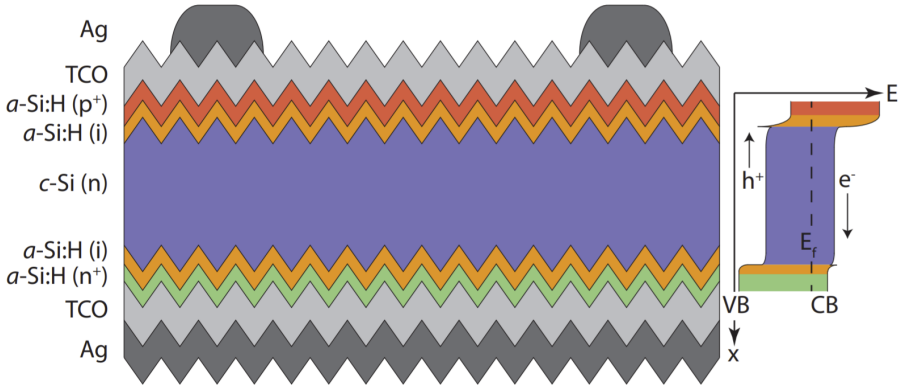

FIGURE 1.5. Visualization of a basic SHJ solar cell, including the band diagram. Taken from Ref. **53**.

deposited a-Si:H of both n- and p-type forms a passivating contact layer on both sides. The appeal of using a-Si:H for this purpose lies in its slightly wider bandgap (compared to c-Si), the ease of doping, excellent passivation qualities, and low temperature processing [**53**, **54**].

SHJ solar cells have world record efficiencies approaching 27%, due to the excellent surface passivation by their amorphous Silicon (a-Si) layer that leads to low surface recombination velocities and high open circuit voltages V_{OC}. Driven by open circuit voltages well above 700 mV, the fill factor (FF) in SHJs can reach 85%, the highest of any silicon solar cell to date [**56**]. In spite of the impressive efficiency records, SHJ cells have not yet been widely adopted by the market because of various perceived challenges. Several of these challenges, including the cost of n-type silicon wafers, the low temperature deposition of Ag leads, and the higher capital expense costs, are getting rapidly resolved, making SHJ technology competitive. It has been estimated by ITRPV (the International Technology Roadmap for Photovoltaic) that the market share of SHJ cells will be 10% by 2025, and 15% by 2031 [**57**], see Figure 1.6.

One of the remaining widely held reservations concerning the adoption of SHJ cells is that they may exhibit accelerated performance degradation, possibly related to their a-Si:H layer. Traditional crystalline Si (c-Si) modules typically exhibit about a 0.5%/yr efficiency degradation, primarily via their short circuit current I_{sc} and the fill factor FF, typically attributed to external factors, such as moisture ingress and increased contact resistance [**58**]. In contrast, in 2018 two papers reported studies of the degradation of fielded SHJ modules over 5-10 years [**59**, **60**]. They reported degradation rates close to 1%/yr, about twice the rate of traditional cells. These papers pointed

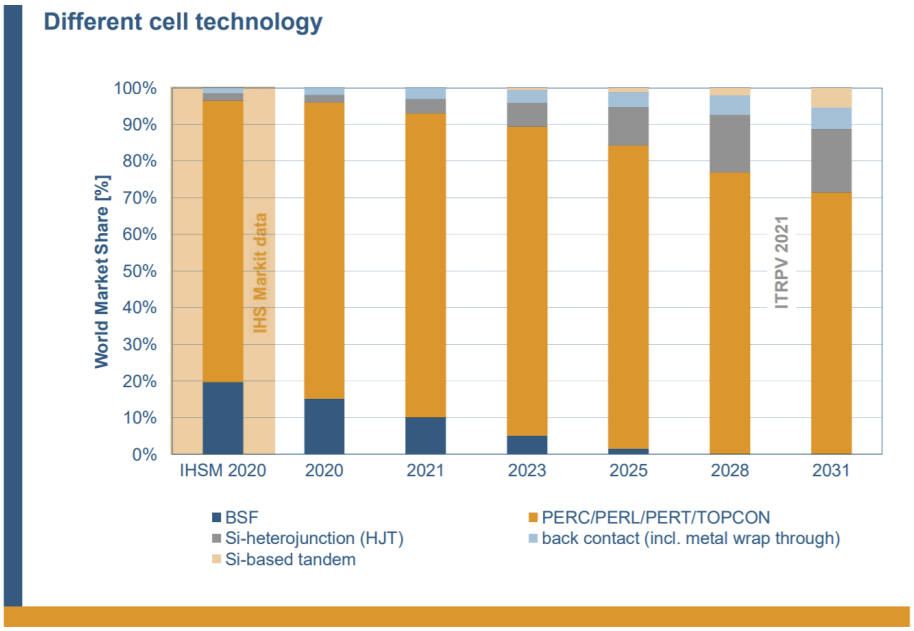

FIGURE 1.6. The 2021 ITRPV roadmap of predicted market share of the most prominent solar cell technologies [**57**].

to a new degradation channel, the decay of V_{OC}, at a rate of about 0.5%/yr. The decay of V_{OC} suggests that the degradation is possibly due to internal factors, increasing recombination either at the a-Si/c-Si interface, or in the a-Si layer. Such increased recombination is typically caused by the increase of the electronic defect density.

These initial reports on fielded panels were followed up by in-laboratory analysis. The Bertoni group has studied the surface recombination velocity (SRV) at the a-Si/c-Si interface in HJ stacks. By applying a model for the recombination at the a-Si/c-Si interface to their temperature- and injection-dependent SRV data, they analyzed the degradation of the carrier lifetime and were able to attribute it to a loss of chemical passivation [**61**]. More recently, Holovsky et al. investigated ultrathin layers of hydrogenated amorphous silicon (a-Si:H), passivating the surface of crystalline silicon (c-Si) [**62**]. These authors applied highly sensitive attenuated total reflectance Fourier-transform infrared spectroscopy, combined with carrier lifetime measurements. They manipulated the a-Si/c-Si interface by applying different surface, annealing, and aging treatments. Electronic interface properties were discussed from the perspective of hydrogen mono-layer passivation of the

c-Si surface and from the perspective of a-Si:H bulk properties. They concluded that both models have severe limitations and called for a better physical model of the interface [**62**].

Understanding the degradation of the passivated c-Si surface is important not only for understanding a-Si:H/c-Si heterojunction solar cells. The PV industry roadmap shows that among newly installed modules, the fraction of advanced Passivated Emitter/Rear Contact (PERC) modules will rapidly rise above 90% in the next 3 years. One of the advanced features of these PERC cells is the improved interface passivation with the application of elevated levels of hydrogen. However, the increased efficiency was accompanied by notable levels of degradation [**63**, **64**, **65**]. By experiments and by including all three charge states of hydrogen in their modeling, the authors speculated that the PERC cell degradation both in the dark and under illumination could be explained by the migration of and interaction between hydrogen ions in different charge states.

To summarize, the accelerated degradation of V_{OC} slows the market acceptance of the world-efficiency-record holder SHJ modules, and impacts the introduction of the advanced PERC cells, thereby impacting the entire PV industry roadmap. Therefore, analyzing and mitigating this degradation process is of crucial importance.

In chapter 7, the simulation platform which we have established to simulate and study the formation of interfacial defects in silicon heterojunctions, SolDeg, will be discussed for the case where hydrogen is absent. The inclusion of hydrogen is a crucial step in comprehensively simulating degradation pathways in silicon heterojunction solar cells. In chapter 8, the development of a Si-H interatomic potential for use with SolDeg will be presented in detail.

CHAPTER 2

Nanoparticle Simulation Methods

To study electron transport in disordered nanoparticle solids, our group has developed a kinetic Monte Carlo (KMC) platform termed the **Hi**erarchical **N**anoparticle **T**ransport **S**imulator, or HINTS. This platform does not take a complete ab-initio band structure approach to modeling the electron transport. While such an approach would be the most accurate, the computational expense is unfeasibly large due to the highly varied length, energy and time scales involved.

Adopting a more computable transport model, HINTS simulates electron transport using a multi-scale hierarchical method. The broad layers of this method are: (a) building a microscopic foundation from ab-initio descriptions of the individual nanoparticles themselves; (b) modeling electron transport between the nanoparticles on the length scale of a few nanometers; (c) describing mesoscopic transport across the entire disordered NP solid on the length scale of hundreds to thousands of nanometers. This approach, which characterizes electron transport as being hopping-driven, is quite suitable for the disorded systems that we consider, where disorder would have to be significantly decreased for band-like transport to occur. In the instances where we have needed to approach disorder levels where band-like transport can take place, our model is capable of being extended with approximations of metallic transport channels, and we have also supplemented the HINTS results with other simulation methods. These cases will be described in the appropriate thesis chapters.

In the subsequent sections of this chapter, the underlying features of the HINTS platform will be discussed in detail.

2.1. Hierarchical Nanoparticle Transport Simulator: HINTS

2.1.1. Microscopic Foundation: Modeling the Electronic NP Structure. The HOMO and LUMO band energies of the NPs are calculated using the $k \cdot p$ method of Kang & Wise [**66**].

We apply a rigid shift to align the infinite diameter limit of the conduction band edge with the bulk work function of PbSe. An illustration of this can be seen in Figure 3.1, in Chapter 3.

On-site Coulombic repulsion E_C, also referred to as the on-site charging energy, is the energy cost that needs to be paid to load each electron onto a given nanoparticle. The total charging energy accounting is defined by:

$$E_{C,\text{total}} = n(\Sigma^0 + \frac{(n-1)}{2}\Sigma). \tag{2.1}$$

Here, n is the number of electrons on the NP after the electron is added. Σ^0 is the total electrostatic energy cost of loading an electron onto a neutral NP, while Σ is the energy cost of the Coulomb repulsion with the (n-1) electrons already on the NP.

This self-charging energy can be calculated by a variety of methods, including the semi-empirical pseudopotential configuration interaction method of Zunger and coworkers and the single NP empirical-perturbative hybrid calculations of Delerue [**67**, **68**]. In this paper we report results with the latter approach. In this approach:

$$\Sigma^0 = \frac{e^2}{8\pi\epsilon_0 R}(\frac{1}{\epsilon_{\text{solid}}} - \frac{1}{\epsilon_{\text{NP}}}) + 0.47\frac{e^2}{4\pi\epsilon_0\epsilon_{\text{NP}}R}(\frac{\epsilon_{\text{NP}} - \epsilon_{\text{solid}}}{\epsilon_{\text{NP}} + \epsilon_{\text{solid}}}) \tag{2.2}$$

and

$$\Sigma = \frac{q^2}{4\pi\epsilon_0 R}(\frac{1}{\epsilon_{\text{solid}}} + 0.79\frac{1}{\epsilon_{\text{NP}}}) \tag{2.3}$$

For the dielectric constant inside the NP, we assume that it will be the bulk high frequency dielectric constant of PbSe, taken to be ϵ_{NP} =22.0. To model the dielectric constant of the medium surrounding the NP, we account for both the organic ligand shell of the NP as well as the presence of neighboring NPs. We assume that the ligands themselves have a dielectric constant of ϵ_{ligand} =2.0. The dielectric constant of the entire solid is then calculated using the Maxwell-Garnett (MG) effective medium approximation:

$$\epsilon_{\text{solid}} = \epsilon_{\text{ligand}}\frac{\epsilon_{\text{NP}}(1+\kappa f) - \epsilon_{\text{ligand}}(\kappa f - \kappa)}{\epsilon_{\text{ligand}}(\kappa + f) + \epsilon_{\text{NP}}(1-f)} \tag{2.4}$$

where κ is 2 for spherical NPs, and f is the filling factor.

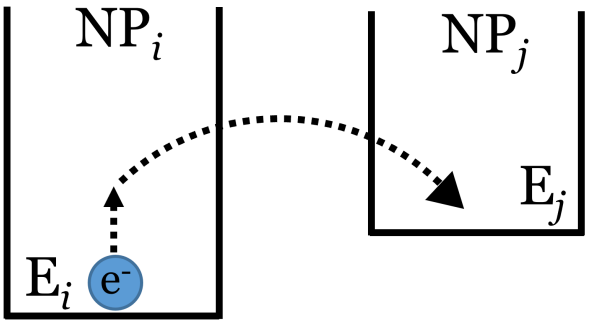

FIGURE 2.1. Illustration of a mobile electron hopping from NP$_i$ to NP$_j$.

2.1.2. Inter-NP Electron Transport. HINTS describes electron transport in disordered nanoparticle solids as being characterized by decoherent hopping. In this paradigm, illustrated in Figure 2.1, electrons are modeled as transitioning from nanoparticle to nanoparticle by hopping over the intermediary organic ligand barrier, absorbing or releasing phonons in order to match energy levels between the initial and final NPs. This NP-NP hopping can be either nearest neighbor or variable range hopping, and the hopping mechanism is commonly described either as Miller-Abrahams phonon-assisted hopping, or as a Marcus process where the electron transition involves an elastic reorganization of the NPs. All possible combinations of these hopping range and hopping mechanisms can be considered, including the intriguing case of variable range hopping governed by Marcus theory transitions [**69**]. We have adopted Miller-Abrahams phonon-assisted nearest-neighbor hopping as our framework for calculating the inter-NP electron transition rates. This choice was informed by experiments, which commonly report Miller-Abrahams activated temperature dependence near room temperature [**70**]. Under Miller-Abrahams, the transition rates are given by:

$$\Gamma_{i\to j} = \nu g_{ij}\beta_{ij}\exp\left\{(\frac{-\Delta E_{ij}}{k_b T})\right\} \tag{2.5}$$

where the attempt frequency ν is chosen to be $10^{12}\,\mathrm{s}^{-1}$ to match experimental data, g_{ij} is the product of the band occupation on NP$_i$ and the unoccupied band states on NP$_j$, determined by the NP band degeneracy, and β_{ij} is the tunneling amplitude. The energy difference between the initial and final configurations ΔE_{ij} is:

$$\Delta E_{ij} = \Delta E_{ij}^{sp} + \Delta E_{ij}^{F} + \Delta E_{ij}^{C} \tag{2.6}$$

where ΔE_{ij}^{sp} is the difference in single-particle band energies; ΔE_{ij}^{C} is the difference in charging energies; and ΔE_{ij}^{F} is the difference of the potential energy from the external electric field, $\Delta E_{ij}^{F} = q\frac{V}{L_z}(z_j - z_i)$, where L_z is the entire length of the sample in the $\hat{z}$ direction, and $(z_j - z_i)$ is the z distance between the two NPs. This external electric field is applied in order to induce electron motion and more easily measure the mobility. Care is taken to make sure that the applied voltage is low enough that the solids remain in the linear regime of the I-V curve.

Finally, β_{ij} is calculated using the WKB approximation as:

$$\beta_{ij} = \exp\left\{(-2\Delta x\sqrt{\frac{2m^*(E_{\text{vac}} - E_{ij})}{\hbar^2}})\right\}. \tag{2.7}$$

Here Δx is the NP-NP surface-surface separation distance. m^* is the effective mass of the electrons in the tunneling medium, approximated as $.05m_e$, the effective mass of electrons in bulk PbSe. E_{vac} is the vacuum energy level, set to be zero as all other energy levels are defined relative to the vacuum. E_{ij} is the tunneling energy, taken to be the average of the initial and final states of the hopping transition: $E_{ij} = (E_i + E_j)/2$, where E_i is the energy level of NP_i. This is the approach of Chandler & Nelson [**48**].

2.1.3. Mesoscopic Transport.

2.1.3.1. *Kinetic Monte Carlo Framework.* Monte Carlo (MC) algorithms are a class of numerical algorithms which incorporate random numbers in attempts to accurately simulate real-world problems. Broadly, this is implemented by calculating the probability of specific events, and then executing them if a random number between 0 and 1 falls in that specified range.

A kinetic Monte Carlo algorithm is a specific MC which seeks to accurately simulate the evolution in time of physical systems. It does so by propagating the physical system forwards step by step, executing a single event and evolving time accordingly at every step. In this manner, KMC simulations mimic explicitly the evolution of real-world systems.

Our kinetic Monte Carlo simulator is implemented according to the BKL algorithm [**71**]. At each step, the KMC tabulates the probabilities of all possible events occurring, and then chooses which one to execute by choosing a random number r_1 between 0 and 1. Time is then evolved by choosing another random number r_2 (also between 0 and 1). The specifics are as follows.

Once the simulation is initialized (and all charges have been placed at random into the network), the time-evolution starts by determining the transition rates Γ of all possible events, which will be locally updated after each algorithm step. In each step, the event j is executed using the random number r_1 for which the following equation is satisfied:

$$\sum_{i=1}^{j-1} \Gamma_i < r_1 \Gamma_{\text{sum}} < \sum_{i=1}^{j} \Gamma_i \tag{2.8}$$

where

$$\Gamma_{\text{sum}} = \sum_{i=1}^{N} \Gamma_i. \tag{2.9}$$

After this execution, time is evolved according to the second random number, r_2:

$$\Delta t = -\frac{\ln r_2}{\sum_{ij} \Gamma_{j \to i}} \tag{2.10}$$

Finally, the list of all possible events is updated to reflect the current state of the system, and the rate table is updated accordingly.

Our simulations typically run for 500,000 events, well into the steady state. Data is only collected after the transients have dissipated.

Mobility is measured in our simulation as:

$$\mu = \frac{(\text{harvested} \quad \text{charge}) * L}{\text{time} * N * F_{ext}}. \tag{2.11}$$

Here L the length of the simulation box, N the total number of carriers, and $F_{ext} = eV/L$. The harvested charge is the total charge of the electrons which have reached the drain electrode. Our simulations use periodic boundary conditions, so these electrons will pass through the drain electrode to the source electrode to be reintroduced to the sample. Any electron that travels in the opposite direction gives a negative addition to the current.

Conductivity can be taken directly from mobility. The classical relation is:

$$\sigma = ne\mu \tag{2.12}$$

where n is the volumetric electron density N/V.

2.1.3.2. *Simulation Samples.* Several different classes of NP solids are considered in this thesis. Chapter 3 considers disordered close-packed binary NP solids, which exhibit some form of lattice periodicity when one NP species dominates the binary system, but exhibit high levels of disorder when the two NP species are present in more equal proportions. Chapters 4, 5 and 6 all consider NP superlattices, where the NPs live on a periodic ordered lattice of either cubic or triclinic geometry, representative of the corresponding lab-grown structures. Chapter 5 additionally considers location disorder, where the NPs are shifted from their ideal lattice sites due to epitaxial fusion (or "necking") with neighboring NPs. Chapter 6 additionally considers the effect of extended defects, where the NP superlattice is disrupted by either a grain boundary, where on either side of the boundary the NP superlattice orientation can be entirely different, or a twin plane, where the NP superlattice is mirrored across the boundary plane.

Regardless of the class of NP solid considered, all NP samples used for our simulations consist of approximately 800 NPs arranged in a thin film geometry, for instance 20x2x20 (x, y, z) nanoparticles. This is appropriate for field-effect transistor (FET) NP solids where transport primarily occurs in the top few layers, with small penetration depths.

Each NP's diameter has a standard deviation σ, which can be either taken as the fixed value, or as a percentage of the diameter. A fixed diameter disorder has been shown to be appropriate for some corresponding experiments [**31**], while a percentage-based diameter disorder may be more suitable for the many experimental realizations of NP solids which exhibit larger size dispersions when synthesizing larger NPs. The mean inter-NP distance is taken as twice the average ligand length in the system, with variation due to the aforementioned size disorder. The ligand length is a tunable parameter, which is typically taken to be 0.5 nm to correspond to EDT (1,2-Ethanedithiol), which capped the nanoparticles in most experiments which do not include necking [**31**].

2.1.3.3. *Additional Simulation Details.* The NP solids are filled with mobile carriers at the start of each simulation by adding mobile carriers to individual NPs at random until a predefined electron

filling n, or e^-/NP, is reached. This electron filling level can either be independently chosen, or emerge from the choice of volumetric electron density, e.g. e^-/unit volume.

To get reliable statistics, each HINTS calculation is averaged over simulations performed on 100 or more NP solids. Calculation error bars correspond to the standard deviation of the mean. We found that in many NP solids the disorder of nanoparticle energies does not average exactly to zero, creating an internal voltage bias which can disrupt our simulations. To remove this, on each NP solid the voltage bias is applied both in the forward and reverse transport directions (2 different simulation runs), and the resulting current is pairwise averaged.

CHAPTER 3

Percolative Charge Transport In Binary Nanocrystal Solids

This work appeared as Physical Review B 103, 195303 (2021).

Colloidal semiconductor nanocrystals (NCs) are exciting nanoscale building blocks for fabricating mesoscale materials that exhibit emergent collective properties. NCs are well-defined building blocks that can be synthesized with excellent control of composition, size, and shape. The energetics and the charge transport in NC solids can be tuned by changing the NC size, size distribution, shape, inter-NC spacing, spatial ordering, surface chemistry and defects, and the properties of the matrix between the NCs. This remarkable tunability makes NC solids promising promising platforms for optoelectronic applications [**7**, **8**], including third generation solar cells [**9**, **10**], light emitting diodes [**11**], and field effect transistors (FETs) [**12**,**13**]. NC solids are especially interesting for solar cell applications because the band gap can be tuned by changing the NC size in order to improve device power conversion efficiency. Solar cell efficiency can also be improved by leveraging quantum confinement to open new energy conversion channels such as the down-converting carrier multiplication (CM), in which more than one electron-hole pairs are generated per absorbed photon [**9**, **17**, **18**, **19**, **20**]. CM has the potential to boost solar cell efficiency to 44%, well beyond the Shockley-Queisser limit of 33% [**14**]. Very recently, we have advocated for the formation of mini-bands in NC solar cells to implement the complementary, up-converting intermediate band solar cell paradigm [**25**]. In principle, intermediate band solar cells can deliver up to 47% efficiency at one sun illumination.

One of the factors limiting the utility of NC-based optoelectronics is the relatively high energetic and spatial disorder of NC solids. This disorder causes decoherence of the electronic wave functions between NCs and inhibits the emergence of new collective mesoscale behavior, resulting instead in weakly-coupled NC films with slow hopping transport. These factors, weak coupling and slow transport are the primary agents hindering the realization of high-performance NC optoelectronics [**31**, **32**, **33**]. These factors used to limit the hopping mobility in NC solids into the $10^{-4} - 10^{-1}$

cm^2/Vs range. Recently, new reasons for optimism emerged as various groups managed to boost the mobility by increasing the inter-NC charge transfer rate with a variety of methods, including ligand engineering [**34**, **35**, **36**], band alignment engineering [**37**], chemical doping [**39**, **40**], photodoping [**41**], metal-NC substitution [**42**], epitaxial attachment of NCs [**33**, **43**], and atomic layer deposition (ALD) infilling [**44**]. In some cases, these efforts managed to reach mobilities exceeding 10 cm^2/Vs [**46**].

To increase the mobility even further, a deeper understanding of the role of disorder is essential. A particularly promising testing platform is the class of binary nanocrystal solids (BNSs), which are crystalline solids composed of two different types of NCs. These metamaterials can be formed from NCs of different composition and/or size [**7**, **33**, **72**, **73**, **74**, **75**]. The Murray group demonstrated the possibility of fabricating such binary nanocrystal solids as large area monolayer and bilayer structures [**73**]. Later, they were able to perform an in situ ligand exchange, producing ultrafast directional carrier transfer on the timescale of 1 ps [**74**]. They were also able to increase the conductivity by more than three orders of magnitude by substituting an increasing fraction of PbS NCs with Ag or Au NCs [**42**]. The Alivisatos group focused on the percolation aspects of the electron transport, and beautifully imaged charge percolation pathways [**72**]. Whitham et al. devised ingenious ways to extract the localization length of the electrons in a type of percolative NC systems to further characterize transport [**33**].

Theoretical efforts have kept pace with these promising experimental developments only partially. A pioneering study of charge transport in NC arrays was performed by Chandler and Nelson [**48**]. They modeled the electronic structure of individual NCs using the $k \cdot p$ method, then performed Monte Carlo transport studies on small samples of 2x2x3 and 3x3x4 NCs. In the case of low charging energy, metal-insulator transitions were observed at electron occupation levels $\langle n \rangle$ that corresponded to the complete filling of an s, p, or d shell. When the charging energy became comparable to the level broadening, additional minima appeared in the conductance at every integer value of $\langle n \rangle \rangle$ as a result of electron-electron repulsion. The charge transport properties of NCs embedded in a matrix were explored by others using a kinetic Monte Carlo (KMC) method [**76**,**77**]. Although these papers developed an advanced method that was capable of handling the long-range Coulomb interactions, the small system sizes limited the definitiveness of their conclusions.

Our first contribution to this field was to develop the kinetic Monte Carlo platform HINTS – the Hierarchical Nanoparticle Transport Simulator – to compute the electron and hole mobilities as a function of the NC diameter [**49**]. We found that the mobility exhibited a maximum or plateau as a function of the NC diameter (depending on the type of disorder). This finding was in agreement with corresponding experiments [**78**, **79**]. Since then, we extended HINTS to describe the metal-insulator transition in NC solids and proposed a quantum percolation model to explain the unique criticality observed [**50**, see also **80**]. Very recently, we demonstrated that NC solids are an excellent platform to study Mott-Hubbard phenomena, as they exhibit transport transitions driven by interactions, by disorder, and by their interplay [**81**].

In this paper, we adapt and apply our hierarchical transport simulator HINTS [**49**,**50**] to study charge transport in binary nanocrystal solids (BNSs) consisting of PbSe NCs of two different sizes. Our simulation results are motivated by early stage efforts to measure the transport of such binary NC films fabricated with layer-by-layer dip coating of colloidal mixtures. Our main results include the following. First, our HINTS simulations of the mobility of field-effect transistors made from PbSe NCs with a mixture of 6.5 nm diameter large NCs (LNCs), and 5.1 nm diameter small NCs (SNCs) showed a deep minimum at a fraction of the LNCs, $f_{\mathrm{LNC}} = 0.25$. The minimum persists up to temperatures where kT becomes comparable to the difference of the conduction band edge energies of the LNCs and SNCs. We developed a percolative theory to explain this deep mobility minimum. We propose that at low f_{LNC}, the LNCs form traps and thus suppress the mobility. With increasing f_{LNC}, these LNC traps coalesce into a percolative transport pathway at $f_{\mathrm{LNC}} = f_{\mathrm{P}}$. f_{LNC} increasing beyond f_{P} opens a new transport channel: the electrons propagating through the percolating LNCs. This new channel starts boosting transport with increasing f_{LNC}, thereby explaining the mobility minimum. Second, we analyzed the impact of NC site energy disorder, carrier density, charging energy, and ligand length on the transport. We developed an electron-occupation-induced trap renormalization model that accounted for the dependence of the mobility on these four parameters. Finally, we validated our percolative theory of LNC traps transforming into percolative transport pathways as a function of f_{LNC} by constructing and analyzing heat maps of the carrier residence times.

3.1. Overview of Simulation and Results

For this work, we extended and adapted the HINTS platform as outlined in chapter 2 to describe transport in binary NC solids. The specifics are highlighted here.

(1) We used the event-driven molecular dynamics code PackLSD [**82**] to generate a random-packed, jammed NC solid for the simulation. The NC solids typically included many hundred NCs with a form factor of 10x10x1, inspired by the experimental geometry of 2D FET channels. For example, a monodisperse sample containing 400 NCs was packed into a simulation volume with the approximate spatial extent of 16x16x1.6 NC diameters. It is noted here that due to the form factor of these NC solids, short range processes can have 3D character, phenomena driven by long range correlations, such as phase transitions, are effectively 2D. For the binary NC solids, the diameters of the small NCs (SNCs) and large NCs (LNCs) were selected from corresponding Gaussian distributions, with widths σ_{SNC} and σ_{LNC}, and then jam-packed to form the binary NC solid BNS. We note that experimentally the amount of disorder in the NC solid can be tuned, from an approximately ordered solid to a more disordered solid, with some degree of glassiness.

(2) Next, the energy parameters of the Hamiltonian of each NC were established as follows. We used the photoelectron spectroscopy results of Jasieniak et al. [**83**] modified by the method of Miller et al. [**84**] to estimate the energies of the valence band maximum (E_{VBM}) and conduction band minimum (E_{CBM}) of PbSe NCs as a function of NC diameter. These energies are modified, or tuned, from their bulk values by "quantum confinement", the fact that the electron wavefunctions are localized on the NCs. The values are plotted in Figure 1. Photoelectron spectroscopy provides a direct measurement of E_{VBM}, from which E_{CBM} can be estimated by adding the NC band gap. Following Jasieniak et al., we show limiting values of E_{CBM} obtained using the experimentally-determined optical band gap ($E_{\mathrm{CBM,optical}}$) and a calculated upper estimate of the electronic band gap, which includes Coulomb and polarization energies ($E_{\mathrm{CBM,max}}$), yielding a range of E_{CBM} values for each NC size (green band in Fig. 3.1). Clearly, E_{CBM} exhibits a much larger change with NC size than does E_{VBM}. For example, 75-85% of the difference in band gap for 5.1 nm and 6.5 nm NCs is due to the change in E_{CBM}, with the exact value depending on the true electronic band gap of the PbSe NC. Building on these experimental findings, for our HINTS simulations we used the

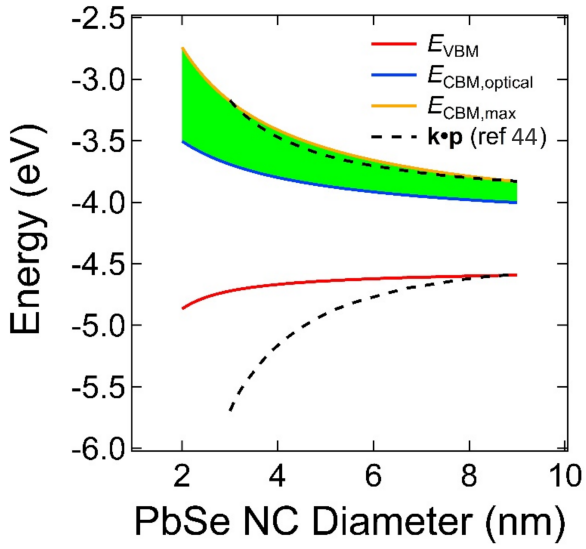

FIGURE 3.1. Absolute conduction and valence band edge energies (E_{CBM} and E_{VBM}) of PbSe NCs as a function of NC diameter. E_{VBM} was measured by photoelectron spectroscopy [**83**, **84**]. E_{CBM} has a range of values (green band) bracketed by E_{CBM},optical (from the measured optical band gap) and $E_{\mathrm{CBM,max}}$ (from a DFT-calculated upper estimate of the electronic band gap). Also shown are the E_{CBM} and E_{VBM} curves calculated from $k \cdot p$ theory (dashed lines, ref. **66**), rigidly shifted along the ordinate to match the experimental data at large NC size. The latter E_{CBM} curve is used to parameterize our transport model. Contribution to this Figure by Matt Law is gratefully acknowledged.

E_{CBM} curve from the $k \cdot p$ calculations of Kang and Wise (dashed line in Fig. 3.1) [**66**], which is well-validated by its dependence on the NC size closely tracking the experimental $E_{\mathrm{CBM,max}}$ values.

(3) We simulated the transport across the BNS using the extended kinetic Monte Carlo method with activated hopping transitions between nearest-neighbor NCs, as outlined in chapter 2. Electrons were added to the BNS at random with a specified average electron density (e/NC). Then the electrons were allowed to relax to favorable energy configurations. Transport was simulated by applying an electric field and measuring the responsive current. The overall NC-NC hopping attempt rate prefactor was selected such that the simulated mobilities were consistent with published experimental values [**78**]. We systematically explored wide ranges of temperature, disorder, electron density, and Coulomb interaction. The mobilities were determined by simulating at least 40 samples, and often more than 100 samples, at each set of parameters and then averaging the results. Since each mobility was determined from a dynamic flow of hundreds of electrons over

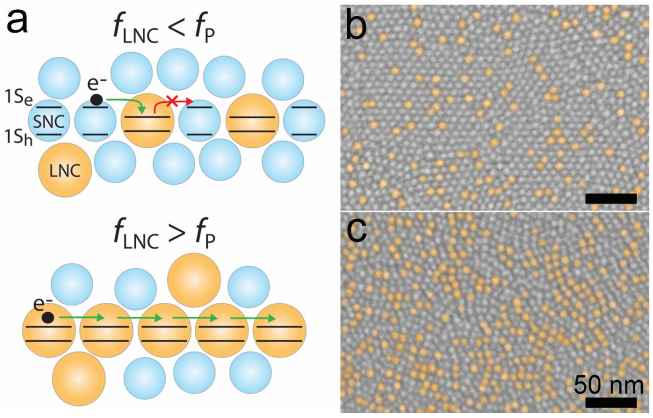

FIGURE 3.2. **(a)** Schematic representation of a binary NC solid containing (top) a small fraction of LNCs and (bottom) a larger fraction of LNCs. When $f_{LNC} < f_P$, the LNCs act as isolated carrier traps, impeding transport. When $f_{LNC} > f_P$, the LNCs form contiguous low-energy transport pathways that facilitate transport. **b-c**: Colorized SEM images of a monolayer of a binary NC solid made from 6.5 nm and 5.1 nm PbSe NCs with **(b)** $f_{LNC} = 0.12$ ($< f_P$) and **(c)** $f_{LNC} = 0.31$ ($> f_P$). The LNCs are shaded orange. LNC percolation pathways are evident in the latter image. The NCs are capped by oleate ligands (prior to exchange with EDT). Scale bars are 50 nm. SEM image is courtesy of Matt Law, UC Irvine.

105-106 time steps, we achieved a remarkably good self-averaging with small error bars even with this moderate number of samples.

Next, we describe the experimental motivation for our work, the main simulation results obtained using HINTS, and the physical picture emerging from the simulations.

Fig. 3.2a illustrates charge transport in a binary PbSe NC solid. Quantum confinement modifies the $1S_e$-$1S_h$ band gaps of the LNCs to be smaller than those of the SNCs, and the $1S_e$ energies (i.e. E_{CBM}) of the LNCs lower than those of the SNCs. Therefore, in a binary NC solid with a small f_{LNC} fraction, the LNCs act as traps for the mobile electrons. (Fig. 3.2a, top). Accordingly, as f_{LNC} is increased from small values, the increasing trap density causes a monotonic decrease of the carrier mobility.

Increasing f_{LNC} first enables the LNCs to form clusters, and then increases the size of the LNC clusters in the BNS. Once f_{LNC} exceeds the percolation threshold f_P, the LNC clusters interconnect to form contiguous percolation networks that span the entire BNS. These LNC percolation networks open new transport channels: low-energy, low-disorder and thus high-mobility transport pathways

(Fig. 3.2a, bottom). As $f_{\mathrm{LNC}} \to 1$, the percolation networks densify and the mobility steadily increases toward its value in a monodisperse NC solid, formed only from LNCs.

Figs. 2b-2c compare scanning electron microscopic images of monolayer-thick films of oleate-capped 6.5 nm and 5.1 nm PbSe NCs having f_{LNC} fractions below and above f_{P}. For $f_{\mathrm{LNC}} = 0.31$ ($> f_{\mathrm{P}}$), the LNCs (colored orange) visibly form essentially sample-spanning clusters. These images show that the LNCs are well mixed in the SNC films and have no tendency to phase separate into pure LNC domains.

Before proceeding, a word about the experimental systems. The binary NC films were made by layer-by-layer dip coating of colloidal mixtures of 6.5 nm and 5.1 nm PbSe NCs. The NCs were synthesized by the hot injection method. Colloidal solutions of different LNC number fraction (f_{LNC}) were prepared in hexane, dip coated onto prepatterned field-effect transistor (FET) substrates using ligand exchange with 1,2-ethanedithiol (EDT), and then infilled and overcoated with amorphous alumina using low-temperature atomic layer deposition (ALD), yielding transistors with dominant n-channel (electron) transport, excellent stability, and greatly-reduced I-V hysteresis compared to EDT-treated NC FETs before ALD infilling [**85**]. The f_{LNC} values of the resulting films were confirmed by analyzing SEM images of the first NC monolayer in the FET channel (like those in Figs. 2b-2c). The experimental methods are described in further details in Appendix A. We continue with presenting the results of our simulations.

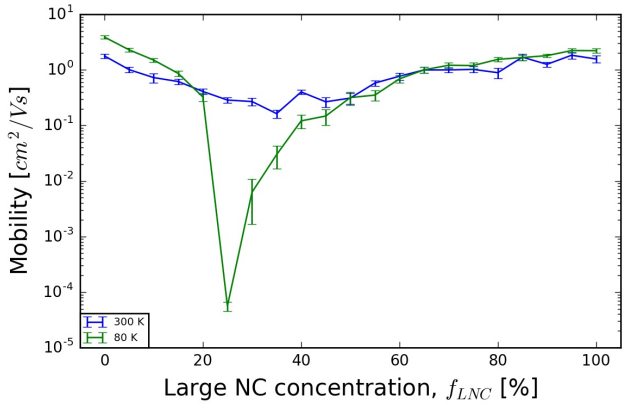

FIGURE 3.3. Simulated electron mobility versus f_{LNC} for 6.5 nm and 5.1 nm PbSe NCs. $\Delta E_{\mathrm{CBM}} = 60\,\mathrm{meV}$; with a diameter disorder of $\sigma_{\mathrm{LNC}} = 0.325$ nm and $\sigma_{\mathrm{SNC}} = 0.046$ nm; and electron density $n = 0.25\ e/\mathrm{NC}$.

3.1.1. Mobility as a function of LNC fraction f_{LNC}. Fig. 3.3 presents the HINTS-simulated mobility of a PbSe BNS with NC diameters of 6.5 nm and 5.1 nm at $T = 80$K and 300K. The corresponding difference of the SNC and LNC conduction band energy minima was taken from Fig. 3.1 as $\Delta E_{\mathrm{CBM}} = 60$ meV; for other parameters see the Supplemental Material. The simulated mobility curve at $T = 80$K shows a deep mobility minimum at $f_{\mathrm{LNC}} = 0.25$. Interpreting f_{LNC} of this minimum as approximately equal to f_{P}, the geometric percolation fraction is consistent with the prediction of $f_{\mathrm{P}} = 0.24$ of bond percolation theory [**86**], as well as with the percolation onset of $f_{\mathrm{P}} = 0.22$, observed in our recent calculations of NC films [**50**]. The precise relationship between the position of the mobility minimum and f_{P} is impacted by the NC packing and the electron density, as discussed below.

Another feature is that the mobility of the monodisperse solid of LNCs ($f_{\mathrm{LNC}} = 1.0$) is smaller than, or equal to, the mobility of the monodisperse solid of SNCs ($f_{\mathrm{LNC}} = 0$). This feature seems to contrast to previous reports [**31**, **49**] that electron mobility increases with NC size. However, in our simulations, the LNCs have a larger size disorder than the SNCs, large enough to offset the expected gain in mobility from an increasing NC diameter.

The key message of this simulation is the emergence of a mobility minimum as a function of f_{LNC} around f_{LNC}=f_{P}, which is sharp and deep at low temperatures, and partially smoothed at higher temperatures. As mentioned earlier, we developed a percolative theory to explain this deep mobility minimum. We propose that as the lower-energy LNCs are introduced into the higher-energy SNC matrix at low f_{LNC}, the LNCs form traps and thus suppress the electron mobility. With increasing f_{LNC}, these LNC traps coalesce into a percolative transport pathway at $f_{\mathrm{LNC}} = f_{\mathrm{P}}$. Once f_{LNC} increases beyond f_{P}, the electrons can propagate through this percolating network of LNCs, thus opening up a new transport pathway. As f_{LNC} grows past $f_{\mathrm{P}} \to 1$, the percolating networks densify and the mobility steadily increases toward its value in a monodisperse NC solid, formed only from LNCs. The opening of this new percolating LNC transport channel at $f_{\mathrm{LNC}} = f_{\mathrm{P}}$, and its subsequent broadening as f_{LNC} grows past f_{P} explains the mobility minimum.

3.1.2. Mobility as a function of temperature T. The mobility minimum is considerably smoothed out as the temperature is raised from T=80K to T=300K. The mobility at the minimum rises by a bit more than three orders of magnitude. The ratio of the mobilities at the minimum for

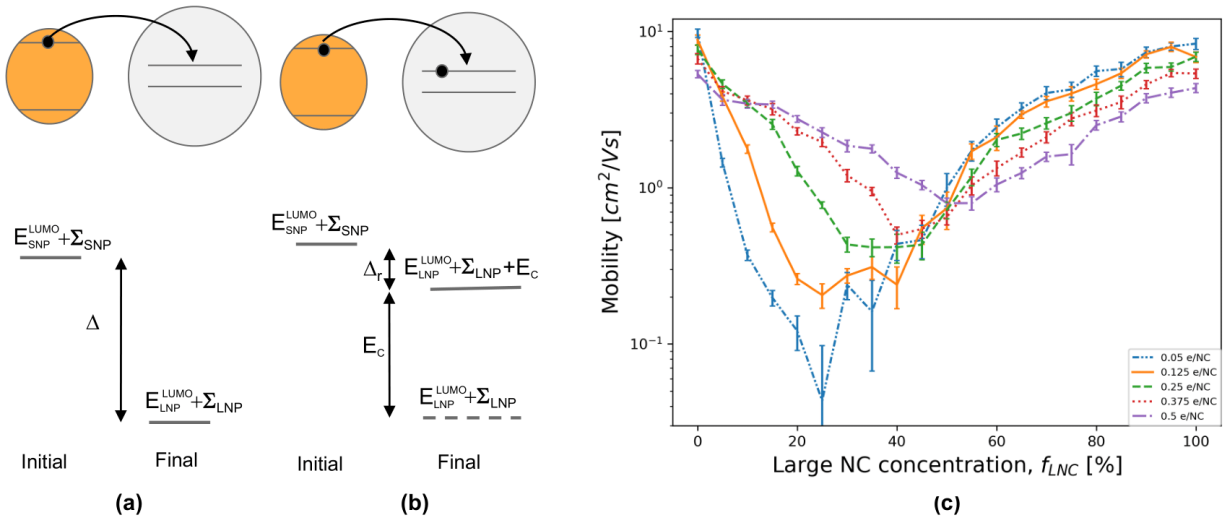

FIGURE 3.4. **Impact of electron density when** $E_C < \Delta$. **(a)** Energy levels of the initial state and the final state of an electron hopping from an SNC on an unoccupied trap of an LNC. **(b)** Energy levels of the initial state and the final state of an electron hopping from an SNC on a singly occupied trap of an LNC. The unchanging energy of the electron already on the LNC is not shown expressly for clarity. The dashed level shows the energy without the charging energy E_C for reference. **(c)** Mobility vs. f_{LNC} for electron densities from 0.05 e/NC to 0.5 e/NC at $T = 80$K, with $\sigma_{SNC} = 0.01$ nm and $\sigma_{LNC} = 0.08$ nm for $E_C < \Delta$. The mobility at zero LNC concentration is higher than in Fig. 3.3, because the disorder of the SNC diameters, σ_{SNC}, is four times smaller than in Fig. 3.3.

the two temperatures is consistent with an estimate based on an activated transport across a gap of $\Delta E_{CBM} = 60$ meV. Of course, the precise value of the mobility is further impacted by f_{LNC}, and the electron density as well.

We add that more complex behaviors can emerge as a function of temperature. The depth of the mobility minimum is controlled by the f_{LNC} fraction of the LNCs in the BNS and the thermal activation factor $\exp\{(-\Delta/k_B T)\}$, corresponding to an electron hopping from an LNC "trap" to an SNC. In a first approximation, the Δ energy barrier faced by an electron in an LNC trap can be identified with ΔE_{CBM}. However, for traps that are already occupied, the trap energy Δ is renormalized to the smaller value of $\Delta_r = \Delta E_{CBM} - E_C$, as long as $\Delta E_{CBM} > E_C$. Next, it is recalled that Kang et al. reported that some experiments can be explained by assuming that the charging energy E_C depends on the temperature to a substantial degree: $E_C = E_C(T)$ [**87**]. In their work, Kang et al. reported a 40-70% increase of $E_C(T)$ as the temperature was raised from

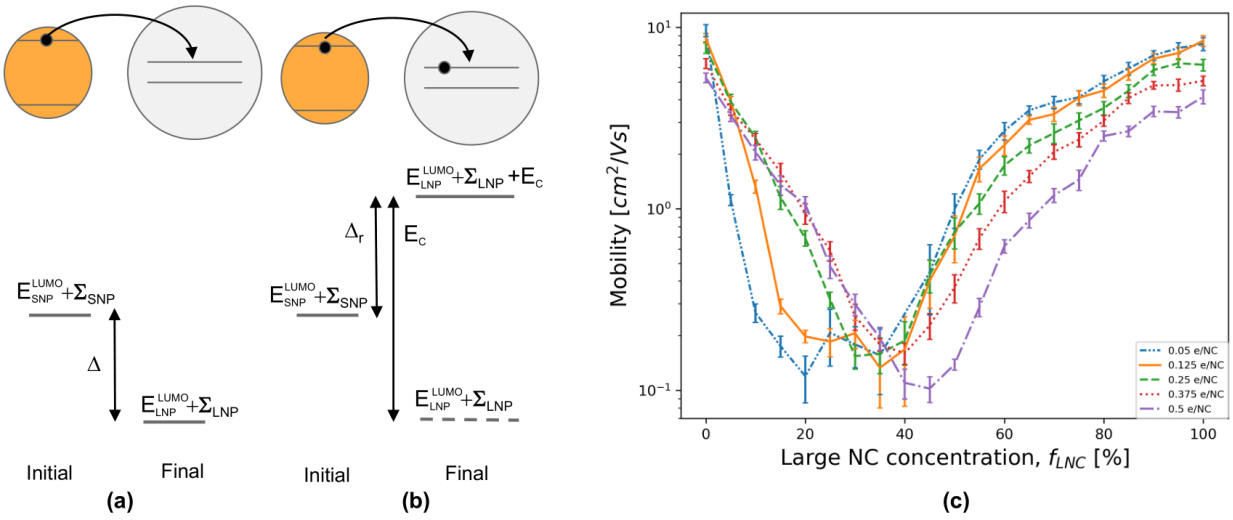

FIGURE 3.5. **Impact of electron density when $E_C > \Delta$.** **(a)** Energy levels of the initial state and the final state of an electron hopping from an SNC on an unoccupied trap of an LNC. **(b)** Energy levels of the initial state and the final state of an electron hopping from an SNC on a singly occupied trap of an LNC. The starting energy of the electron already on the LNC is not shown expressly for clarity. The dashed level shows the energy without the charging energy Ec for reference. **(c)** Mobility vs. f_{LNC} for electron densities from 0.05 e/NC to 0.5 e/NC at $T = 80$K, with $\sigma_{\mathrm{SNC}} = 0.01$ nm and $\sigma_{\mathrm{LNC}} = 0.08$ nm for $E_C > \Delta$.

$T = 20$K to 80K. A charging energy $E_C(T)$ that increases with temperature creates a renormalized trap energy $\Delta_r(T)$ that decreases with increasing temperature. This mechanism can explain a smoothing of the mobility minimum with the temperature that is faster than a smoothing driven by temperature-independent energy parameters alone.

Remarkably, the opposite scenario can arise as well. If $\Delta E_{\mathrm{CBM}} \gg E_C$, then several electrons can occupy each trap. This creates effective traps whose energy spectrum is a ladder with E_C level spacing, and thus E_C plays the role of the renormalized trap energy $\Delta_r = E_C(T)$. In this parameter range, a Kang-type temperature-dependent charging energy creates a renormalized gap $\Delta_r(T)$ that increases with increasing temperature, making the high temperature mobility minimum deeper than the one corresponding to temperature-independent parameters.

The above considerations motivate us to investigate the behavior of the BNS mobility in different parameter ranges, and to use our interaction-renormalized trap model to analyze and interpret our results. This is what we do in the rest of this paper.

3.1.3. Mobility as a function of electron density n and charging energy E_C. The electrostatic effects of adding electrons to a NC are taken into account following the work of Delerue [**88**, **89**]. When an electron is added to a neutral NC at the bottom of the conduction band, the E_{CBM} energy is increased by the one-electron self-energy, Σ, arising from the charging of the NC, also including the effect of the NC's polarizable host. When a second electron is added, the screened repulsion between the two electrons costs an additional charging energy E_C (denoted as U by Delerue). When the KMC step of HINTS evaluates the probability of a jump from one NC to another NC, the difference between the total initial energy and total final energy is calculated, including these electrostatic energies. The details of the HINTS code are described in chapter 2.

When a LNC is unoccupied within a SNC matrix, it is a trap with a depth for an electron. Δ is given by the difference of the CBM energies of the LNC and the SNC, ΔE_{CBM}, plus the difference of the self-energies $\Sigma_{LNC} - \Sigma_{SNC}$: $\Delta = \Delta E_{CBM} + (\Sigma_{LNC} - \Sigma_{SNC})$. When the trap is already occupied by an electron, the trap energy Δ gets renormalized by the charging energy E_C to $\Delta_r = \Delta - E_C$. For $E_C < \Delta$, this renormalization transforms the deep traps into shallow traps, making them much less efficient in hindering transport. For $E_C > \Delta$, this renormalization transforms the LNCs from negative-energy traps into positive-energy obstacles.

We explore the effects of varying the charging energy by simulations using $E_{C,LNC} = E_{C,SNC} = E_C = 35$, and $E_{C,LNC} = E_{C,SNC} = E_C = 125$meV, in order to explore both relevant regimes of $E_C < \Delta$, and $E_C > \Delta$. The effects of the charging energy E_C are closely interdependent with that of the electron density n. We therefore explored the average electron density n sweeping across $n = 0 - 0.5$ e/NC, because most density-dependent phenomena are cyclic with a n period of 1. Therefore, in the complementary range of $n = 0.5 - 1.0$ e/NC, the mobility's behavior is the approximate mirror image across $n = 0.5$, and for $n > 1$, the entire cycle repeats.

Figs. 3.4 and 3.5 show simulation results for small and large Ec. In both cases, the mobility minimum gets shifted to larger f_{LNC} concentrations as the electron density n grows. The primary reason for this is trap renormalization by electron occupancy. As the electrons are introduced into the sample, they fill up the LNC traps, renormalizing them into shallower traps, or possibly into obstacles. For $n < f_{LNC}$, this reduces the number of deep, unrenormalized traps, which are the primarily suppressants of the mobility. As the electron density exceeds the LNC density, $n > f_{LNC}$,

a trapped electron population equal to the number of LNCs dynamically renormalizes essentially all deep trap LNCs into shallow traps. This leaves the non-trapped excess $(n - f_{\mathrm{LNC}})$ electrons to move across the BNS that has the same trap density, but which are now renormalized into shallow traps. – In reverse, the $(n - f_{\mathrm{LNC}})$ density of non-trapped electrons decreases as f_{LNC} increases, thereby decreasing the mobility. Once f_{LNC} exceeds n, the mobility keeps decreasing with f_{LNC} until the unrenormalized deep traps percolate. The percolation of the unfilled/unrenormalized deep traps is only reached at f_{LNC} concentrations that exceed f_{P} by a quantity set by n. This explains the mobility minimum moving to higher f_{LNC} concentrations with increasing n.

Fig. 3.4 shows that when $\mathrm{E_C}$ is small (35 meV), and thus $\mathrm{E_C} < \Delta$, increasing n shifts the mobility minimum to higher f_{LNC}, as well as makes the minima shallower. Fig. 3.5 shows that when $\mathrm{E_C}$ is large, $\mathrm{E_C} > \Delta$, increasing n again shifts the mobility minimum to higher f_{LNC}, but without changing its depth. In the case of Fig. 3.4, LNCs with one trapped electron remain energetically capable of trapping additional electrons, as renormalized shallow traps Δ_r. In this situation, increasing n fills an increasing fraction of the LNCs with electrons, thereby decreasing the average trap energy in the NC film and thus resulting in a shallower and shallower mobility minimum. In addition, shallow traps next to deep traps make it easier for the trapped electrons to escape from the deep traps via a two-step process, thus further reducing the depth of the mobility minimum.

Fig. 3.5 shows that for large $\mathrm{E_C}$ (125 meV), since $\mathrm{E_C} > \Delta$, the LNCs that have trapped one electron become energetically incapable of trapping an additional electron, and are thus transformed into kinetic obstacles against transport. Therefore, each singly-occupied LNC becomes a lost trap, so increasing n again shifts the mobility minimum to higher f_{LNC}, but the average trap energy remains unchanged, and thus the depth of the minimum remains unchanged too, as shown in Fig. 3.5. In addition, increasing n increases the mobility at low f_{LNC} values.

3.1.4. Mobility as a function of size disorder. We briefly explored the effect of LNC size poly-dispersity on transport. Fig. 3.6 compares mobilities for LNC polydispersities of $\Sigma_{\mathrm{LNC}} = 0.08$ nm and 0.16 nm. We find that such an increase in polydispersity decreases the depth of the mobility minimum without changing its position. The site energy disorder, induced by the LNC polydispersity, has competing effects. Increasing disorder tends to decrease the mobility on the

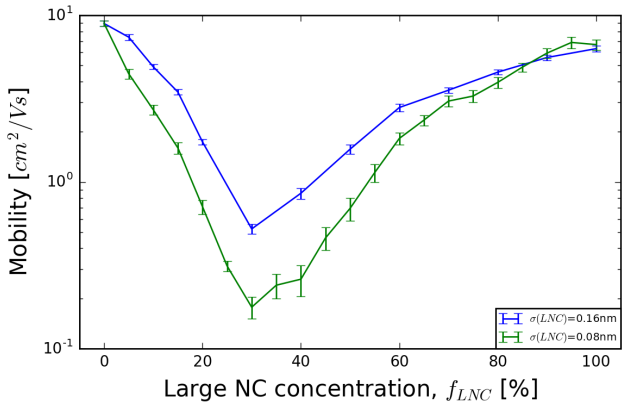

FIGURE 3.6. Mobility vs. f_{LNC} for an LNC size polydispersity of $\sigma_{\mathrm{LNC}} = 0.08$ nm and $\sigma_{\mathrm{LNC}} = 0.16$ nm. Electron density = 0.25 e/NC; $T = 80$K; SNC polydispersity $\sigma_{\mathrm{SNC}} = 0.01$ nm; $\mathrm{E_C} = 35$ meV.

LNC network itself. However, this same increased variation of the site energies makes some of the LNCs into shallower traps, enhancing the mobility. In the present case, the latter of the two effects seems to be more impactful.

For completeness, we also explored the effect of size polydispersity, or simply size disorder, on transport in a NC solid with NC diameters distributed according to a single Gaussian centered on a mean of 3.5 nm. Fig. 3.7 shows the mobility as the size disorder is increased at two different temperatures, $T = 80$K and $T = 300$K. Without the competing effects described above in the context of BNSs, in polydisperse NC solids with a Gaussian size distribution increasing disorder simply supresses the mobility, and drives the NC solid further into a disorder-localized phase.

3.1.5. Mobility as a function of ligand length. We simulated transport for ligand lengths of 0.6 nm and 0.8 nm, resulting in NC-NC separations of 1.2 nm and 1.6 nm respectively. The larger inter-NC spacing reduces the entire mobility curve by a multiplicative factor, the ratio of the tunneling factors that depend on the ligand length exponentially. Varying the ligand length did not change the depth or position of the mobility minimum.

3.1.6. Transport Heat Maps. We visualized the transport through the percolating network by building heat maps that show the time-integrated electron occupancy for each NC during the simulation. At periodic instants we recorded the location of each electron, and overlaid all these images. Thus, an NC appearing darker indicates more electrons spending longer times on that NC.

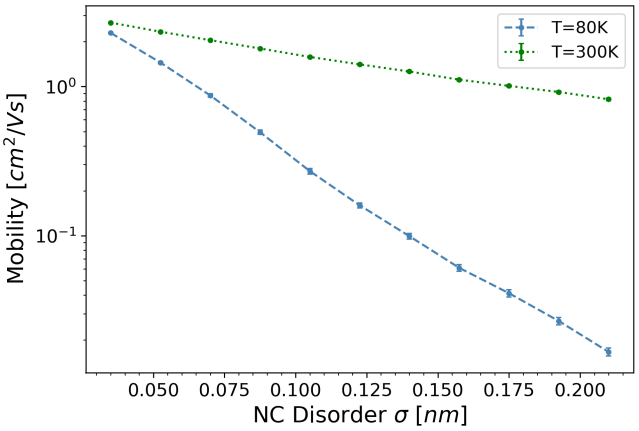

FIGURE 3.7. Mobility vs. NC size polydispersity σ, at T = 80K and T = 300K. Monodisperse NC solids with mean diameter = 3.5 nm; electron density = 0.25 e/NC.

Figs. 8-9 show heat maps for several different f_{LNC} values, with an electron density equal to 0.25 e/NC in a BNS with $\mathrm{E_C} < \Delta$. At f_{LNC}=0, the sample consists only of SNCs: the heat map is very homogeneous, and the mobility is high. At f_{LNC}=0.05, the LNCs act as isolated traps, but most electrons can avoid the sparse traps and propagate via the SNC matrix. For f_{LNC}=0.10, the LNC traps start to capture a substantial fraction of the propagating electrons. For f_{LNC}=0.15, most the electrons spend most of their time captured in the LNC traps. These traps are isolated, or form small clusters. At f_{LNC}=0.20, the LNC clusters nearly interconnect. The mobility decreases in the entire range of LNC concentrations from f_{LNC}=0 to f_{LNC}=0.20.

At $f_{\mathrm{LNC}} = 0.30$, the first sample-spanning LNC clusters appeared. The formation of these percolation networks causes the mobility to begin increasing. At $f_{\mathrm{LNC}} = 0.40$, the percolation networks densify, greatly helping the mobility to recover. Finally, at f_{LNC}=1.00, the occupancy heat map becomes quite homogeneous, comparable to the map at $f_{\mathrm{LNC}} = 0$. These images give a clear visual support to the physical picture developed above: as f_{LNC} starts to increase from zero, the LNCs serve as traps and thus suppress the mobility. When the LNCs percolate, then the traps suddenly form new transport channels and start increasing the mobility. Therefore, the mobility forms a minimum at the percolation threshold f_{P}, modified by the electron density n. As f_{LNC} grows towards $f_{\mathrm{LNC}} = 1.00$, the transport can again flow through the entire NC matrix.

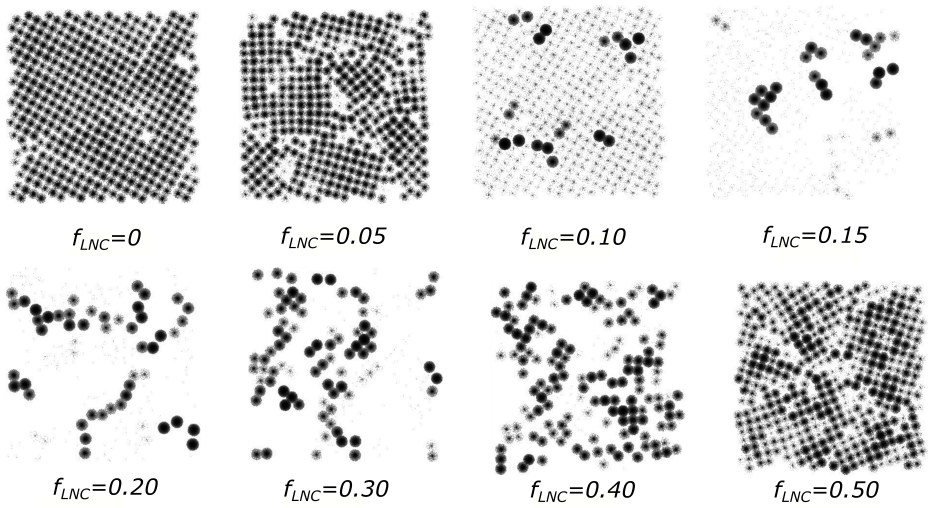

FIGURE 3.8. Electron occupancy heat maps for a typical BNS for different values of f_{LNC}. Shading indicates the time-integrated probability of each NC being occupied by electrons.

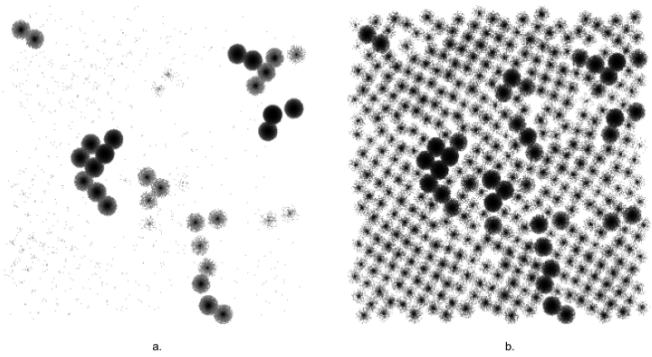

FIGURE 3.9. Temperature dependence of the electron occupancy maps for a typical BNS at (a) $T = 80$K and (b) $T = 300$K.

Fig. 3.9 shows the effect of temperature on the heat maps of a typical BNS. Electron transport pathways are dominated by the deep traps at $T = 80$K, giving rise to a very uneven heat map. At $T = 300$K, thermal energy is reasonably effective at freeing the trapped electrons, so the electron transport is more homogeneous throughout the sample. This translates to a higher mobility at higher temperatures, which is consistent with the smoothing out of the mobility minimum at $T = 300$K, reported above in Fig. 3.3.

3.2. Discussion and Conclusions

We simulated and fabricated field-effect transistors (FETs) made from a mixture of PbSe NCs with diameters of 6.5 nm and 5.1 nm, thereby forming a binary nanocrystal solid (BNS). We used our Hierarchical Nanoparticle Transport Simulator to model the transport in these BNSs, and study the impact of several factors on this transport. The BNS mobility exhibited a minimum at a large-NC-fraction $f_{\mathrm{LNC}} = 0.25{=}0.25$. The mobility minimum was deep at $T = 80$K and partially smoothed at $T = 300$K. We developed the following physical picture to account for this behavior. As the LNC fraction f_{LNC} within the SNC matrix starts growing from zero, the few LNCs act as deep traps for the electrons traversing the SNC matrix. Increasing the f_{LNC} concentration of these traps decreases the mobility. As the increasing f_{LNC} reaches the percolation threshold $f_{\mathrm{LNC}}{=}f_{\mathrm{P}}$, the LNCs form sample-spanning networks that enable electrons to traverse the entire BNS via low-energy, low disorder LNC pathways. The opening of the new transport channel through these percolating LNC pathways leads to the recovery of the mobility as f_{LNC} grows past f_{P}. Therefore, the electron mobility exhibits a pronounced minimum as a function of f_{LNC} at $f_{\mathrm{LNC}}{=}f_{\mathrm{P}}$. We have studied the effect of temperature, electron density, charging energy, ligand length, and disorder on the mobility minimum. To account for all trends, we have proposed that capturing an electron renormalizes a deep trap LNCs into either a shallow trap or a kinetic obstacle, depending on the value of the charging energy $\mathrm{E_C}$ relative to the NC energy difference Δ. A central prediction of this model is that the position of the mobility minimum shifts to a larger LNC fraction $f_{\mathrm{LNC}} > f_{\mathrm{P}}$ as the electron density increases, but its depth is modified differently depending on whether $\mathrm{E_C} < \Delta$, or $\mathrm{E_C} > \Delta$. Finally, we verified our expectations and physical picture by constructing and analyzing heat maps of the mobile electrons in the simulated BNS.

CHAPTER 4

Disordered Mott-Hubbard Physics in Nanoparticle Solids: Transitions Driven by Disorder, Interactions, and Their Interplay

This work appeared as Nano Letters 20, 8569–8575 (2020).

Quantum Confined localization drives NP solids insulating, hindering charge transport and thus their utility. Therefore, driving NP solids from their insulating phase across a Metal-Insulator Transition (MIT) into a conducting, metallic phase is a top priority to boost their utility. Recent experimental attempts to cross the MIT included atomic layer deposition (ALD), [**44**] substitutional percolation, [**42**] chemical doping, [**39**, **40**] and photodoping [**41**]. ALD infilling with metal oxides already enhanced mobilities above 7 cm^2/Vs [**44**]. Whether these enhanced-mobility NP solids support coherent metallic transport is still debated. Building on these advances, NP solar cells were developed with impressive 13-16% power conversion efficiencies [**27**, **28**, **29**].

There is a vast literature on the theory of the disorder-driven, "Anderson"-type MIT of non-interacting electrons [**90**]. The disorder of the site energies breaks up the site-to-site phase coherence of the originally extended wavefunctions, thereby localizing the electrons. Introducing interactions into Anderson localizaton makes the physical scenarios more complex, as revealed by scaling methods [**91**, **92**, **93**]. Implications for transport were studied, e.g., via the concept of the "Coulomb blockade/gap", the energy cost of the attraction between the moving electron and the hole it leaves behind, thus suppressing transport at all fillings [**94**]. These ideas were adapted to NP solids e.g. in Ref. **39**. Transport has been described as nearest neighbor hopping at high T [**70**, **95**], and as Efros-Shklovskii (ES) variable range hopping at low T [**96**].

Interactions are especially important at commensurate fillings. An electron already on an NP blocks the transport of additional electrons through that same NP because of the Coulomb cost of double occupancy. This was referred to as a Mott-gap, or Coulomb blockade. This blockade fully blocks transport only at integer fillings [**47**, **48**, **51**]. In recent years, the analysis of the

interplay of disorder and interactions was re-energized by adaptating the Dynamical Mean Field Theory (DMFT) for analogous Hubbard models [**97**, **98**, **99**]. A surprising prediction of DMFT was that at n=1, at intermediate repulsion, increasing disorder first dissolved the Mott-localized phase into a metal, which then transformed into a Anderson-localized phase only at a higher disorder. Accordingly, the gap of the Mott-localized phase did not persist into the Anderson-localized phase with increasing disorder [**98**, **99**]. Fillings $n \neq 1$ were not yet investigated with DMFT.

Remarkably, despite all this progress, profound unmet needs remain. (1) In spite of inviting analogies, the vast amount of knowledge developed for the disordered Mott-Hubbard physics has not yet been adapted for NP solids, beyond some early suggestions [**100**, **101**, **102**, **103**, **104**, **105**]. For example, even though the mobility of some NP solids exhibits maxima and minima as the filling is tuned, these features were not attributed to Mott-Hubbard commensuration [**87**]. Adapting Hubbard-based knowledge to nanomaterials could inspire new pathways to improve the transport properties of NP solids. In reverse, articulating these connections could make nanoparticle solids a rich and well-controlled testing ground for Hubbard-based research.

(2) We are not aware of a theory of the MIT that starts from the insulating phase either in NP solids, or in the Mott-Hubbard field. Notably, both the scaling and the DMFT techniques are built with extended wave functions, and thus indicate Anderson/disorder localization only as the boundary where their applicability breaks down. Therefore, they are ill-suited to describe the Disorder-localized phase itself. Thus, developing a theory of the MIT out of the insulating phase would complement the MIT theories from the metallic phase, thus creating a comprehensive characterization of the MIT.

In response to these needs, here are the main messages of our paper. (1) We advocate that adapting disordered Mott-Hubbard ideas for NP solids, and viewing NP solids as well-controlled experimental platforms for Mott-Hubbard models, provides extensive benefits for both fields. (2) To start this adaptation, we developed a Hierarchical Nanoparticle Transport Simulator to reach the MIT from the localized phase; and we analyzed a multi-orbital Hubbard model with DMFT to reach the MIT from the delocalized phase. Using the combination of these complementary methods we determined the comprehensive phase diagram of Nanoparticle solids that consists of two distinct localized phases defining two distinct MITs, which can be crossed by tuning various control

parameters. (3) Tuning the filling n towards integer values drives a Disorder-localized–to–Mott-localized transition. (4) For n=1 and large interactions, decreasing disorder drives a direct Disorder-localized–to–Mott-localized transition without an intervening metallic phase, characterized by a persistent gap. (5) For $n \neq 1$, decreasing disorder drives a Disorder-localized–to–Metal, Anderson-like MIT. (6) The DMFT-determined filling-dependence of the mobility at low disorder shows striking similarities to that at high disorder, demonstrating the internal consistence of our analysis.

The HINTS method: Our **HI**erarchical **N**anoparticle **T**ransport **S**imulator HINTS is a kinetic Monte Carlo transport simulator that is extended by an additional metallic transport channel. This extension makes HINTS capable of reaching the MIT from the insulating phase. In an introductory analysis at generic fillings, we reported reaching the MIT and interpreted it as a Quantum Percolation Transition [**50**]. However, we did not connect this MIT to Mott-Hubbard phenomena, did not consider its interplay with Anderson localization, and did not analyze the model at commensurate fillings.

In our extended HINTS, modified from chapter 2, the NP-NP transition rates are either Miller-Abrahams phonon-assisted hoppings, or non-activated metallic transitions, depending on whether the energy difference between the initial and final states was larger or smaller than a hybridization energy:

$$\Gamma_{i\to j} = \begin{cases} \nu g_{ij}\beta_{ij} \exp\left\{\left(\frac{-\Delta E_{ij}}{k_b T}\right)\right\} & \text{if } \Delta E_{ij} >= E_{\mathrm{H}} \\ \nu g_{ij}\beta_{ij} & \text{if } \Delta E_{ij} < E_{\mathrm{H}} \end{cases} \tag{4.1}$$

The hybridization energy E_H depends on the electron wavefunction overlap between NPs i and j, and for simplicity is taken to be approximately equal to the half bandwidth $2t$, where t is calculated by mapping our tunneling probabilities to Fermi's golden rule. The attempt frequency ν is chosen to be $10^{12}\,\mathrm{s}^{-1}$ to match experimental data, g_{ij} is the product of the initial density of states on NP_i and the final density of states on NP_j, and β_{ij} is the WKB tunneling amplitude. The hybridization energy E_H is determined by the overlap of the electron wavefunctions of NPs i and j.

See Chapter 2 for the full details of the HINTS method. We move to presenting the results of the HINTS simulations.

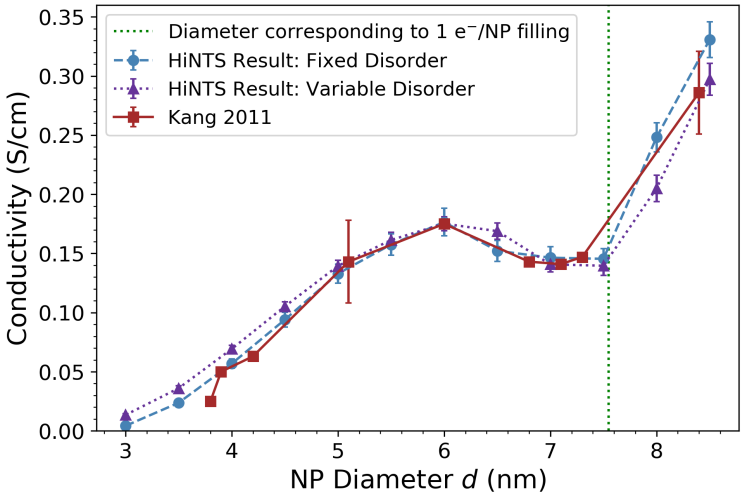

FIGURE 4.1. Conductivity v. NP diameter. HINTS simulations of PbSe NPs overlaid with exp. data. Volumetric electron density .0016 e/nm^3, ligand length 0.5 nm, $T = 200\text{K}$.

Disorder-localized–to–Mott-localized transition with a scan of the filling n: Experimentally, the electron/NP filling n can be scanned by increasing the average NP diameter at a fixed volumetric charge density. Two experimental groups measured the dependence of the mobility on the NP diameter in NP-FETs, and reported an initial rise followed by a maximum [**31**, **87**].

We now use HINTS to compute the conductivity of PbSe NP solids as a function of NP diameter d. Fig. 4.1 shows the HINTS-computed conductivities with increasing d for two representations of the disorder: fixed diameter disorder of ± 0.3 nm, and variable diameter disorder of $\pm 5\%$. These results are overlaid on the experimental data of Kang *et al* [**87**]. The HINTS conductivities and the Kang *et al.* data exhibit remarkable agreement.

The broad rising trend of the mobility/conductivity is driven by two factors: (i) larger d means that the electrons can traverse a fixed length by fewer hops; and (ii) since the electron energy-diameter relationship flattens with increasing d, the energy disorder induced by the diameter disorder decreases with increasing d.

The Kang experiments and our simulations both display a non-monotonic pattern overlaid on this broad rising trend. Conspicuously, the conductivity maximum at d=6 nm is observed to

be only the beginning of a maximum-minimum-resumed rise pattern, centered on $n = 1$. The utility of adapting Mott-Hubbard ideas to analyze NP solids is compellingly demonstrated here by recognizing that such a conductivity minimum also arises when n is scanned across $n = 1$ in the repulsive Hubbard model, as the Coulomb repulsion opens a Mott gap at $n = 1$, and thus suppresses transport through the occupied NPs. For context, we mention that earlier experiments [**31**] reported only a mobility maximum/ plateau, which we reproduced by simulation [**49**]. However, neither works observed the maximum-minimum pattern, and correspondingly did not recognize that Mott-Hubbard commensuration physics drives all these phenomena.

Changing d also varies site energies and hopping rates, and thus convolutes the transition into the Mott-localized phase with other trends. Therefore, next we isolate the mobility's dependence on n in *fixed diameter* NP solids. Experimentally this can be achieved by varying the FET gate voltage applied to a NP solid.

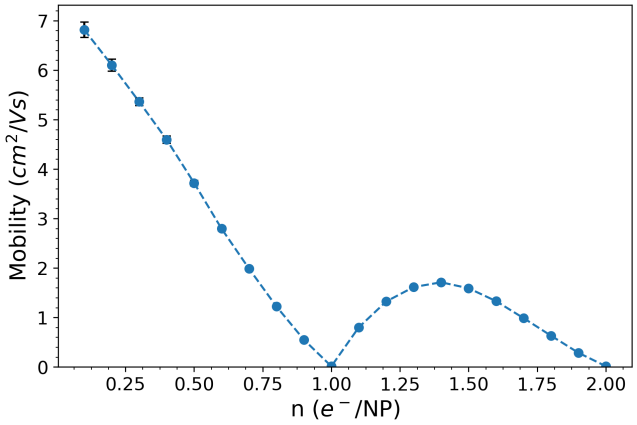

FIGURE 4.2. Electron mobility as a function of carrier filling in the disorder-localized Phase of PbSe NPs with diameters of 6.6 ± 0.3 nm. $T = 80$K. Average charging energy $E_c = 100$meV, average hopping energy $t = 7$meV.

Fig. 4.2 shows the HINTS-simulated mobility of a PbSe NP solid as n is varied. Visibly, the mobility exhibits minima at integer fillings, accompanied by maxima close to half-integer fillings, just as with increasing d. These features are much more pronounced than in Fig. 4.1.

The temperature dependence of the mobility/conductivity is activated for all fillings in Figs. 4.1 and 4.2, having a smaller, disorder-induced gap away from $n = 1$, that is boosted by the Coulomb

blockade to a larger gap at $n = 1$. Thus, scanning with n through $n = 1$ crosses from a Disorder-localized phase into a Mott-localized phase, and then back to a Disorder-localized phase for $n > 1$, as expected from adapting the Hubbard model for these NP solids. And in reverse, the fact that the experimental data and our simulations show such a remarkable correspondences is compelling evidence that NP solids are well-controlled and tunable experimental realizations of the disordered Hubbard model.

Experimentally, such filling-driven Disorder-localized–to–Mott-localized phase transitions have been reported in Si quantum dot arrays, where the gate voltage was used to tune the filling [**102**], and in InAs quantum dot solids [**106**].

Mott-localized–to–Disorder-localized transition with a scan of disorder W at n=1:

Next, we explore the robustness of the Mott-localized phase as the disorder $W/2t$ is varied at fillings around $n = 1$. Here the Hubbard t kinetic energy was determined by mapping our tunneling probabilities to Fermi's golden rule. W was determined from the sum of the disorder of the band and charging energies. We conduct this study on PbSe NP solids with a mean diameter of 6.5 nm by scanning the diameter dispersity up to 10%.

Fig. 4.3 shows the dependence of the activation energy/ gap Δ on the disorder $W/2t$ at n=1 (scan 3a), and at $n = 1+\delta$ where $\delta = 0.001$ (scan 3b). At n=1 and small disorder the gap Δ is Mott-like, as its value is set by the charging energy E_c: $\Delta/E_c \approx 1$. This Mott gap suppresses transport, and creates a Mott-localized phase. With increasing disorder, the gap Δ gets renormalized to a lower value $\Delta(W)$. The physics of this lower gap region is clarified by scan 3b of $\Delta(W)$ at the filling $n = 1 + \delta$. The gap $\Delta(W)$ is the same for $n = 1$ and $n = 1 + \delta$ above a critical value $W_c(Mott)/2t \approx 3.5$. This insensitivity of the gap to the charging energy and to commensuration identifies this phase as a Disorder-localized phase, into which the Mott-localized phase of n=1 transitions as W exceeds $W_c(Mott)$. Clearly, the transition at $n = 1$ across $W_c(Mott)$ is direct, in the sense of having a persistent gap across the transition and no intervening gapless metallic phase. An analogous direct Mott-to-Anderson transition was reported by DMFT studies with a disorder scan in the Hubbard model at n=1 at around $W_c(Mott) = 3$, in good agrement with our result. Both studies worked in the $U/t = 10 - 14$ range. [**98**] It is noteworthy that the gap is

relatively insensitive to W in the Disorder-localized phase. This is explained by the charging energy E_c screening the disorder W.

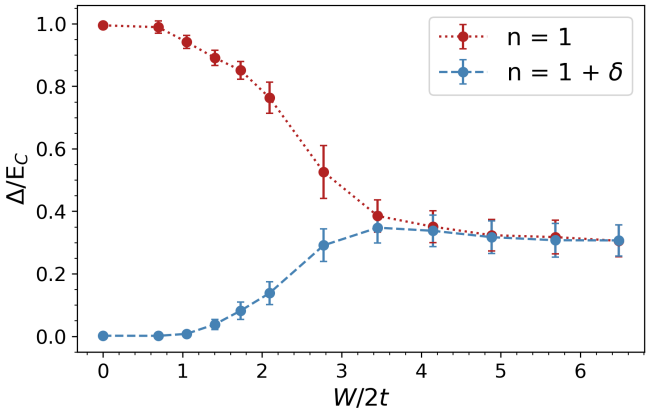

FIGURE 4.3. The disorder dependent gap Δ (W) for PbSe NPs: (a) $n = 1$; (b) $n = 1 + \delta$. $W_c(Mott)/2t \approx 3.5$; $W_c(MIT)/2t \approx 1.5$.

Beyond the remarkable disorder driven Mott-localized–to–Disorder-localized transition at n=1, scan 3b also reveals that as the disorder W is reduced at $n = 1 + \delta$, the gap shrinks to zero at $W_c(MIT)/2t \approx 1.5$. The vanishing of the gap indicates the disorder below which the wavefunctions become delocalized again. In this regime, the phases of the wafunctions become important, and the metallicity of transport is restored. HINTS does not track the phases of the electron wavefunctions, and thus can describe the transport with decreasing disorder only down to $W = W_c(MIT)$, but cannot enter the metallic phase itself. We identify $W_c(MIT)$ as indicating a Disorder-localized–to–Metal Transition, taking place at $n \neq 1$. This MIT at $W_c(MIT)$ at $n = 1+\delta$ is disorder-driven, and is therefore distinct from the interaction-driven Mott transition at $W = W_c(Mott)$ at $n = 1$.

For context, we comment on the expectation that all electronic states are localized in 2D. This expectation, however, was demonstrated only in non-interacting systems. [**90**]. In interacting systems, the complex interplay of interactions and disorder has been shown to drive Metal-Insulator delocalization transitions starting from the extended phase even in 2D. [**93**, **107**, **108**] Our results, building from the insulating phase, are consistent with and complement these claims.

These results have direct experimental relevance for NP solids beyond just PbSe NPs. Ref. **40** developed strategies to cross the MIT and induce band-like transport with the high mobility of 27 cm^2/Vs in CdSe NP FETs by increasing the kinetic energy t and decreasing the disorder W. Ref.

40 increased the wavefunction overlap, and thus t, by switching to the compact ligand thiocynate, and by annealing at the elevated temperatures of T=200C-250C. They eventually reached values of $t = 6 - 8$meV. They also reduced W by doping the CdSe NP FETs with Indium that filled up traps and thus reduced the trap-related disorder, eventually giving rise to an effective gap of $\Delta = 6 - 7meV$.

Our simulations provide a firm foundation for these strategies. To establish a quantitative correspondence, one would need to redo our PbSe simulation for CdSe NP solids to determine the additional disorder from polydispersity. Without the benefit of this calculation, we only make the qualitative observation that the $W/2t$ ratio where Ref. **40** reports an MIT is of the order 1, and thus consistent with our $W_c(MIT)/2t = 1.5$.

An additional strategy emerges from our simulations: the reduction of the charging energy E_c. We showed that E_c sets the Mott gap and screens the gap in the Disorder-localized phase, thus reducing E_c is yet another strategy to cross the MIT in NP solids.

Disordered-metal–to–Mott-localized transition as a function of n: We already established that the physics of NP solids is analogous to a disordered Hubbard model whose sites represent the individual NPs. We take into account the 8-fold degeneracy of the electronic states of the PbSe NPs [**109**] by adopting a four orbital (labeled by $a, b = 1, 2, 3, 4$) Hubbard model with diagonal disorder [**110**]. The Hamiltonian reads:

$$H = \sum_{\langle i,j\rangle,a,\sigma} t_{ij} d^{\dagger}_{i,a,\sigma} d_{j,a,\sigma} + \sum_{i,a,\sigma} (w_i - \mu) n_{i,a,\sigma} + \sum_{a} U n_{a,\uparrow} n_{a,\downarrow} + \sum_{a \neq b,\sigma,\sigma'} U n_{a,\sigma} n_{b,\sigma'}. \tag{4.2}$$

Here $\langle i, j\rangle$ label nearest neighbor sites, $n_{i,a,\sigma} = d^{\dagger}_{i,a,\sigma} d_{i,a,\sigma}$ is the density of electrons of spin σ in orbital a on site i, μ is the chemical potential, t_{ij} is the nearest neighbor hopping, and U is the Coulomb repulsion. The disorder is introduced through the random site potential energy w_i, independent of orbital and spin index. For further details, see Appendix A.

The NP solid is on a regular lattice to start from a bona fide metallic state. We explore the combined effect of Coulomb repulsion and site energy disorder. We simulate PbSe NPs by associating the on-site Hubbard repulsion U with the NP charging energy by taking $U = E_c = 100$ meV, and the kinetic term with the NP-NP hopping amplitude of $t = 7$ meV, making $U/2t = 7$.

These parameters match those of Fig. 2, and thus our Hubbard model is to be viewed as a quantitative modeling of the PbSe NP solid.

Since $t/U << 1$, the Hubbard model is in strong coupling. Therefore, we adopt the Dynamical Mean Field Theory (DMFT), extended to include disorder effects [**97**, **98**, **99**, **111**].

The DMFT approach maps the original lattice model onto an auxiliary quantum impurity model supplemented with a self-consistency condition. The quantum impurity problem is then tackled by numerical simulations that we performed using the continuous-time quantum Monte Carlo (CTQMC) method [**112**, **113**], described in Ref.**114**. That method samples a diagrammatic expansion of the partition function in powers of the impurity-bath hybridization. For simplicity, for the non-interacting electrons we adopt a semi-circular density of states (DOS) of bandwidth $4t$, since single-site DMFT is not sensitive to the shape of the non-interacting DOS. DMFT is exact in infinite dimensions, and it has been shown to remain a good approximation for lower dimensional systems whose physics is local, as is the case for the present Mott system. The disorder is introduced through a random site energy with a uniform distribution in the interval $[-W, W]$ (see Appendix A for details).

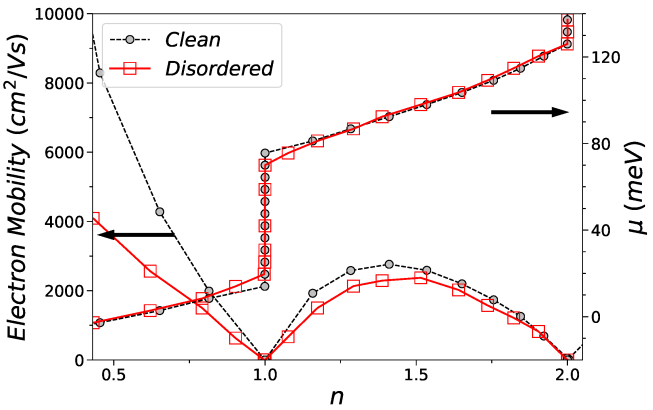

FIGURE 4.4. Mobility and chemical potential μ as filling scans from the Metallic Phase through the Mott gap.

Fig. 4.4 shows the electron mobility and the chemical potential μ of this Hubbard model as a function of the filling n for the clean and disordered cases, at T/t=0.02. In the clean case, μ shows a jump at $n = 1$: this indicates the emergence of a Mott gap that localizes the electrons [**110**]. This is a remarkable result, as our DMFT technique finds this Mott-localized phase at the band filling

of 1/8, whereas band structure calculations for PbSe, or traditional Hubbard mean-field theories would not find such a Mott insulator below the customary band filling of 1/2. So, our DMFT work establishes PbSe as a Mott system, where correlation effects play out in 4-fold degenerate orbitals.

At finite temperatures, this Mott gap makes the mobility exhibit a minimum as the filling crosses n=1. Clearly, DMFT established that the Mott gap/Coulomb blockade also suppresses the mobility in the metallic phase when the filling is scanned across $n = 1$, just like in the insulating phase (cf. Fig. 4.2).

A main result of the DMFT study is that the clean trends persist even for a substantial disorder $W/2t = 1$. Indeed, the Mott gap (jump of μ) at $n = 1$ only decreases by a small amount and remains robust. This is reasonable since $W/2t = 1 << W_c(Mott)/2t = 3.5$. At the same time, the mobility away from $n = 1$ is reduced much more notably because the $W/2t = 1$ disorder is relatively closer to the off-commensuration MIT at $W_c(MIT)/2t = 1.5$. Finally, Fig. 4.4 shows that the relative reduction of the mobility by the disorder is strongest at small n. This makes physical sense, since at small n the Fermi energy becomes comparable to the disorder, and thus the relative importance of the disorder grows. To our knowledge, the present DMFT study is the first one done for a multi-orbital model with disorder as a function of electron filling.

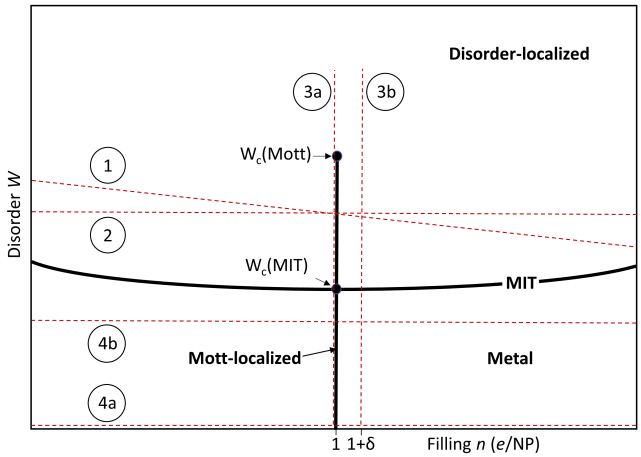

FIGURE 4.5. Qualitative phase diagram of NP solids in the (disorder W–filling n) space, for $U >> W$. The red dashed lines report the scans in the correspondingly labeled figures.

The here-used coherent potential CPA-DMFT method does not capture Anderson localization. While "typical medium" DMFT theories were proposed to capture a Mott-Anderson transition, this issue remains debated [**115**, **116**, **117**, **118**, **119**, **120**, **121**, **122**].

Conclusions: We now bring together all the scans of our complementary HINTS and DMFT work and construct the phase diagram of PbSe NP solids on the filling–disorder plane, shown in Fig. 4.5. We distinguished a Disorder-driven MIT at $n \neq 1$, and an Interaction-driven MIT at $n = 1$. In particular, at $n = 1$, HINTS showed that at large interactions the Mott-localized–to–Disorder-localized transition occurs with a persistent gap. We complemented the studies building from the localized phases with studies building from the extended phase. Reassuringly, the complementary studies produced the same qualitative scenarios, as illustrated by the strikingly similar behavior of the mobility in Figs. 4.2 and 4.4.

The totality of our studies demonstrated that adapting the vast body of knowledge developed for the disordered Mott-Hubbard model for NP solids can and will produce many new insights into the physics of NP solids, and thus can be used to develop strategies to improve their optoelectronic properties.

CHAPTER 5

Structural Characterization of a Polycrystalline Epitaxially-Fused Colloidal Quantum Dot Superlattice by Electron Tomography

This work appeared as Journal of Materials Chemistry A 8, 18254 (2020).

While improvements in colloidal semiconductor quantum dot (QD) processing, electronic performance and stability are ongoing, as discussed in prior chapters the use of QDs in many optoelectronic devices is limited by poor charge transport relative to bulk semiconductors. Poor transport is in part caused by energetic disorder arising from variations in QD size, spacing and other types of spatial disorder [**31**,**33**,**123**]. Epitaxially-fused PbX (X = Se, S) QD superlattices (epi-SLs) consist of PbX QDs that are arranged in a periodic lattice and epitaxially interconnected (necked or partially fused) to form a porous single crystal of "confined-but-connected" QDs. Epi-SLs promise to combine the tunable optical properties and processability of QDs with the high-efficiency band-like transport of bulk semiconductors [**124**]. However, charge transport studies have so far failed to demonstrate band-like transport in epi-SLs, probably because structural defects from the atomic scale to the mesoscale disrupt the SL periodicity and localize charge carriers [**106**, **125**].

Making PbX QD epi-SLs with larger lateral grain sizes is important for reducing the density of inter-grain structural defects (*e.g.*, grain boundaries, amorphous regions, and voids), but it is the several types of intra-grain defects that conspire to degrade spatial order within the grains, destroy mini-bands, and prevent the emergence of delocalized states [**33**, **106**, **123**]. Intra-grain defects include variations in QD and neck size and shape, missing necks, missing QDs (vacancies), misaligned QDs (edge dislocations, screws dislocations, and zig-zag jitter), larger-scale wave-like oscillations in QD position that result from flow of the QD film on the liquid surface (meander), and variations in the surface coverage of ligands, ions, and traps, all of which will scatter carriers and disrupt SL periodicity to some degree. Most of these defects have been observed in 2D epi-SLs (QD monolayers), which are readily imaged by conventional transmission electron microscopy (TEM)

and scanning transmission electron microscopy (STEM) [**33**, **46**, **125**, **126**, **127**, **128**, **129**, **130**, **131**, **132**, **133**, **134**, **135**]. Transport measurements of 2D epi-SLs show that carriers are localized, and several groups have proposed that missing necks are a primary cause of carrier localization in these materials [**33**, **46**]. Furthermore, the electronic coupling of necked QDs is expected to be sensitive to neck polydispersity (length, width, atomic coherence, and faceting) and the number of nearest neighbor QDs [**33**].

While 2D epi-SLs can be structurally characterized using traditional electron microscopy, imaging the internal details of 3D epi-SLs is more challenging [**43**, **130**, **136**, **137**]. Neck connectivity and projected neck size in 2D epi-SLs have been directly imaged by (S)TEM [**33**, **46**, **134**], and the three-dimensional structure of these necks was deduced from single images by high-angle annular dark-field (HAADF) STEM atom counting reconstruction [**130**]. To date, structural characterization of 3D epi-SLs has been almost exclusively limited to X-ray scattering and conventional electron microscopy imaging/diffraction methods [**4**, **43**, **125**, **138**], neither of which can visualize the intra-grain neck network or internal structural defects that are so important for understanding carrier delocalization in these materials. Electron tomography (ET) is a suitable tool for the near-atomistic structural characterization of 3D epi-SLs. The Vanmaekelbergh group has previously used ET to establish the basic unit cell of non-fused 3D binary [**139**, **140**] and ternary [**141**] QD SLs, 2D honeycomb epi-SLs [**128**], and thin multilayer honeycomb epi-SLs [**142**]. Savitzky *et al.* reported a tomogram of a fused 3D PbS QD SL made at high pressure, but no assessment of necks or structural defects was presented [**143**].

Here we present an in-depth and quantitative structural analysis of a 3D PbSe QD epi-SL using electron tomography. We show that with a full-tilt HAADF ET reconstruction of a disc-shaped epi-SL film (120 nm in diameter $\times$ 38 nm tall), we are able to achieve sufficient spatial resolution (0.65 nm) to determine the position of all 1,846 QDs and the size and shape of all necks in the sample. From the center-of-mass coordinates of the QDs, we find that the sample consists of three SL grains and assign the unit cell and in-plane crystallographic orientation of each grain as well as the 3D structure of the grain boundaries. The epi-SL grains have a distorted simple cubic structure with lattice parameters in agreement with our previous results [**4**]. Maps of the neck locations and diameters reveal that the sample has an average of 3.7 necks per QD (giving

an overall network connectivity of 72%) and an average neck diameter of 4.1 nm (64% of the QD diameter). The three grains show similar distributions of neck number (necks per QD) but very different distributions of average neck diameter, reflecting significant inhomogeneity between the adjacent grains. We discover a weak positive correlation between neck number and diameter and a strong negative correlation between neck number and both the average and standard deviation of the nearest neighbor QD distance, indicating that QDs with more necks tend to have more ordered local environments. Kinetic Monte Carlo charge transport simulations show that the SL grain boundaries have little impact on carrier mobility because the three grains are interconnected by many necked QDs. The detailed and comprehensive understanding of various structural features gained from our statistical analysis of this relatively disordered polycrystalline sample can potentially inspire synthesis of 3D PbX QD epi-SLs of better structural perfection for realizing delocalized charge transport.

Note: supporting information for this chapter is available at [**80**]. Figure references in this chapter whose labels begin with an S refer to figures found in the supporting information.

5.1. Experimental

5.1.1. Materials. Lead oxide (PbO, 99,999%), Lead iodide (PbI_2, 99.9985%, purchased from Alfa Aesar), oleic acid (OA, technical grade, 90%), diphenylphosphine (DPP, 98%), 1-octadecene (ODE, 90%), ethanol (99.5%, anhydrous), ethylene glycol (EG, 99.8%, anhydrous), acetonitrile (99.99%, anhydrous), hexanes (≥99%, anhydrous), toluene (99.8%, anhydrous), (3-mercaptopropyl) trimethoxysilane (3-MPTMS, 95%), and N,N-dimethylformamide (DMF, 99.8%, anhydrous) were purchased from Sigma Aldrich and used as received. Trioctylphosphine (TOP, technical grade, >90%) and selenium (99.99%) were acquired from Fluka and mixed for 24 hours to form a 1 M TOP-Se stock solution. Ethylenediamine (EDA, >98.0%, anhydrous) was purchased from TCI and mixed with acetonitrile in a 1:1 volume ratio to make a 7.5 M EDA stock solution.

5.1.2. Quantum Dot Sythesis. PbSe QDs were synthesized and purified using standard air-free techniques. PbO (1.50 g), OA (5.00 g), and ODE (10.00 g) were mixed and degassed in a three-neck round-bottom flask at room temperature. The mixture was heated to 120 °C under vacuum to form dissolved $Pb(OA)_2$ and dry the solution. After 1 hour at 120 °C, the $Pb(OA)_2$

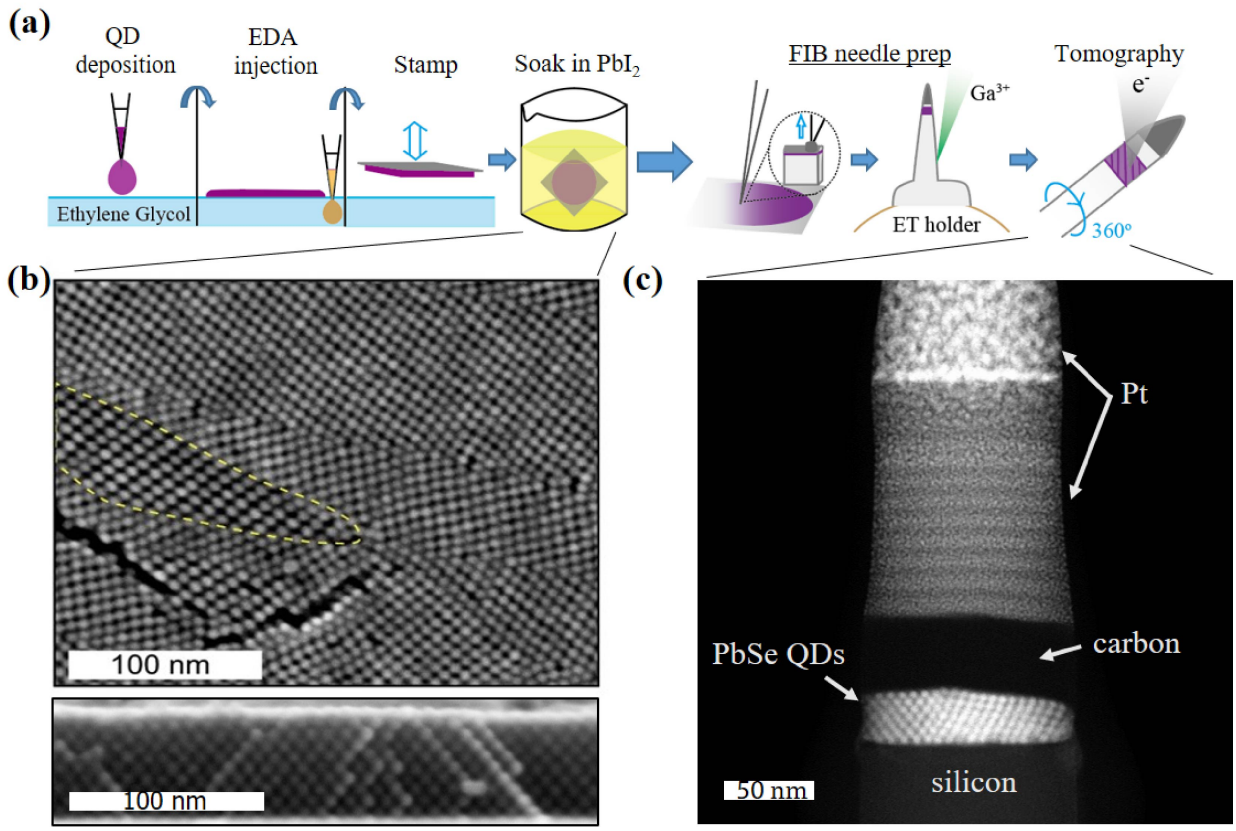

FIGURE 5.1. Fabrication of the PbSe QD epi-superlattice tomography sample. (a) Sample fabrication. (b) Plan-view and cross-section SEM images of a different region of the epi-SL film. The film is a polycrystalline SL with SL grains of two different in-plane orientations, previously assigned to the $(100)_{SL}$ and $(01\bar{1})_{SL}$ projections of a distorted simple cubic SL. [**4**] Most of the SL grains in this image have a $(100)_{SL}$ orientation. The dashed yellow line encircles a $(01\bar{1})_{SL}$-oriented grain. Scale bars are 100 nm. (c) HAADF-STEM image of the needle-shaped tomography sample with disc-shaped epi-SL layer and all layers labeled. Scale bar is 50 nm.

solution was heated to 180 °C under argon flow and 9.5 mL of a 1 M solution of TOP-Se containing 200 μL of DPP was rapidly injected into this hot solution. An immediate darkening of the solution was observed, and the QDs were grown for 105 seconds at ∼160 °C. The reaction was quenched with a liquid nitrogen bath and injection of 10 mL of anhydrous hexanes. QD purification and SL fabrication were performed in glove boxes with <0.5 ppm O_2 content. The QDs were purified by two rounds of precipitation/redispersion using ethanol/hexane and stored as a powder in the glove box.

5.1.3. Substrate preparation. A single-side polished Si substrate was cleaned using 10 minutes of sonication in acetone, Millipore water, and then isopropanol, followed by drying in a stream of flowing air. The cleaned substrate was immersed in a 100 mM solution of 3-MTPMS in toluene for 1 hour to functionalize its native SiO_x surface for improved epi-SL adhesion, then rinsed with neat toluene and dried in flowing air.

5.1.4. Superlattice fabrication. An oleate-capped superlattice was prepared in the glovebox by drop casting 70 μL of a 4 g/L dispersion of PbSe QDs in hexanes onto 6 mL of ethylene glycol (EG) in a Teflon well (3.5 $\times$ 5 $\times$ 1 cm). After depositing the QD solution, the well was immediately covered with a glass slide. The hexane evaporated over 30 minutes, resulting in a smooth, dry QD film floating on the EG surface. The glass slide was then removed and 0.1 mL of a 7.5 M solution of ethylenediamine in acetonitrile was slowly injected (5-10 sec) into the EG under the QD film using a 500 μL Hamilton syringe. After 30 seconds of exposure to EDA, the resulting epi-SL film was stamp transferred to the Si substrate using a vacuum wand, rinsed vigorously with acetonitrile and dried under flowing N_2. The epi-SL film was then immediately immersed in a 10 mM solution of PbI_2 in DMF for 5 minutes, rinsed thoroughly with acetonitrile and dried under flowing N_2. This procedure is nearly identical to the one used in our previous report [**4**] and yields epi-SL films with similar SL unit cell, grain size, and homogeneity, including degree of QD necking, coverage of the substrate, and density of cracks. However, the film for this tomography study is somewhat thinner (40 nm *vs.* 50-80 nm) and have a higher density of intra-grain extended defects (e.g., partial twins) because it was prepared in a glove box with a higher O_2 concentration (5 ppm *vs.* <0.1 ppm).

5.1.5. Basic characterization. Optical absorbance measurements of QDs dispersed in TCE were performed with a PerkinElmer Lambda 950 spectrophotometer. Neat TCE served as the background for the solution measurements. Scanning electron microscopy was performed on both an FEI Magellan 400L XHR SEM operating at 10 kV and 25-50 pA and a JEOL JEM-2800 TEM (with a secondary electron detector) operated in STEM mode with a 1.0 nm probe size.

5.1.6. Grazing incidence small-angle X-ray scattering. GISAXS measurements were performed on Beamline 7.3.3 of the Advanced Light source (ALS) at Lawrence Berkeley National Laboratory using 10 keV monochromatic X-rays (λ = 1.24 Å) with an energy bandwidth of 1%.

For GISAXS measurements, SL films were prepared on Si substrates and transported with the QD suspensions to the ALS under nitrogen to minimize air exposure prior to measurement. However, measurements were performed in air. A Dectris Pilatus 2M detector with a pixel size of 0.172 × 0.172 mm and 1475 × 1679 pixels was used to record the 2D scattering patterns. A silver behenate standard was used to determine the sample-to-detector distance and beam center. Exposure times ranged from 0.2 to 30 s. The grazing angle of incidence was varied from 0.2° to 0.3°. Manual pattern fitting was performed using the IndexGIXS software package provided by Detlef Smilgies of the Cornell High Energy Synchrotron Source. The critical angles of the films were fit empirically (0.195° for the oleate-capped SLs and 0.21° for the epi-SLs) to capture the breadth of the Yoneda band.

5.1.7. Tomography needle sample preparation. An area of the epi-SL film suitable for FIB milling was located by SEM and tagged with a Pt fiducial marker deposited by electron-beam induced deposition (EBID) in an FEI Quanta 3D FEG DualBeam microscope. The sample was then coated with 50 nm of carbon using the pulse plasma mode of a Leica ACE200 evaporator and returned to the DualBeam for FIB milling, lift-out, and final needle preparation. Prior to milling, a ∼200 nm Pt capping layer was deposited onto the carbon-coated sample by EBID, followed by an additional ∼2000 nm of Pt deposited by ion beam induced deposition (IBID). The carbon layer serves primarily to enhance STEM imaging contrast by separating the epi-SL layer from the high-Z protective Pt capping layer. The area of interest was then FIB milled into a wedge shape (10 μm × 6 μm × 2 μm), lifted-out with an OmniProbe 400 nanomanipulator, ion welded to the tip of a sample holder for needle tomography samples (Single Point Tip, Hummingbird Scientific), and FIB milled again into a ∼130 nm diameter needle (Fig. S2). Milling was performed in several stages. The wedge was first milled into a pillar shape (1 μm diameter) using a 0.3 nA ion beam at 30 keV accelerating voltage, then thinned to a ∼200 nm diameter needle using 50 pA at 16 keV. Finally, a 5 minute ion beam shower (25 pA at 5 keV) was employed to sharpen the needle to ∼130 nm and remove surface damage. The finished needle contained a disc-shaped epi-SL layer (38 nm tall × 128 nm in diameter) for tomographic analysis.

5.1.8. HAADF-STEM Electron Tomography. The needle sample was mounted on the rotation axis of a Hummingbird Scientific single-tilt tomography holder (1000 Series) and imaged in a double aberration corrected JEOL JEM-ARM 300F TEM operated at 300 keV in STEM mode ($\sim$25 mrad semi-convergence angle). Two series of images were acquired, with HAADF and bright-field data recorded simultaneously (2k $\times$ 2k images) at each tilt angle. The first series consisted of 145 HAADF images spanning tilt angles over -78 to 67 degrees in 1 degree steps. The sample was then removed from the microscope, manually rotated on the sample holder by 86 degrees, and re-imaged from -68 to 78 degrees in 2 degree steps (resulting in 73 additional images). All 2D and 3D image processing was conducted in MATLAB unless otherwise noted. The two tilt-series were then merged using cross-correlation comparison (Fig. S4). The merged tilt-series include 181 images covering tilt angles from 0° to 226°. The image stack was then aligned vertically (along the rotation axis) by iteratively shifting the images to maximize the value of the 2D normalized cross-correlation function between adjacent images in the stack. Pixels outside of the epi-SL film were excluded from this cross-correlation calculation in order to maximize the quality of the vertical image alignment. Horizontal alignment of the images (normal to the rotation axis) was accomplished by converting each image to a 1D intensity profile and shifting the images to maximize the match between the 1D curves. The aligned image stack was then processed through two iterations of a Wiener image filter to remove noise. Tomographic reconstruction was carried out on the aligned and de-noised tilt-series using 200 iterations of the simultaneous iterative reconstruction technique (SIRT) in the ASTRA toolbox [**144**, **145**]. The raw reconstructed volume consisted of 2048 $\times$ 2048 $\times$ 700 voxels with edge lengths of 1 Å. The spatial resolution of this reconstruction was evaluated by the Fourier shell correlation (FSC) method to be 6.5 Å (Fig. S5).

The raw reconstruction was processed in two different ways. For analysis of the QD necks, the reconstruction was simply smoothed by a nonlinear anisotropic diffusion filter. Image processing for analysis of the QD positions was more involved. The raw tomogram was first filtered with a morphological 3D top-hat filter to minimize reconstruction intensity attenuation and enhance contrast. A top-hat filter was used to retain edge contrast instead of the more common Fourier filter [**146**] because Fourier filtering would erroneously remove necks between QDs and other important structural features present in the raw tomogram. To better emphasize the QD positions, the filtered

tomogram was convolved with a spherical 6.0 nm diameter QD kernel with a homogeneous intensity profile to obtain a 3D map of normalized cross-correlation (NCC) coefficients indicating the center of mass of each QD in the sample. Use of the 6.0 nm QD template is justified by the analysis of the average QD size and polydispersity from conventional dark-field STEM images (pixel size of 0.2 nm) of a different area of the same sample (Fig. S6). Prior to data analysis, the outer 6 nm of the cylinder-shaped tomogram was digitally removed to exclude QDs near the surface of the sample that were potentially deformed by the FIB milling process. To automate the measurement of neck dimensions, a script was written that defines a plane normal to each inter-QD axis and slides this plane along the axis to locate the minimum neck area. The neck diameter was then determined as the diameter of a circle of the same area.

5.1.9. Mobility Simulation. Mobility simulations were performed by again utilizing the Hierarchical Nanoparticle Transport Simulator (HINTS) kinetic Monte Carlo code presented in chapter 2. In this chapter, the HINTS code is expanded by the inclusion of an additional QD-to-QD transition mechanism: tunneling through the neck of epitaxially-fused QDs. In this new version of the code, after the energetics of the individual QDs are computed by *ab initio* methods, the QD-to-QD transitions of the charges are described by the following two mechanisms:

(1) Miller-Abrahams single phonon-assisted hopping between nearest neighbor QDs, as described in Chapter 2.

(2) Tunneling through the neck of epitaxially-fused QDs:

$$\Gamma_{\mathrm{i}\to\mathrm{j}} = \begin{cases} \frac{2\pi}{\hbar}|t|^2 g_{\mathrm{ij}} \exp\left(\frac{-\Delta E_{\mathrm{ij}}}{k_{\mathrm{b}}T}\right) & \text{if } \Delta E_{\mathrm{ij}} > OE, \\ \frac{2\pi}{\hbar}|t|^2 g_{\mathrm{ij}} & \text{if } \Delta E_{\mathrm{ij}} \leq OE \end{cases} \tag{5.1}$$

where $|t|$ is the QD-QD tunneling matrix element, and OE is an overlap energy. This transition channel represents that when a neck is formed between two QDs, their electronic states overlap and therefore hybridize. This hybridization induces a perturbation of the energy levels of the individual QDs, which we model by an overlap energy OE that is proportional to the neck diameter. The electronic states of those pairs of QDs whose energy level difference is less than OE: $\Delta E_{\mathrm{ij}} \leq OE$, hybridize to such a degree that they support a metallic $\mathrm{QD_i}$-to-$\mathrm{QD_j}$ transition instead of a hopping

one, paving the way toward the formation of a mini-band. The tunneling matrix element $|t|$ depends on the wavefunction overlap between the necked QDs. For its calculation, we adopt the approximation of Fu *et al.*: [**147**]

$$|t| = \frac{9\hbar^2 n\rho^3}{m^* d^2} \tag{5.2}$$

where n is the average electron volume density of the two quantum dots, ρ is the neck radius, m^* is the effective electron mass, and d is the average QD diamter. HINTS simulates nearest neighbor transitions and interactions; it does not include transitions to and interaction with farther neighbors.

On the next HINTS modeling layer, a QD epi-SL, is constructed. Simulations were performed on three types of epi-SL samples. First, the replica of the tomography sample was generated using the experimentally determined center-of-mass coordinates, QD diameters, and neck map of all three SL grains. Since the circular shape and uneven periphery of the tomography sample would make it harder to set up controlled transport simulations, QDs at the periphery of the sample were removed to reduce the simulation volume to the well-defined central cuboid of the tomography sample. To develop a comparative analysis of the transport of this tomography sample, we next generated two ensembles of over a thousand samples each to form a comparison basis. The first ensemble consisted of monocrystalline epi-SLs with the lattice parameters and neck statistics of grain I of the tomogram. The second ensemble consisted of bicrystalline epi-SLs with the same lattice parameters and neck statistics of grain I, but bisected by a plane of missing necks normal to the transport direction to create a necking grain boundary. The QDs in the latter two types of samples were assigned a diameter and lattice displacement vector according to the experimentally-determined Gaussian distributions.

Electron transport was simulated by first randomly placing electrons on QDs to fill the samples with a predetermined density of electrons. Based on work in previous chapters, we chose the electron density to be 0.5 electrons per QD, remaining far from commensuration to avoid Coulomb blockade effects [**81**]. A small voltage of 1 mV was then applied across electrical contacts on opposite sides of each sample to induce electron transport. Periodic boundary conditions were used. Throughout the simulation, we checked and ensured that the current-voltage characteristic stayed in the linear regime. The transport across every sample in both ensembles was simulated.

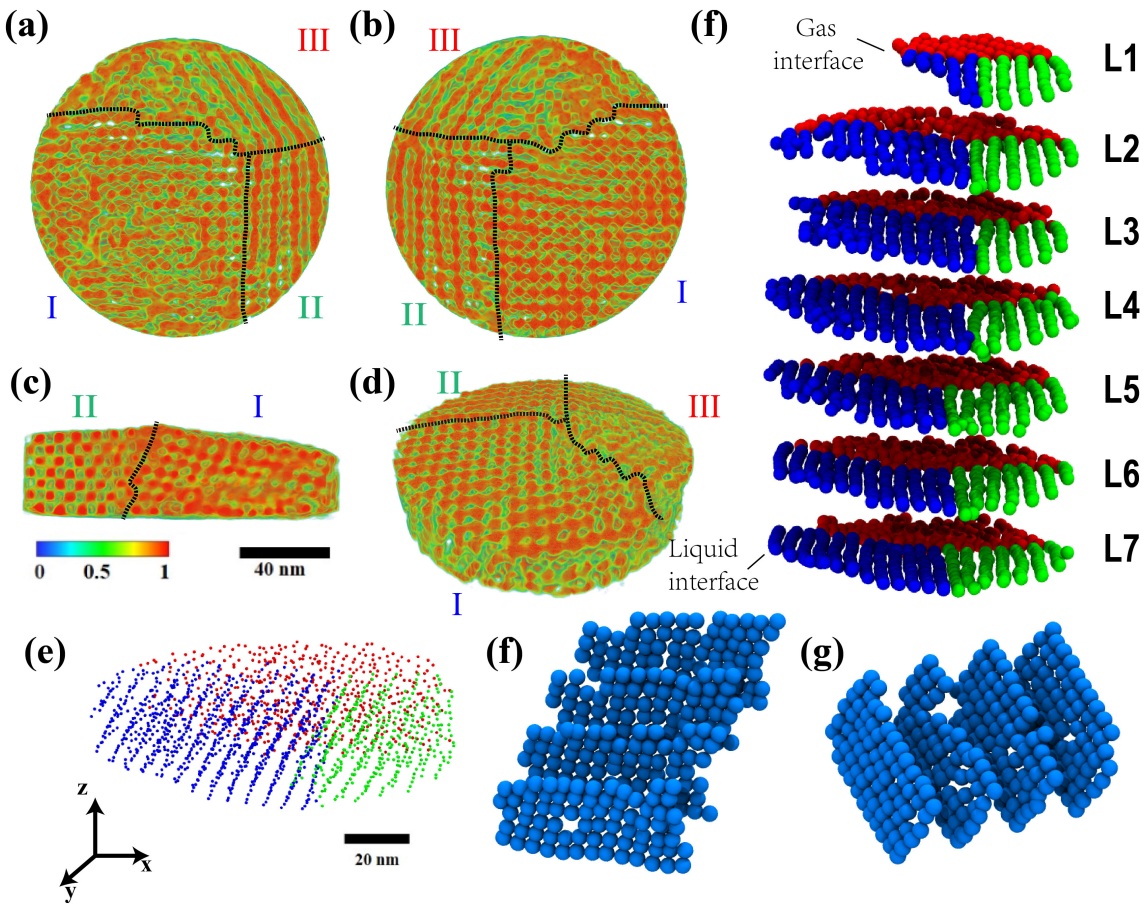

FIGURE 5.2. The epi-SL tomogram and QD positions. (a) Top, (b) bottom, (c) cross-section, and (d) perspective views of the tomogram of the epi-SL film. The color scale denotes the normalized electron density in units of e^-/nm^3. Dashed lines represent grain boundaries between the three SL grains (labeled grain I, II, and III). The scale bar is 40 nm. (e) Perspective image of the center of mass coordinates of all QDs in the sample. Each QD is represented by a sphere with a diameter of 1 nm (for ease of viewing). The QDs are color coded according to their location in grain I (blue), grain II (green), or grain III (red). The scale bar is 20 nm. (f) Exploded view of the seven QD layers of the sample to illustrate the internal structure of the epi-SL film. Each QD is represented by a 6 nm diameter sphere (Fig. S6). Layer 1 (L1) is the top layer of the originally floating film (at the QD/gas interface), while layer 7 (L7) is the bottom layer of the film (at the liquid/QD interface). The QDs are color coded according to panel e. (f-g) Representative monolayers in grain I seperated along direction x and y, representing SL lattice planes of (f)$(100)_{SL}$ and (g)$(010)_{SL}$.

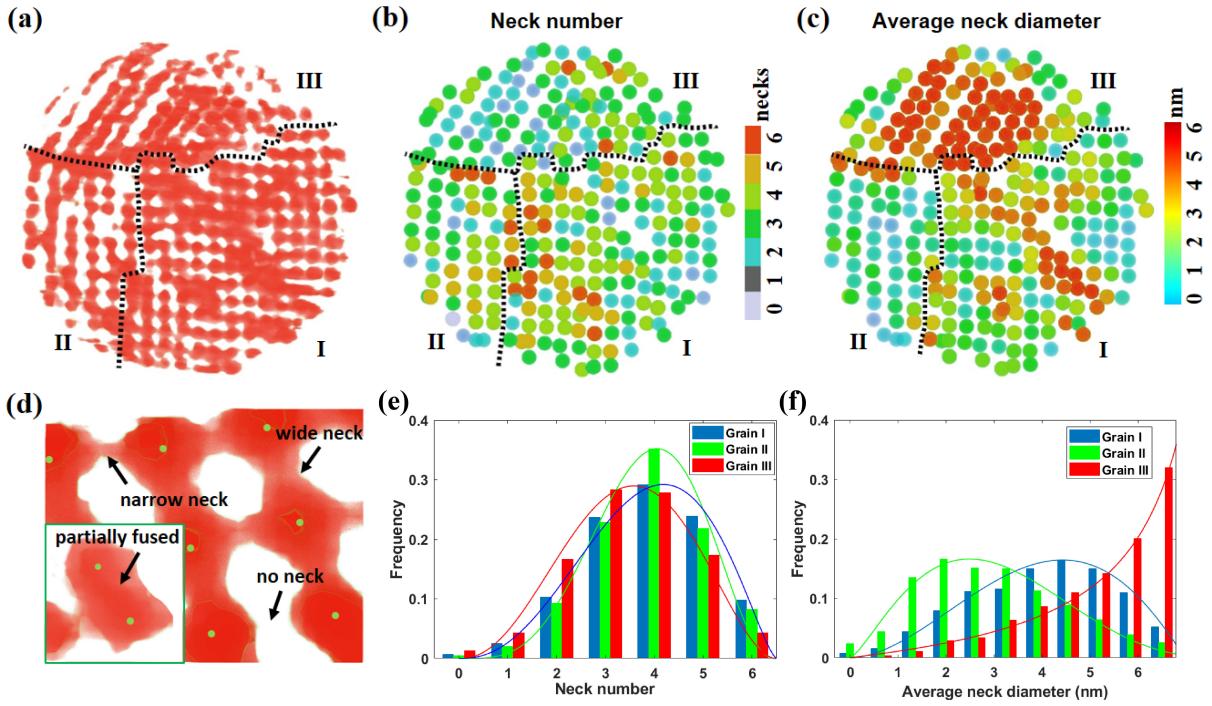

FIGURE 5.3. Analysis of the QD necks. (a) A slice of the tomogram through the middle of L4, showing in-plane necks between the QDs. (b) Heat map of the total number of necks for each QD in L4. The color scale is labeled. (c) Heat map of the average neck diamer for each QD in L4, including both in-plane and out-of-plane necks. The color scale is labeled. (d) Magnified isosurface views of two regions of the sample to illustrate typical neck polydispersity (narrow, wide, and missing necks) and a highly-fused pair of QDs (inset). The green dots denote the CoM of each QD. (e) Histograms of neck number for all QDs in grain I, II and III (inclusive of L1-7, not just L4). The solid curves are fitted beta distributions. (f) Corresponding histograms of average neck diameter. Fitting beta distributions are shown as solid curves. See Fig. S15 for histograms of the diameter of every neck in each grain.

TABLE 5.1. Lattice constants of SL grains I and II as determined from statistical analysis of the tomogram. GISAXS data is from refrence **31**.

Grain	a/nm	b/nm	c/nm	α	β	γ
I	6.4±0.6	6.4±0.6	5.9±0.7	102±8°	95±7°	96±7°
II	6.3±0.6	6.5±0.6	6.2±0.7	103±9°	107±5°	97±7°
GISAXS		6.6 ± 0.2			99 ± 2°	

5.2. Results and Discussion

5.2.1. SL Unit Cell and Disorder. Oleate-capped PbSe QDs with a diameter of 6.4 ± 0.3 nm were used to fabricate a 3D polycrystalline epi-SL film via self-assembly and ligand exchange

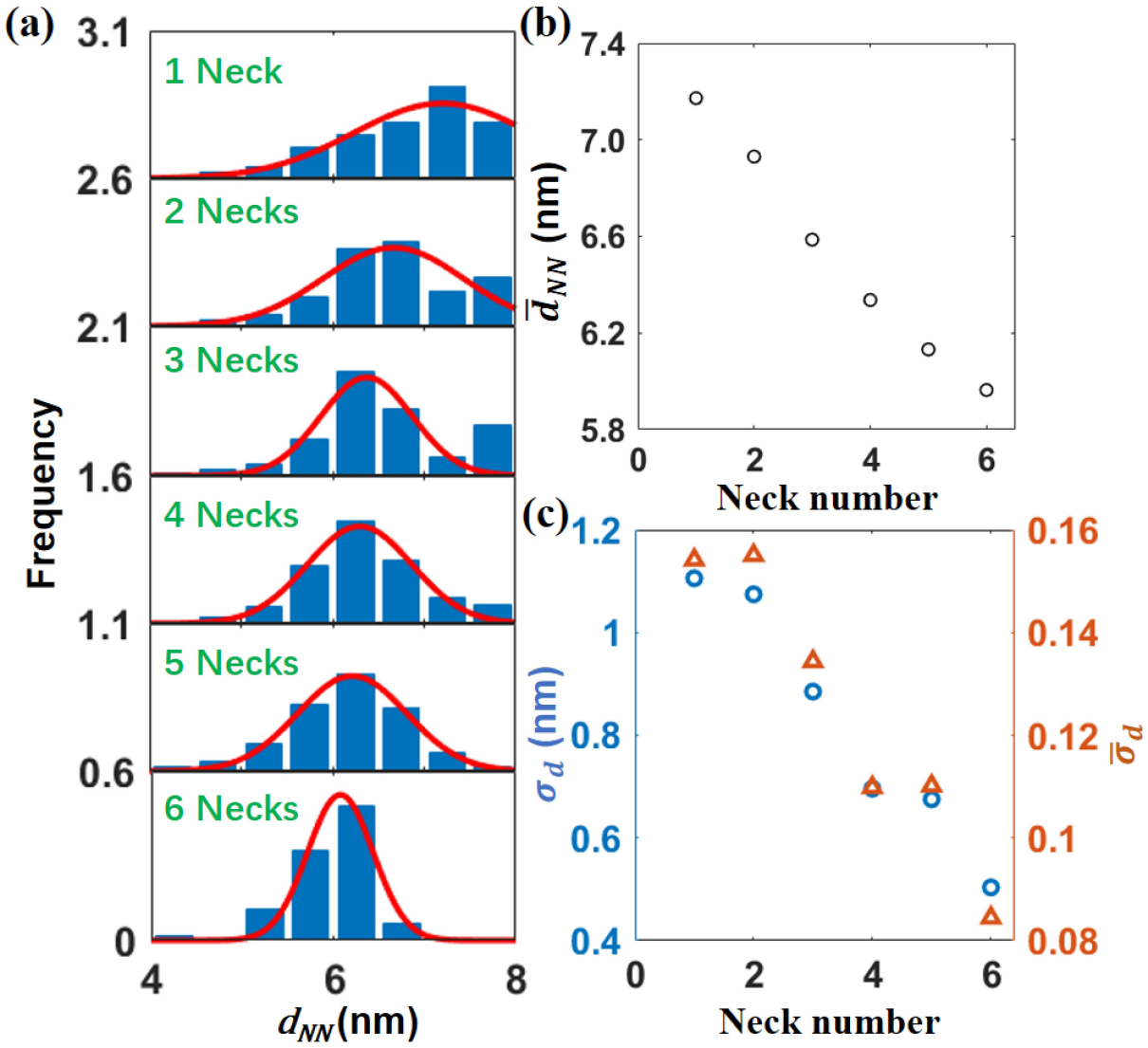

FIGURE 5.4. Correlation of neck number with nearest neighbor QD positional disorder. (a) Histograms of NN distance (d_{NN}) at each neck number for all of the QDs in grains I and II. Overlaid red curves are Gaussian fits. (b) Plot of the average NN distance ($\bar{d}_{\mathrm{NN}}$) versus neck number. (c) Plot of the standard deviation of the NN distance (σ_d) and the normalized standard deviation of the NN distance ($\bar{\sigma}_{\mathrm{d}} = \sigma_{\mathrm{d}}/\bar{d}_{\mathrm{NN}}$) versus neck number. $\bar{\sigma}_{\mathrm{d}}$ is a measure of the local disorder that is independent of differences in unit cell size.

on a liquid ethylene glycol substrate (Fig. 5.1a and Methods) [**125**,**126**,**148**,**149**]. After triggering epitaxial fusion of the QDs with EDA, the epi-SL film was stamped onto a silicon substrate, immersed in a solution of PbI_2 to remove additional oleate ligands, and milled by focused ion beam

(FIB) into a 128 nm diameter disc embedded in a nanoscale needle for full-tilt electron tomography studies (Fig. 5.1a). Scanning electron microscopy (SEM) images of the epi-SL film and the finished tomography needle are presented in Fig. 5.1b and 5.1c, respectively. An optical extinction spectrum of the QDs in solution and additional details about the preparation of the tomography sample are provided in the Supporting Information (Figs. S1-S2).

We acquired a $\pm 113^{\circ}$ single-axis tilt-series of 181 images of the sample using high-angle annular dark-field scanning transmission electron microscopy (HAADF-STEM) in a double aberration-corrected microscope (see Methods and Figs. S3-S4). Tomographic reconstruction of the sample was accomplished using the SIRT algorithm after careful image alignment and noise filtering. The final tomogram (Fig. 5.2a and Movie S1) has a spatial resolution of 6.5 Å ($\sim$1 unit cell of PbSe) as determined by the Fourier shell correlation (FSC) method (Fig. S5). This resolution is sufficient to unambiguously identify the center of mass (CoM) coordinates of all 1,846 QDs in the sample volume, as illustrated in Fig. 5.2e and f.

The CoM data were used to determine the size, shape, crystallographic orientation, and lattice parameters of the constituent SL grains as well as the presence of inter-grain defects (grain boundaries, amorphous domains, voids) and intra-grain defects. Visual inspection of Fig. 5.2 shows that the sample is seven QD layers thick and consists of three cylindrical sector-shaped (pie slice) SL grains that meet at a grain boundary triple junction near the center of the tomogram (dashed lines in Fig. 5.2a-d). While it is possible to assign the SL grain crystallography *a priori* from the CoM coordinates, we utilized the known unit cell of similarly-prepared PbSe QD epi-SLs [**4**] (distorted simple cubic with a = 6.6 $\pm$ 0.2 nm and $\alpha = 99 \pm 2^{\circ}$; Fig. S7) to help interpret the tomogram. Grain I has a square-like lattice of QDs in each QD layer parallel to the substrate, so it is assigned as a $(100)_{\mathrm{SL}}$-oriented SL grain, which is the most common grain orientation in this sample (see Fig. 1b). Grains II and III have 1D chains of QDs in each layer parallel to the substrate, with an average QD spacing of a along the chains and approximately $\sqrt{2}a$ between the chains. This arrangement is consistent with the $(01\bar{1})_{\mathrm{SL}}$ projection of the distorted simple cubic SL unit cell, so grains II and III are assigned as $(01\bar{1})_{\mathrm{SL}}$-oriented SL grains (again, see Fig. 5.1b). Grains II and III intersect at a planar coherent twin boundary indexed as 39°[001],(010) (most easily seen in Fig. 5.2a-b). Between grains I and II, it is harder to define a grain boundary inferface as we observe

in Fig. 5.2c a relatively smooth change in the $[001]_{SL}$ lattice vector from grain II on the left side to grain I on the right side. A possible mechanism for such an inter-grain orientational transition is proposed in Fig. S8 involving a small rotation and a subsequent glide of the $(100)_{SL}$ plane. Grains I and III meet at a highly-corrugated boundary. All three grain boundaries are normal or nearly normal to the substrate and span the entire thickness of the QD film. SEM images of similar grain boundaries are presented in Fig. S9. In Fig. 5.2g and h, we show representative separated layers in grain I along two other SL lattice vectors showing QD vacancies from different perspectives. The randomness in the QD positional order is shown to occur in all directions. We also note that there is no significant difference in the vacancy rate for layers normal to different lattice vectors. Several slice views of the tomogram taken at different angles are shown in Fig. S10 emphasizing the orientational differences between SL unit cells of grain I and II and also how the lateral and vertical monolayers are connected through necks. See Movies S2 and S3 for additional continuous slices of this sample.

We determined the lattice parameters of grains I and II by compiling nearest-neighbor QD distances and bond angles from the CoM data (see Fig. S11 for labeling conventions). Grain III was excluded from this analysis due to its poor spatial order. Histograms of the QD distances and angles (Figs. S12-S13) show Gaussian distributions with average and standard deviation values summarized in Table 1. The lattice constants of grains I and II are in good agreement with the unit cell parameters of similar epi-SL films derived from ensemble GISAXS measurements [**4**], so we conclude that these epi-SLs have essentially the same crystal structure, validating the recent GISAXS results. However, grains I and II also exhibit broad distributions of distances and angles indicative of a relatively large amount of positional disorder, as is apparent from Fig. 5.2. The spatial order of this sample is likely limited by the structural disorder of the original oleate-capped SL, the presence of several nearby grain boundaries, variability in QD neck number and diameter (*vide infra*), and (possibly) mechanical strain caused by sample preparation. Two additional aspects of the data are noteworthy. First, while grains I and II have very similar triclinic unit cells, they differ slightly in their β angle (Table 1). Such grain-to-grain variability is expected in polycrystalline SLs due to local differences in grain nucleation and growth, especially when the SL grains are small and experience non-uniform stress. Electron tomography is one of the few techniques capable

of detecting such minute structural differences between individual QD SL grains. Second, grain I is slightly compressed along the film normal with a smaller average lattice spacing in the c direction shown in Table 1. This is commonly seen for nanocrystal films prepared by solvent evaporation [**150**, **151**, **152**, **153**].

5.2.2. Characterization of Neck Disorder. In addition to the positions of the QDs, the tomogram provides rich information about the crystalline connections (necks) between the QDs. Previous TEM studies have shown that the QDs in these SLs are epitaxially fused across their {100} facets [**43**, **130**, **135**, **138**, **154**, **155**]. The epitaxial necks likely dictate the strength and uniformity of electronic coupling within the epi-SLs [**31**], so mapping the location and size of the necks is essential for understanding and optimizing the electronic properties of these materials. Electron tomography can directly visualize the necks and map the 3D neck network inside each SL grain. Fig. 5.3a shows a slice of the tomogram through the middle of L4 with the necks between the QDs clearly visible. We implemented an automated program to measure the cross-sectional area of every neck in the sample and assign each an effective diameter (Fig. S14). In our approach, any connection with an area smaller than the tomogram spatial resolution (0.43 nm^2, or about one PbSe unit cell) was considered to be absent (a "missing neck"). An example of a missing neck is shown in Fig. 5.3d.

Heat maps of the average neck diameter and the total number of necks for each QD in L4 are presented in Fig. 5.3b-c. Maps for all seven layers of the sample are compiled in Figs. S16 and S17. The 1,846 QDs in the sample have a maximum of 4,865 possible epitaxial necks (considering the six {100} facets of each QD and sample edge effects, vacancies, and voids). We observe a total of 3,471 necks, giving an overall network connectivity of 72%, well above the bond percolation threshold (p_c) of 25% for simple cubic lattices [**156**]. This estimate of neck connectivity is conservative because, as mentioned above, any neck smaller than the tomogram resolution ($\leq$3 Pb atoms wide) is not counted by our algorithm. Overall, the average number of necks per QD is 3.7 and the average neck diameter is 4.1 nm (64% of the QD diameter). Table 2 summarizes the neck statistics for the sample.

Figs. 5.3e and f show histograms of neck number and diameter for the three epi-SL grains in this sample. The neck number for all three grains follows a beta distribution (solid curves) with a

peak at 3.5-4 necks per QD. Grain I has the largest fraction of QDs with high connectivity (five and six necks), while grain II has the largest fraction of QDs with intermediate connectivity (four necks) and the smallest fraction of QDs with low connectivity (three or fewer necks). Overall, grains I and II are quite similar with respect to neck number. In contrast, grain III has much poorer neck connectivity than grains I and II, with the smallest fraction of high-connectivity QDs and the largest fraction of low-connectivity QDs. Grain III is also dominated by QDs with very large neck diameters (see the J-shaped distribution in Fig. 5.3f). The low neck number and large fraction of heavily-fused QDs contribute to the poor spatial order of grain III. The average neck diameters of grains I and II also follow a beta distribution and are similarly polydisperse. These two beta distributions (grain I: $\alpha = 2.90$, $\beta = 2.25$; grain II: $\alpha = 2.10$, $\beta = 3.18$) are approximately mirror images of each other (Fig. 5.3f). Grain I has a larger fraction of thicker necks (>4 nm) while grain II has a larger fraction of thinner necks (<4 nm). The reason for these differences in neck diameter and number in adjacent epi-SL grains is unclear, but probably related to variability in the spatial order of the parent oleate-capped SL and the kinetics of the epi-SL phase transition. We attempted to determine a correlation between neck number and diameter to measure whether the number of necks on each QD determined the neck thickness. Supporting Information Fig. S18a shows this correlation for the full sample and for each of the grains, indicating little correlation between the number of necks and the neck thickness for each QD, but also clearly showing that the average neck thickness is consistent throughout the grain regardless of the number of necks. Understanding the origin of such differences between grains will require systematic study of many tomograms to establish statistical relationships.

We also investigated whether there are trends in the necking that depend on the position of the layer within the SL. Fig. S18b-c plot the average neck number and diameter for each of the seven QD layers of the film. We find that the neck number is essentially constant in the middle five QD layers of grains I and II, while the neck number is significantly lower in grain III. However, there is a reduced neck number in L1 (the top of the film) for grains I-III and L7 (the bottom of the film) for grain II and III, despite taking into account edge effects. We conclude that the top and bottom monolayers of the epi-SL tend to have fewer necks per QD. For all three grains, the neck diameter is smaller in L1 and L7 and increases in the middle of the film (Fig. 5.4c). Interestingly,

TABLE 5.2. Neck statistics.

Parameter	Grain I	Grain II	Grain III	Total
number of QDs	903	389	554	1846
QD number density ($\times 10^{18}$ cm^{-3})	3.9	3.7	3.5	3.7(3.5*)
space filling fraction	0.53	0.51	0.48	0.51
possible necks	2343	1028	1494	4865
observed necks	1760	774	959	3493
connectivity	75%	75%	64%	72%
average number of necks	3.8	4.0	3.4	3.7
average neck diameter(nm)	4.0	3.5	5.0	4.1

* from reference 31.

while neck number and neck thickness are not in general correlated, the number and thickness of necks is lower at the QD/liquid and QD/gas interfaces, which suggests that out-of-plane forces from adjacent layers are important for necking formation and order. One might also expect to observe a monotonic decrease in neck number and diameter along the film normal due to ligand (glycoxide and oleate) concentration gradients since the ligands diffuse into the SL from the QD/liquid interface. Our neck diameter profile suggests that no such concentration gradients exist in this sample, in agreement with recent infrared spectroscopy measurements showing homogeneous ligand exchange in films of similar thickness [**4**].

We also explored the relationship between neck number and the local spatial order of the epi-SL. In the ideal averaged epi-SL unit cell (Fig. S7), each QD is necked to six nearest neighbors (NNs) located at a common center-to-center distance and fixed lattice angles. In contrast, QDs in real epi-SLs have distributions of neck number, NN distance, and lattice angles. These distributions provide a measure of the local (nanoscale) spatial disorder of the QD array. We reasoned that the distribution of NN distances and lattice angles should depend strongly on neck number because necks can form over only a narrow range of QD positions. Thus, QDs with high (low) connectivity should have more (less) ordered local environments. To assess the impact of neck number on local spatial order, we compiled histograms of the nearest neighbor distance (d_{NN}) as a function of neck number for all of the QDs in grains I and II (Fig. 5.4a). Grain III was again excluded from analysis due to its poor order. We find that as neck number increases, the average NN distance ($\bar{d}_{\mathrm{NN}}$) and standard deviation of the distance (σ_{d}) decrease in a linear fashion. As Fig. 5.4b and c shows,

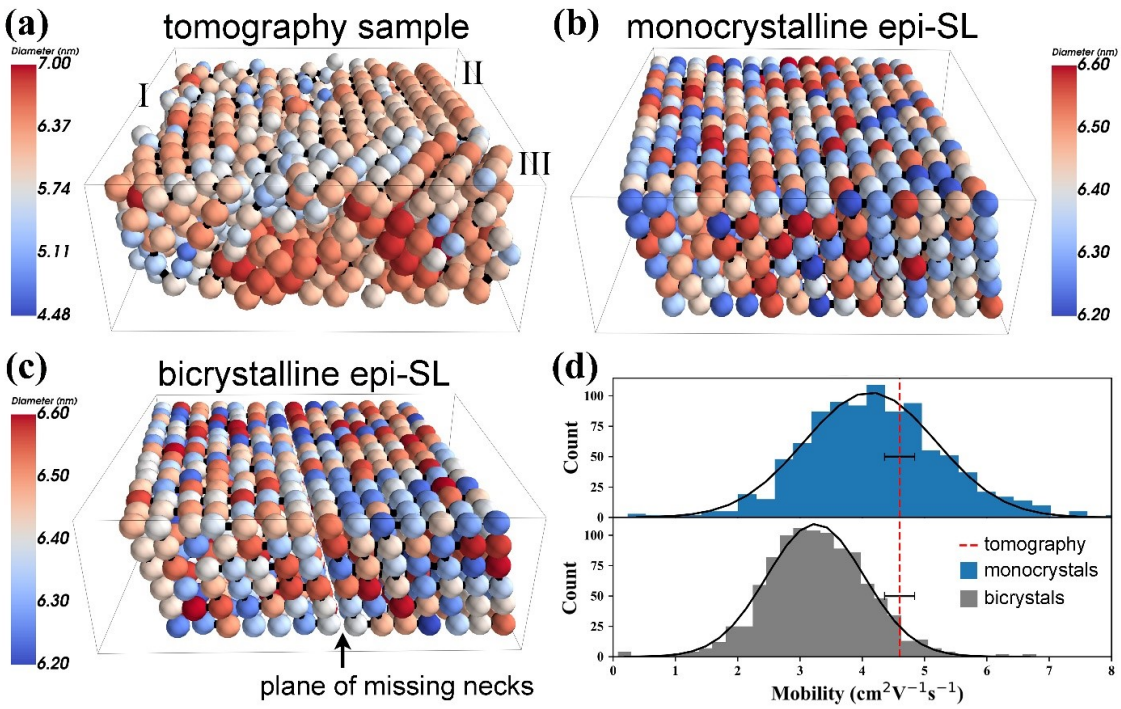

FIGURE 5.5. Transport simulation results. (a-c) Perspective views of the three types of simulated samples. (a) The tomography sample (trimmed from a disc into a cuboid). Grains I, II, and III are labeled. (b) A monocrystalline epi-SL. (c) A bicrystalline epi-SL. The monocrystalline and bicrystalline epi-SLs were generated using the lattice parameters, QD size distribution, QD positional disorder and neck statistics of grain I. The bicrystalline samples are bisected by a plane of missing necks (a necking grain boundary), which limits transport across this plane to hopping. Virtual electrical contacts are placed at the left and right sides of each sample. All simulation boxes are approximately 92×92×39 nm. (d) Comparison of the calculated electron mobility of the tomography sample (dashed red line), monocrystalline epi-SLs (blue bars) and bicrystalline epi-SLs (gray bars). The horizontal error bar represents the error in the mobility estimate for the tomography sample. Overlaid black curves are Gaussian fits of the histograms. The mobility for the monocrystalline and bicrystalline samples is 4.25 ± 1.25 cm^2/Vs and 3.28 ± 0.8 cm^2/Vs, respectively.

d_{NN} decreases from ~7.2 nm for QDs with one neck to ~6.0 nm for QDs with six necks, while σ_d decreases from 1.1 nm to 0.5 nm (a 55% reduction). Although this simple metric is limited to NNs and neglects the propagation of disorder across longer length scales [**43**], it demonstrates the importance of neck connectivity to the structural order of QD epi-SLs: high neck number is associated with high local spatial order. Future tomograms of more perfect monocrystalline samples

will be used to map, understand, and ultimately minimize the multiscale spatial disorder of these QD solids.

5.2.3. Charge Transport Simulation. Charge transport in the epi-SL tomography sample was simulated with the HINTS code. As described in the Methods section, the simulated tomography sample was generated using the QD CoM coordinates and neck network of the experimental tomogram and trimmed into a cuboid shape with electrodes on opposite faces (Fig. 5.5a). In this geometry, electrons must cross the grain boundary between grains I and II, or I and III, to traverse the sample. The tomogram shows that grains I, II, and III are connected by many necks across these grain boundaries. The mobility of the tomography sample was found to be $\sim$4.6 cm^2/Vs (Fig. 5.5d).

To probe the relative importance of the necking versus the conventional SL grain boundaries, and the disorder for the electron transport across the tomography sample, mobility simulations were also performed on the two ensembles of its monocrystalline and bicrystalline analogues. First, we compared the mobility of the tomography sample to that of the ensemble of monocrystalline (single-grain) epi-SLs with the same lattice parameters and neck statistics as grain I (Fig. 5.5b). Relative to the monocrystalline samples, the tomography sample has three grains separated by SL grain boundaries, but these grain boundaries are bridged by a large number of inter-QD necks. In spite of these differences, the mobility of the tomography sample remains typical of the mobility distribution of the ensemble of monocrystalline epi-SLs, as shown in the upper panel of Fig. 5.5d. Next, we also calculated the carrier mobilities of the ensemble of bicrystalline (double-grain) epi-SLs, generated by removing a bisecting plane of necks from the monocrystalline samples (Fig. 5.5c). Electrons can move across this "necking grain boundary" only by hopping, which is significantly slower than direct tunneling through necks. We find that the computed average mobility decreases by $\sim$25% as a consequence of splitting the neck network in two (lower panel of Fig. 5.5d). The introduction of the necking grain boundary makes the mobility of the tomography sample largely inconsistent with the bicrystalline mobility distribution.

The most natural explanation of these results is that the mobility in these strongly disordered epi-SLs is primarily determined by transport across the inter-QD neck network, while SL grain

boundaries impact the mobility only to a limited degree as long as inter-QD necks continue to connect the SL grains across the SL grain boundary with a reasonable density. The tomography sample falls into this category: this explains why its mobity is consistent with the mobility distribution of the monocrystalline samples. In contrast, when a sample is bisected with a neck grain boundary, so that the two grains cease to be connected by inter-QD necks, electrons are forced to thermally hop across no-neck boundaries rather than tunnel through necks, thereby reducing the mobility by a substantial amount. Our analysis suggests that the formation of necks between QDs across conventional SL grain boundaries is an efficient way to substantially increase carrier transport across those grain boundaries. Strategies to enhance the mobility in SLs were already discussed in earlier works, wherein the importance of reducing the disorder of SLs to form mini-bands was emphasized [**44**]. A key message of the present paper is that the mobility of QD SLs can also be substantially improved by forming sample-spanning neck networks. In a single-grain sample, charge transport should be improved by regulating intra-grain necking conditions such as decreasing neck size dispersity and increasing connectivity. This is particularly true for QD SL based photovoltaics, where the charge carriers are collected along the through-plane (film normal) direction of the multilayer instead of in-plane direction. We did observe a higher through-plane connectivity of QDs in Grain I that might suggest anisotropic necking conditions in a 3D epi-SL film. However, further investigations should be conducted to look into the effect of the degree of anisotropy of connectivity on the mobility, and will more rely on structural statistics from single-grain tomography samples, which is beyond the scope of this paper.

5.3. Conclusion

We analyzed a full-tilt electron tomographic reconstruction of a disc-shaped region of a 3D epitaxially-connected PbSe QD SL film. This tomogram provides (i) sufficiently high spatial resolution (0.65 nm) to accurately determine the position and size/shape of the QDs and their necks and (ii) sufficiently large volume (4.3×10^5 nm^3) to enable meaningful statistical analysis of structural disorder in the sample. We showed that the sample consists of three SL grains and assigned the unit cell and in-plane crystallographic orientation of each grain as well as the structure of the three grain boundaries. Maps of the neck locations and diameters revealed that the sample has an

average of 3.7 necks per QD (overall network connectivity of 72%) and an average neck diameter of 4.1 nm (64% of the QD diameter). In testing correlations between neck number, neck diameter, inter-QD distance, and QD location in the film, we discovered a strong association between neck number and both the average and standard deviation of the nearest neighbor QD distance, demonstrating that QDs with more necks tend to have more ordered local environments. Achieving more complete, uniform necking will require fabrication of more perfect oleate-capped SLs and greater control of the kinetics of the phase transition from the oleate-capped SL to the epi-SL.

We also simulated the combined nearest-neighbor hopping/tunneling transport in this SL film. Simulations of monocrystalline and bicrystalline analogues showed that SL grain boundaries have limited impact on the electron mobility as long as the grains remain interconnected by necked QDs that form percolating neck networks. An encouraging message of this result is that high mobilities can still be achieved in QD SLs even if they have a high density of grain boundaries, and thus small grain sizes, by increasing the QD attachment density, or neck connectivity, across the SL grain boundaries. To complete the picture, it is natural to expect that once the neck networks connect most of the QDs of the epi-SL to the point that carriers delocalize into mini-bands, further mobility enhancements can be achieved by reducing the density of conventional SL grain boundaries as well.

Our study sets a baseline for the quantitative structural characterization of 3D QD epi-SLs. Looking forward, electron tomography will likely be an important tool for elucidating processing/structure/property relationships and guiding the fabrication of increasingly perfect 3D epi-SLs. Higher-quality epi-SLs will in turn encourage more in-depth analysis of the tomograms, particularly with regard to disorder across length scales longer than those emphasized in this paper [**43**]. Finally, we note that improving the tomogram resolution by a factor of two would allow visualization of QD facets and atomic-scale defects such as edge dislocations [**157**], thereby providing a comprehensive near-atomistic picture of the 3D structure of these mesoscale QD films.

CHAPTER 6

Hierarchical carrier transport simulator for defected nanoparticle solids

This work appeared as Scientific Reports 11, 7458 (2021).

As described in previous chapters, various experimental groups have managed to boost the mobility in NP solids by enhancing the inter-NP transition rate with a variety of methods, including: ligand engineering [**34**,**35**,**36**], band-alignment engineering [**37**,**38**], chemical-doping [**39**,**40**], photo-doping [**41**], metal-NP substitution [**42**], epitaxial attachment of NPs [**33**, **43**], and atomic layer deposition methods [**44**]. Encouragingly, these efforts recently translated into notable progress, as NP solids were reported to exhibit band-like, temperature-insensitive mobilities, with values exceeding 10 cm^2/Vs at room temperatures [**40**,**45**]. It is important to note that some experiments reported data that can be interpreted as evidence for band-like transport. One of these is the relative temperature independence of the observed mobilities, in contrast to hopping insulators where an activated temperature dependence is expected. However, the absolute values of the mobilities remain relatively low compared to most metals, and this makes conservative commentators stop short of identifying this transport as metallic [**40**, **45**].

On the theoretical front, there have been efforts from several groups to understand electronic transport in NP films and solids. Density functional theory (DFT)-based ab initio calculations of the energy levels of a single NP alone are already limited to only hundreds of atoms for higher-reliability methods, and a few thousands for more approximate methods by prohibitive CPU times. These translate to diameters less than 2-3 nm, whereas experimental NP diameters often exceed 5-6 nm. Next, the accurate computation of the NP-NP transition rates would require the simulation of two NPs. And even if this calculation is completed, it does not address that the NP-NP transport is not metallic but insulating; the disorder of the parameters from NP to NP; and finally the defects of the NP solids. In total, ab initio descriptions alone are very far from being capable

of describing transport in NP solids. Cleary, there is a pressing need for developing mesoscopic transport simulations that somehow integrate ab initio calculations.

Shklovskii et al. have developed transport calculations for a NP array in a FET geometry, where they focused on the effects of the Coulomb interaction [**47**]. The interplay of transport and Coulomb interactions was studied in Refs. **47** and **48**, albeit on very small samples. Over the last few years, our group developed the Hierarchical Nanoparticle Transport Simulator (HINTS) platform that starts with an ab initio calculation of the energetics of individual nanoparticles, then forms a NP solid of several hundred NPs, and finally simulates transport across this NP solid by a kinetic Monte Carlo method [**49**, **50**], described in Chapter 2. HINTS can simulate 500-2,000 nanoparticles. A reassuring validation of HINTS emerged from simulating the dependence of the mobility of PbSe NP layers as a function of the NP diameter. The results in [**49**,**50**] closely tracked the experimental results of Liu et al., who studied the electron mobility of PbSe layers in a FET geometry [**31**]. More recently, we studied commensuration effects in bilayer NP solids [**51**].

However, these theoretical efforts only considered NP solids with homogeneous disorder: the NPs were arranged either in a close-packed glassy/jammed structure, or on an ordered superlattice (SL) with disorder only in the NP size. In contrast, representative scanning electron microscope (SEM) images, like in Fig. 6.1, taken of NP solids with millions of NPs, conspicuously reveal that typical NP solids are also characterized by disorder on much larger length scales. These defects, often on the μm length scale, have sizes well beyond the capabilities of any published technique, including HINTS. Therefore, there is a need for transport simulation methods that are capable of capturing meso- and macro-scale defects and their effect on transport.

We performed one step in this direction previously by extending our HINTS method to include percolative effects into homogeneously disordered NP solids [**50**]. This simulation captured physics on the longer length scales of percolative clusters. Our main message was that a metal-insulator transition (MIT) occurs when a percolating path of metallic-connected NPs develops across the entire sample. We described this MIT as a Quantum Percolation Transition. However, this work still did not incorporate planar defects.

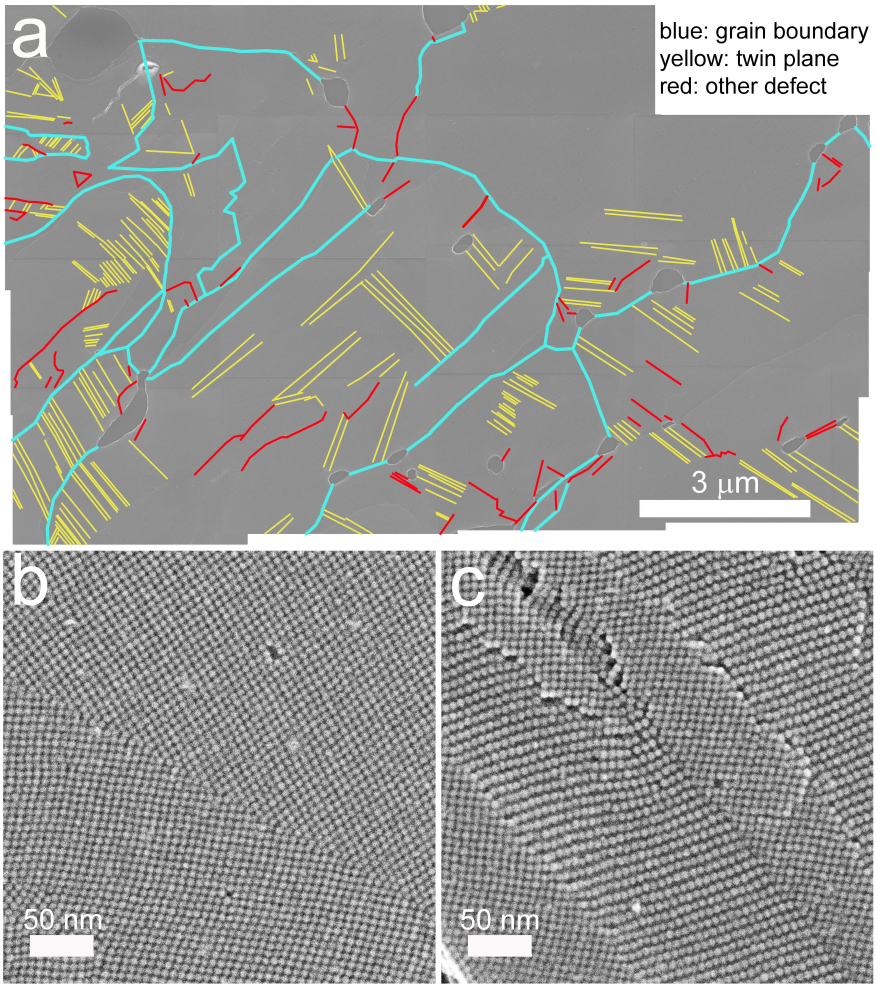

FIGURE 6.1. Common planar defects in PbSe nanoparticle superlattices. (a) Grain map of a typical region of an PbSe NP superlattice film showing the location of several types of planar defects. Blue, yellow, and red lines denote wide-angle grain boundaries, twin planes, and more complex, unclassified planar defects and defect clusters, respectively. The image is a montage of fifteen low-magnification, high-resolution SEM images. Voids, step edges, vacancies, and other types of non-planar defects are also visible in the montage. (b) Higher-magnification secondary electron image of a bicrystalline region of an epi-SL film with two (100)SL-oriented SL grains meeting at a twin plane. (c) Image of another region of the same epi-SL film showing multiple grain boundaries between (100)SL- and (0$\bar{1}$1)SL-oriented grains, as well as several other planar defects.

6.1. Simulation Methods

To answer the above needs, in this paper we report our work that boosted the capability of our HINTS platform by introducing additional hierarchical layers to capture the effect of planar defects

on the transport in NP solids. First, we used HINTS to individually model a NP superlattice (SL) with one planar defect that was either a generic grain boundary or a twin plane. Second, we simulated transport across a large number of such single-defect SLs, and determined the distribution of the mobilities of the single-grain-boundary NP SLs and that of the single twin-plane NP SLs. We also determined the distribution of the mobilities of undefected NP SLs with only homogeneous NP disorder. Third, to reach a simulation scale approaching the scale of the NP solids in the experiments, we built a resistor network where the individual resistor values were taken from the three mobility distributions with predetermined probabilities. Motivated by our previous work [**50**], we determined the resistance of the entire resistor network by changing the fraction of undefected NP SLs within the network. Finally, we analyzed our results by a finite size scaling method.

We call this boosted HINTS platform TRIDENS: the **TR**ansport **I**n **DE**fected **N**anoparticle **S**olid Simulator. With TRIDENS, we are capable of capturing the physics from atomistic length scales up to the scale of NP solids in the experiments by integrating the simulations on several hierarchical layers. The complete hierarchical structure of TRIDENS, beyond the underlying HINTS platform, is presented below. The focus of this work was PbSe NPs because they are of considerable interest for solar applications due to their large Bohr exciton radius and small direct bulk bandgap [**158**], and exhibit the possibly game-changing multiple-exciton generation (MEG) [**21**]. For these reasons, PbSe NPs are often thought to have strong promise for solar applications.

(1) To reach the length scale of hundreds of nanometers, we generated triclinic NP superlattices, of PbSe NPs with a 20x20x2 geometry, inspired by the 2D channel geometries of FETs used in transport experiments [**4**]. The triclinic unit cell was described with lattice constants $a_1 = a_2 = a_3$ = 6.9 nm and angles $\alpha = \beta = \gamma = 99°$. The average NP diameter was 6.0 nm. Size and location disorder were introduced by assigning the NPs a diameter and lattice displacement vector according to Gaussian distributions of widths $\sigma(diameter) = 0.4$ nm and $\sigma(location) = 0.3$ nm respectively. See Fig. 6.2a for an example of one of these SLs. In our undefected SLs, these parameters yield a $\langle \beta_{ij} \rangle \simeq 0.015 \pm .02$.

Layers (1) is still part of the main HINTS platform. HINTS is suitable for capturing the effects of homogeneous disorder, i.e. disorder associated with the size and location of the NPs that varies from site to site of the NP superlattice, but does not involve planar defects. Next, we describe the

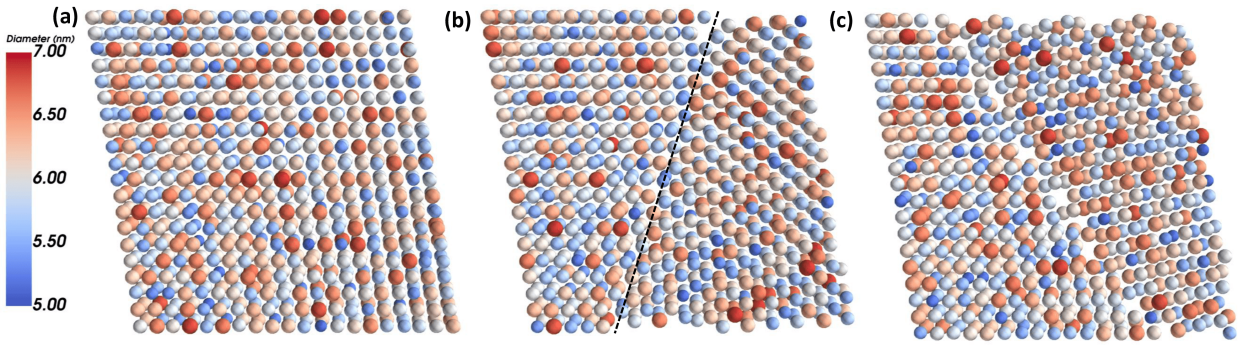

FIGURE 6.2. Top down views of the three types of the simulated NP SLs: (a) An undefected NP SL, characterized by the NPs having only size and location disorder; (b) A NP SL, containing a twin plane, as denoted by the dashed line, also with NP size and location disorder; and (c) An NP SL, containing a grain boundary, also with NP size and location disorder. NP color corresponds to NP diameter, as indicated in the colorbar on the left.

additional layers of the TRIDENS that enable us to access length scales well beyond the reach of HINTS.

(2) As a first step, we introduced a single planar defect into each generated NP superlattice (SL). We carefully analyzed SEM images of NP solids with millions of NPs of the type of Fig.6.1, and determined the predominant types of defects and their statistics, such as the lengths and densities of the planar defects. Based on the SEM image analysis, the most relevant and oft-occurring planar defects were twin planes and grain boundaries.

(a) Twin planes: the NP superlattice is mirrored across a boundary plane, creating two crystallites, or grains, which have reflected in-plane unit cells. Twinned grains can also be related by a 180° rotation normal to the twin plane. The twin plane is always parallel to a possible crystal face (but not any planes of complete symmetry, e.g. it is distinct from all space group symmetries), and thus requires the two grains to share some NP lattice sites along the boundary plane. See Fig. 6.1b and Fig. 6.2b. The high symmetry nature of twin planes makes them a low disorder defect, compared to the more highly disordered grain boundaries discussed below. In our generated samples the twin planes were created in a (100) in-plane oriented SL, and the orientation of the twin plane itself was randomly selected on a sample-by-sample basis from all possible crystal planes which would span the entire NP simulation SL in the x-direction (in order to bisect the SL). As an example, one such boundary orientation is that of a $(01\bar{2})/(02\bar{1})$ twin boundary, where $(01\bar{2})$ is the

orientiation of the boundary plane in grain 1, and $(02\bar{1})$ is the orientiation of the boundary plane in the mirrored grain 2.

(b) Grain boundaries: the NP superlattice is again fractured by a boundary plane. However, unlike with twin planes, the superlattice is not mirrored across the boundary plane. There are two main types of grain boundaries. 1) Tilt grain boundaries, where the in-plane SL orientation is the same in the two grains, but they are spatially rotated in-plane relative to each other. The angle of rotation can be divided into "low angle" and "high angle" regimes, where the higher the angle of rotation, the more disordered the grain boundary (with large areas of poor fit). 2) Twist grain boundaries, where the in-plane superlattice orientations of the two grains are different (rotation occurs along an axis perpendicular to the boundary plane). Such grain boundaries will result in two crystallites/grains with different in-plane superlattice orientations (e.g. a boundary between a $(100)_{\mathrm{SL}}$ in-plane orientation and a $(101)_{\mathrm{SL}}$ in-plane orientation).

In our generated samples, we simulated grain boundaries with a combination of tilt and twist mismatching. Specifically, the boundary plane separated grains of $(100)_{\mathrm{SL}}$ in-plane orientation and $(01\bar{1})_{\mathrm{SL}}$ in-plane orientation respectively, with the relative in-plane spatial orientation of the two grains depending on the angle of the boundary plane (chosen at random on a sample-by-sample basis). The boundary plane was always limited to angles which would span the entire NP simulation SL in the x-direction (in order to bisect the SL). This results in grain boundaries which are much more extensively disordered than twin planes, particularly when the boundary plane results in a high-tilt grain boundary. See Fig. 6.1c and Fig. 6.2c. Hereafter, we will refer to our specific combination of boundary mismatching as simply a "grain boundary".

In total, we generated 30,000 NP superlattices, containing either one or two grains, where we varied the disorder of the NP diameters (see color code in Fig. 6.2), the on-site NP location disorder, and the orientation of the planar defects as viewed out-of-plane. Of these 30,000 NP SLs, 10,000 NP SLs had no planar defects, the next 10,000 NP SLs contained one twin plane, and the last 10,000 NP SLs contained a grain boundary.

Fig. 6.1 shows other types of defects as well. We determined that point vacancies have minimal effect on the mobilities in the insulating phase. One can also see tears/rips/voids/cracks in the SEM image. NP superlattice fabrication technologies will be ready for technical application when

they can minimize or eliminate such disruptive tears. For these reasons, we did not model either of these defects.

(3) Next, we determined the electron mobility across each of the 3x10,000 defected NP SLs. To do this, each NP SL was populated with electrons, randomly placing them on NPs, using the Mersenne Twister, until a predetermined electron density was reached. The chance of an electron being placed on any particular NP was uniform, independent of electron occupation and NP parameters. Data was only taken well after the system achieved equilibrium. A small voltage was applied across the sample to induce transport in the linear I-V regime, with periodic boundary conditions. Finally, the electron transport was simulated by evolving time via a kinetic Monte Carlo (KMC) algorithm. The so-determined mobilities of the 3x10,000 NP SLs were used to create the mobility distributions for the homogeneously disordered NP SLs, the twin-plane-supporting NP SLs, and the grain-boundary-supporting NP SLs. The first class of NP SLs will also be referred to as "undefected NP SLs", the latter two classes as "defected NP SLs".

(4) To simulate NP solids on mesoscopic length scales of the order of 10 μm or longer, we generated a classical resistor network, with resistors chosen at random from the distributions determined in step 6. Which distribution the resistors were chosen from was also randomly determined, according to a parameter that describes the fraction of defected resistors. Random numbers were generated using standard numpy libraries. Each resistor represents an NP SL with an $L = 20$ length planar defect. One notes that in Fig.6.1 many of the planar defects are considerably longer than $L = 20$. Representing planar defects with longer lengths is possible in TRIDENS by placing defected NP SLs correlated along the lines of the network. Such longer range defect-correlations were not pursued in the present work, but will be included in future work.

With these preparations, the mobility of the overall NP solid was determined by treating this NP SL network as a resistor network. We used the Laplacian method of F. Y. Wu et al. to calculate the overall resistance across the entire network [**159**]. The electrodes were modeled as equipotential metallic strips spanning the entire length of the sample edge, thus making them equivalent to a single node on a resistor network. These electrodes were coupled to the sample by contact resistors that were chosen according to the same rules as the bulk resistors.

(5) Having determined the overall mobility of the network of defected NP SLs, we adapted finite size scaling methods to analyze whether this resistor network model built from defected NP SLs had a phase transition, or a crossover, and if so, what are the properties of this transition. To this end, we repeated step (4) for resistor networks of various sizes, including 32x32, 64x64, and 128x128. As detailed below, our finite size scaling found a percolation transition that separates a low mobility insulator from a high mobility insulator. We used finite size scaling to determine the critical properties of this transition, including the critical point, the critical exponents and the universal scaling function.

6.2. Experimental Methods

6.2.1. Materials: Lead oxide (PbO, 99.999%), oleic acid (OA, technical grade, 90%), diphenylphosphine (DPP, 98%), 1-octadecene (ODE, 90%), ethylene glycol (EG, 99.8%, anhydrous), acetonitrile (99.99%, anhydrous), hexanes (≥99%, anhydrous), toluene (99.8%, anhydrous), and (3 - mercaptopropyl) trimethoxysilane (3-MPTMS, 95%) were purchased from Sigma Aldrich and used as received. Trioctylphosphine (TOP, technical grade, >90%) and selenium (99.99%) were acquired from Fluka and mixed for 24 hours to form a 1 M TOP-Se stock solution. Ethylenediamine (EDA, >98.0%, anhydrous) was purchased from TCI and mixed with acetonitrile in a 1:1 volume ratio to make a 7.5 M EDA stock solution, this is a slight modification to a published procedure [**4**].

6.2.2. Quantum Dot Synthesis: In this experimental section we adopt the alternative terminology of "quantum dots" to refer to the nanoparticles, to accommodate alternative terminologies preferred by different communities. PbSe QDs were synthesized and purified air-free using a slight modification of a published procedure [**4**]. Briefly, PbO (1.50 g), OA (5.00 g), and ODE (10.00 g) were mixed and degassed in a three-neck round-bottom flask at room temperature. The mixture was heated to 120 C under vacuum to form dissolved Pb(OA)2 and dry the solution. After 1 hour at 120 C, the Pb(OA)2 solution was heated to 180 C under argon flow and 9.5 mL of a 1 M solution of TOP-Se containing 200 μL of DPP was rapidly injected into this hot solution. An immediate darkening of the solution was observed, and the QDs were grown for 105 seconds at ∼160 C. The reaction was quenched with a liquid nitrogen bath and injection of 10 mL of anhydrous hexanes. QD purification and SL fabrication were performed in glove boxes with <0.5 ppm O2 content. The

QDs were purified by two rounds of precipitation/redispersion using acetonitrile/toluene and stored as a powder in the glove box.

6.2.3. Substrate preparation: Following and slightly modifying the procedure seen in Ref. **4**, a single-side polished Si substrate was cleaned using 10 minutes of sonication in acetone, Millipore water, and then isopropanol, followed by drying in a stream of flowing air. The cleaned substrate was immersed in a 100 mM solution of 3-MTPMS in toluene for 1 hour to functionalize its native SiOx surface for improved QD film adhesion, then rinsed with neat toluene and dried in flowing air.

6.2.4. Superlattice fabrication, electron microscopy imaging: Quantum dot superlattice films were fabricated and imaged using (modified) published procedures [**4**]. An oleate-capped superlattice was prepared in a glovebox (<2 ppm O2) by drop casting 60 μL of 20 g/L dispersion of PbSe QDs in hexanes onto 7 mL of ethylene glycol (EG) in a Teflon well (3.5 x 5 x 1 cm). After depositing the QD solution, the well was immediately covered with a glass lid. The hexane evaporated over 30 minutes, resulting in a smooth, dry QD film floating on the EG surface. The glass lid was then removed and 0.1 mL of a 7.5 M solution of EDA in acetonitrile was slowly injected (5-10 sec) into the EG under the QD film using a 1 mL syringe. After 30 seconds of exposure to EDA, the resulting epi-SL film was stamp transferred to the Si substrate using a vacuum wand, rinsed vigorously with acetonitrile, and dried under flowing N2.

Scanning electron microscopy (SEM) imaging was performed on an FEI Magellan 400 XHR SEM operating at 10 kV. Grain maps were produced by stitching together fifteen 6,144 x 4,415 pixel images acquired at 50,000x magnification, providing the ability to resolve individual QDs in the sample. Image stitching was performed in Adobe Photoshop. Grain boundaries, twin planes, and other planar defects were then located by eye and drawn in manually.

Superlattice samples for TEM analysis were prepared by stamping QD films from the EG surface onto holey carbon TEM grids without a carbon film coating. The use of TEM grids free of a carbon film was critical for high-quality secondary electron imaging (SEI) in the TEM. SE imaging was performed on a JEOL JEM-2800 TEM operating at 200 kV using a probe size of 1.0 nm.

6.3. Results and Discussion

6.3.1. TRIDENS simulations: We laid the foundation of our simulation by carrying out the standard HINTS study steps, including step (1) above. To carry out step (2), we generated 3x10,000 defected NP SLs by starting with homogeneously disordered but undefected 20x20x2 NP SLs whose shape broadly corresponded to FET geometries, and then inserted a twin plane planar defect into 10,000 NP SLs, and a grain boundary planar defect into another 10,000 NP SLs. The latter sometimes involved removing a few NPs to keep the shape of the NP SLs largely unchanged.

Next, we executed step (3) by determining the mobility distribution of the defected NP SLs. The mobility distribution for the homogeneously-disordered, undefected NP SLs is shown in Fig.6.3a. The mobility distribution of the twin-plane NP SLs is shown in Fig.6.3b. Finally, the mobility distribution of the grain-boundary NP SLs is shown in Fig.6.3c. All three distributions were approximately normal, and could be well characterized by a mean and a standard deviation. The mobility of the undefected NP SLs was 0.42 ± 0.1 cm^2/Vs, the mobility of the NP SLs containing twin planes was 0.16 ± 0.06 cm^2/Vs, and the mobility of the NP SLs containing grain boundaries was 0.09 ± 0.05 cm^2/Vs, as shown.

We then performed step (4) by assembling a resistive network whose individual links had mobilities selected from the above determined mobility distributions. To identify the paradigmatic aspects of the behavior of the mobility of the NP solid, we selected the links from the highest mobility undefected NP SL distribution with a probability p, and from the lowest mobility grain boundary NP SL distribution with a probability $(1 - p)$. We used this p, the fraction of the high mobility undefected NP SLs/links as the control parameter of our study. Initially we expected that when the probability $(1-p)$ of the low mobility defected NP SLs becomes small, then the electrons will be able to "flow around" the low mobility links through the high mobility links. Put differently, the high mobility links will be able to approximately short out the low mobility links. Had this expectation been true, then the mobility of the NP solid should have exhibited a saturation as p approached 1.

Fig.6.4 shows the evolution of the mobility of NP solids with p. Visibly, our initial expectation was not confirmed as the mobility did not show a saturation as the fraction p of the undefected NP SLs approached 1.0. The high mobility links did not "short out" the low mobility links. A possible

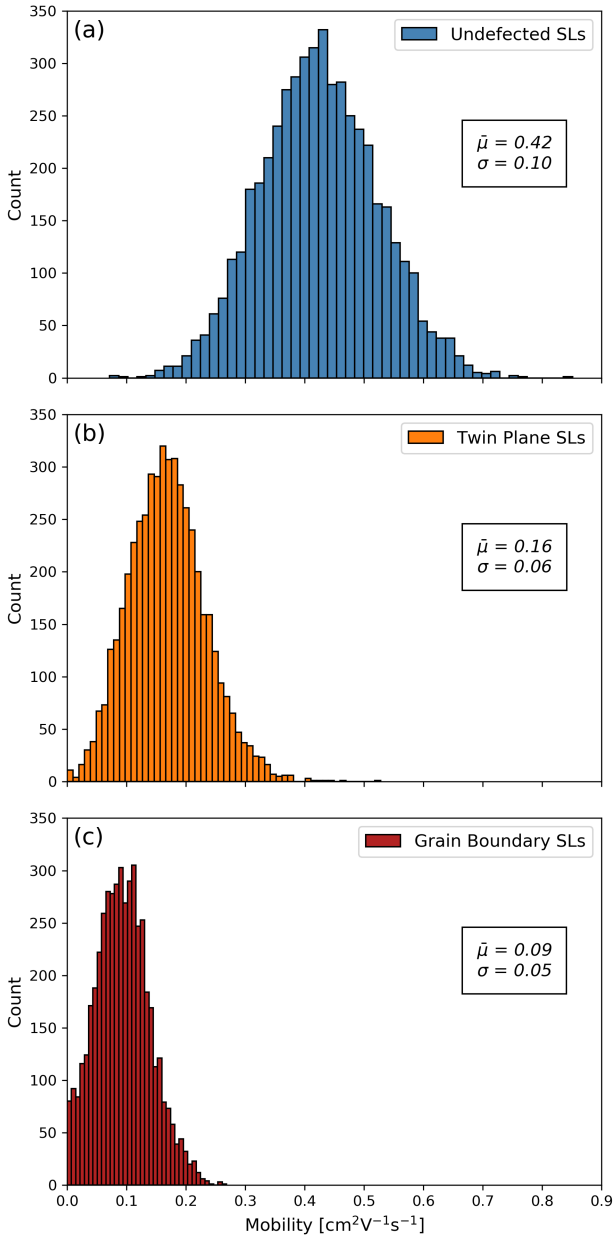

FIGURE 6.3. Mobility distributions of the 3 types of NP SLs: (a) Undefected NP SLs, the NPs having size and location disorder; (b) NP SLs, each containing a twin plane, also with NP size and location disorder; (c) NP SLs, each containing a grain boundary, also with NP size and location disorder. Displayed in each panel is the average mobility and standard deviation of Gaussians fitted to the distributions. All simulations were performed at a temperature of $T = 300K$.

explanation is that the mobilities of the different NP SLs were not different enough for such a short-out. We checked the robustness of this result, and found the same characteristic non-saturating shape in other 2D geometries, as well as in 3D bulk networks.

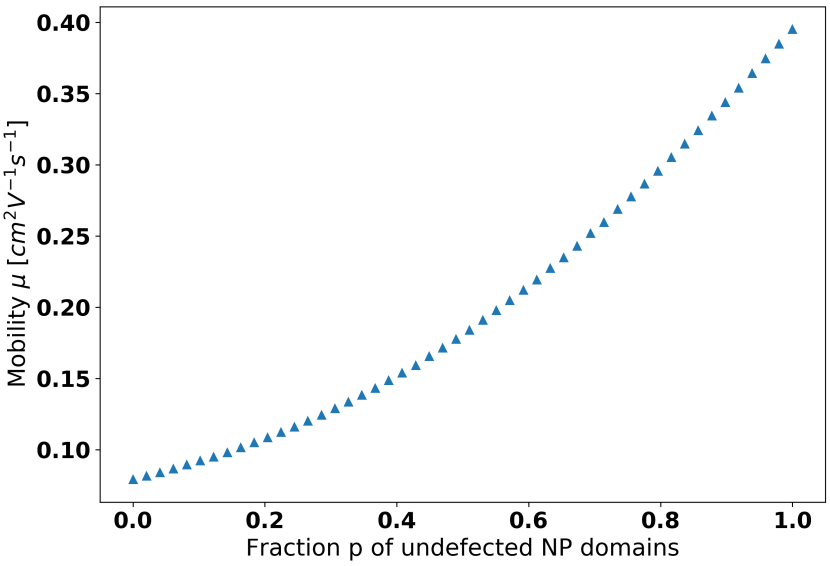

FIGURE 6.4. Mobility of a 32x32 resistor network whose resistors/links are chosen from two distributions, the low mobility grain boundary NP SLs mobility distribution and the high mobility undefected NP SLs mobility distribution. The fraction p of the high mobility NP SLs sweeps the 0 to 1 region. The error bars are smaller than the data points.

6.3.2. Bimodal percolation transition: Next, we investigated whether there is a percolative critical behavior as the p fraction of high mobility links is varied. The simple case of a resistor network, where the links either have a finite (electronic) mobility μ with probability p, or a non-conductive zero mobility with probability $(1-p)$, has been extensively analyzed. The conductivity of such a resistor network exhibits a critical behavior across the percolation critical point p_c with a power law dependence $\mu \propto (p-p_c)^t$, where the critical exponent $t > 1$ is universal, and p_c is the percolation threshold.

Remarkably, the closely related bimodal problem of the links of a network having a high conductivity $\sigma(high)$ with probability p, or a low but finite conductivity $\sigma(low)$ with probability $(1-p)$ has been rarely analyzed. Efros and Shklovskii (ES) established the broad framework for the analysis, when they made the analogy between this bimodal distribution problem and the problem of how the critical behavior of a spin system gets modified by the presence of a symmetry breaking magnetic field [**96**]. They hypothesized a power law critical behavior for the network conductivity,

where the universal scaling function at the critical point $p = p_c$ is anchored by the ratio of the high and low conductivities. However, they did not determine either the critical exponents, or the universal scaling function.

6.3.3. Finite size scaling: Next, we attempt to adapt the ES bimodal framework to describe our TRIDENS-simulated results. The finite size L of the simulated samples makes it necessary to analyze the results by finite size scaling. Normally this is handled by the introduction of a scaling function with a single variable: the ratio of the sample size L to the correlation length $\xi = \xi_0 P^{-\nu}$, where $P = \frac{|p-pc|}{pc}$ that smoothes over the non-analytic critical behavior.

However, for the present, bimodal mobility distribution problem ES argued that the ratio of conductivities plays the role similar to an external magnetic field in a critical magnetic system: $\frac{\sigma_{low}}{\sigma_{high}} = h$, and already smoothes over the critical behavior. Therefore, the model needs to be analyzed by a two variable finite size scaling form, where the ratio L/ξ is a second factor that smoothes the critical behavior:

$$\mu(P, L, h) = P^{-\alpha}\mu(hP^{-\Delta}, LP^{\nu}) \tag{6.1}$$

where $\mu(x, y)$ is the universal finite size scaling function, and α, ν and Δ are critical exponents. The analysis is more tractable if the singular P dependence is absorbed by factoring out $hP^{-\frac{\alpha}{\Delta}}$ from μ, leaving us with:

$$\mu(P, L, h) = h^{-\alpha/\Delta}\mu'(hP^{-\Delta}, LP^{\nu}) \tag{6.2}$$

Since $\mu'(x, y)$ is a two-variable function, the full testing of the finite size scaling hypothesis would require a quite extensive computational effort. Therefore, we narrowed our analysis of the finite size scaling assumption to the first variable, $hP^{-\Delta}$, while keeping the second variable, LP^{ν}, constant. As the lattice sizes were varied from $L = 32$ to $L = 128$, keeping LP^{ν} constant required the appropriate modification of P. We then chose the h values so that the critical regime on either side of the critical point p_c was well sampled.

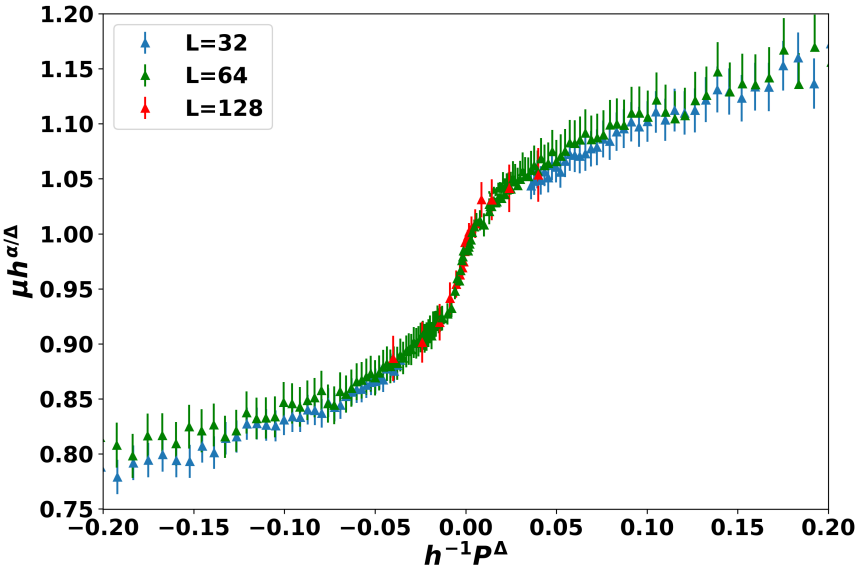

FIGURE 6.5. Scaled data of $\mu h^{\alpha/\Delta}$ vs. $h^{-1}P^{\Delta}$ for 3 different lattice sizes. The product LP^{ν} is held constant.

Fig. 6.5 shows the scaled mobility $h^{\alpha/\Delta}$ as a function of $h^{-1}P^{\Delta}$ for a fixed value of LP^{ν}, for three lattice sizes, varying from $L = 32$ to $L = 128$. Reassuringly, we were able to achieve very good data collapse within the $(-0.1, 0.1)$ critical regime around the critical point at $P = 0$, which remained acceptable out to $(-0.2, 0.2)$. Using the literature values of $\nu = \frac{4}{3}$ and $p_c = 0.5$, the best collapse was reached with exponents $\alpha = -0.99 \pm .02$ and $\Delta = 2.02 \pm .02$.

The success of the finite size scaling shows that the Efros Shklovskii analogy to critical spin systems in an external magnetic field is indeed appropriate for this bimodal percolation problem: as the fraction p of the high mobility undefected NP SLs increases, one can think of the evolution of the overall mobility as a modified percolation transition, rounded by the finiteness of the mobility of the low mobility NP SLs. As far as the authors know, this is the first report of the critical exponents and the universal scaling function of the bimodal distribution resistor network problem.

The following points are worth making. Fig. 6.5 shows that the overall network electron mobility, or conductivity, displays a marked transition from a low mobility insulator behavior when the high mobility NP SLs do not percolate yet, to a high mobility insulator behavior once the high mobility NP SLs percolated. Of course, both of these regimes are insulators, so while the

geometry of the NP solid undergoes a genuine percolation transition, the conductive properties exhibit only a low mobility insulator-to-high mobility insulator transport crossover, not a genuine phase transition.

We have studied a version of this problem recently on the level of our HINTS code [**50**], where the NPs were connected with either low mobility activated insulating links, or high mobility, non-activated metallic links. In that version of the problem, the underlying percolation transition of the metallic links of the NP solid drove a genuine metal-insulator-transition (MIT), as the percolation of the metallic links created a genuine metallic phase. We conceptualized that MIT as a Quantum Percolation Transition, and adapted the ES bimodal mobility distribution percolation model for its description, as at any fixed temperature that version of the problem also consisted of a bimodal mobility distribution with low mobility links and high mobility links. Whether the high mobility phase is a metal or a high mobility insulator can be identified from the temperature dependence of its conductivity. In the absence of the present detailed finite-size scaling study, in Ref. [**50**] we developed a simple, mean-field model form for the scaling function that described the mobility's evolution from the low mobility insulator to the high mobility metal. With the notation of the present paper, the mean field exponents were $\alpha = -1$ and $\Delta = 1$. This enabled us to create the dynamical phase diagram of the model on the electron filling – disorder plane, where the MIT separated the insulating phase with activated conductivity from the metallic phase with non-activated conductivity.

The present bimodal TRIDENS study scales up our previous bimodal HINTS work to much larger length scales. The key distinction is that the building blocks of the HINTS network were the individual NPs, whereas in TRIDENS the building blocks are the NP SLs with around a thousand NPs (in the present work, with 800 NPs). Further, in HINTS the origin of the bimodal mobility distribution was the presence or absence of metallic links between individual NPs, whereas here the origin of the bimodal mobility distribution is the presence or absence of an planar defect across the individual NP SLs. Obviously, the HINTS transport modeling that tracks individual electrons transitiong between individual NPs is more detailed than the resistor network of the present TRIDENS work. Nevertheless, since the building blocks of both the bimodal HINTS and the bimodal TRIDENS are low mobility links and high mobility links, we expected that the same

ES bimodal percolation model with the same universal scaling function and exponents will capture the critical behavior of the bimodal TRIDENS results. The success of the data collapse with the ES finite size scaling form validated this expectation. While, of course several different analytic forms can be fitted to the universal scaling function that emerged in Fig. 6.5, nevertheless it was reassuring that in particular the mean-field function of the bimodal HINTS study:

$$\mu'(hP^{-\Delta}, LP^{\nu} \to \infty) = 1/(1 + P/h) \tag{6.3}$$

was also consistent with it. Further, the $\alpha = -0.99$ exponent of the TRIDENS scaling is approximately equal to the $\alpha = -1$ mean field value within the margin of error. We noted that there was a difference regarding the Δ exponent: TRIDENS gave a $\Delta = 2.02$, whereas in the mean field theory $\Delta = 1$. However, such differences occur typically between mean-field and numerically determined exponents. All in all, the substantial correspondence between our HINTS and TRIDENS works demonstrated that the ES bimodal percolation model is a good, quantitative description of how the underlying percolation transition of the NP solid drives a low-mobility insulator-to-high-mobility insulator transport crossover.

For completeness we mention that we implemented TRIDENS with randomly selecting high or low mobility NP SLs for the links. This corresponds to planar defects with a length of tens of NPs. However, the sample in Fig.6.1 has many defects that are much longer. Such long defects can be modelled by selecting defected SLs along lines of links in TRIDENS, in a correlated manner. Such correlated TRIDENS models will be pursued in a future work.

6.4. Conclusions

Transport in nanoparticle solids must be simulated on extremely large length scales, corresponding to millions of NPs, because NP solids exhibit spatial structures on several length scales, from the subtleties of individual NPs through the sensitive modeling of inter-NP transitions and through transport across homogeneously disordered SLs all the way to transport in NP SLs with large planar defects. Single-level computational methods are manifestly unable to span these length

scales. This is why in our previous work we developed the multi-level HINTS method that was capable of simulating transport across NP solids with up to a thousand NPs. However, even HINTS is unable to capture the effect of planar defects on transport in NP solids of the size of tens of microns.

In this paper, we reported the development of the TRIDENS method that adds three further hierarchial layers on top of the HINTS method. In TRIDENS, we first introduced planar defects into individual NP SLs that comprised the order of about a thousand NPs. Then we used HINTS to simulate the transport across these defected NP SLs. We performed these HINTS transport simulations for tens of thousands of defected NP SLs, and constructed the distribution of the NP SL mobilities with planar defects. Second, the defected NP SLs were assembled into a resistor network with more than 10^4 NP SLs, thus representing about 10^7 individual NPs. This translated to length scales of tens of microns, approaching the experimental scales for NP solids. Third, and finally, the TRIDENS results were analyzed by finite size scaling to explore whether the percolation transition, separating the phase where the low-mobility-defected NP SLs percolate from the phase where the high-mobility-undefected NP SLs percolate, drives a low-mobility-insulator-to-high-mobility-insulator transport crossover that can be extrapolated to genuinely macroscopic length scales.

Our extensive TRIDENS analysis generated the following results. On the level of individual NP SLs, we found that the average of the mobility for undefected NP SLs was 0.42 ± 0.1 cm^2/Vs, for twin-plane-defected NP SLs 0.16 ± 0.06 cm^2/Vs, and for grain-boundary-defected NP SLs 0.09 ± 0.05 cm^2/Vs. On average, grain boundary defects hinder transport about twice as much as twin planes. This result makes sense, as grain boundaries are more disruptive to lattice periodicity than twin planes, and transport across the grain boundaries involves longer hops between more distant NPs, whereas transport across twin planes proceeds across many NPs shared by the grains on the two sides of the twin plane, and thus it involves regular hop lengths. It is noteworthy that the introduction of planar defects into NP SLs reduced their mobility by a factor of up to 5. On one hand, this is a substantial suppression of the mobilities that drives a transport crossover, and thus demonstrates the imperative of minimizing the density of planar defects in NP solids to help their suitability for applications. On the other hand, this is not a qualitative, order-of-magnitude

suppression of the transport that indicate a Metal-Insulator-Transition: those are driven by the loss of phase coherence.

On the highest, resistor network-level analysis of TRIDENS, we observed that the introduction of the planar defects immediately started to reduce the network mobility. This finding suggests that even small concentrations of planar defects are not shorted out in NP solids, and thus every reduction of the density of planar defects will lead to further improvements of the transport in NP solids. Among the planar defects, the elimination of grain boundaries pays more dividends than that of twin planes.

For the theoretical description, we adapted the Efros-Shklovskii bimodal mobility distribution percolation model. We performed a finite size scaling analysis of the TRIDENS network mobilities. We demonstrated that increasing the density of the undefected NP SLs drives an underlying, structural/geometric percolation transition in the NP solid, which in turn drives a low-mobility-insulator-to-high-mobility-insulator transport crossover. We demonstrated that our adaptation of the ES bimodal theory's two-variable scaling function is an effective tool to quantitatively characterize this low-mobility-insulator-to-high-mobility-insulator transport crossover. For context, we discussed the analogies with the Quantum Percolation Transition we developed in our earlier, MIT-focused work [**50**].

CHAPTER 7

From Femtoseconds to Gigaseconds: The SolDeg Platform for the Performance Degradation Analysis of Silicon Heterojunction Solar Cells

7.1. Introduction

7.1.1. Solar Cell Degradation. Heterojunction (HJ) Si solar cells have world record efficiencies approaching 27%, due to the excellent surface passivation by their amorphous Silicon (a-Si) layer that leads to low surface recombination velocities and high open circuit voltages V_{OC}. In spite of the impressive efficiency records, HJ Si cells have not yet been widely adopted by the market because of the perceived challenge that HJ cells may exhibit accelerated performance degradation, possibly related to their a-Si layer. Traditional crystalline Si (c-Si) modules typically exhibit about a 0.5%/yr efficiency degradation, primarily via their short circuit current I_{sc} and the fill factor FF, typically attributed to external factors, such as moisture ingress and increased contact resistance. In contrast, in 2018 two papers reported studies of the degradation of fielded Si HJ modules over 5-10 years [**59**, **60**]. They reported degradation rates close to 1%/yr, about twice the rate of traditional cells. These papers pointed to a new degradation channel, the decay of V_{OC}, at a rate of about 0.5%/yr. The decay of V_{OC} suggests that the degradation is possibly due to internal factors, increasing recombination either at the a-Si/c-Si interface, or in the a-Si layer. Such increased recombination is typically caused by the increase of the electronic defect density.

These initial reports on fielded panels were followed up by in-laboratory analysis. The Bertoni group has studied the surface recombination velocity (SRV) at the a-Si/c-Si interface in HJ stacks. By applying a model for the recombination at the a-Si/c-Si interface to their temperature- and injection-dependent SRV data, they analyzed the degradation of the carrier lifetime and were able to attribute it to a loss of chemical passivation [**61**]. More recently, Holovsky et al. investigated ultrathin layers of hydrogenated amorphous silicon (a-Si:H), passivating the surface of crystalline

silicon (c-Si) [**62**]. These authors applied highly sensitive attenuated total reflectance Fourier-transform infrared spectroscopy, combined with carrier lifetime measurements. They manipulated the a-Si/c-Si interface by applying different surface, annealing, and aging treatments. Electronic interface properties were discussed from the perspective of hydrogen mono-layer passivation of the c-Si surface and from the perspective of a-Si:H bulk properties. They concluded that both models have severe limitations and called for a better physical model of the interface [**62**].

7.1.2. Defects in Amorphous Si. Photoinduced degradation of a-Si under prolonged exposure to intense light was first studied, measured and modeled by Staebler and Wronski [**160**]. They reported that the degradation is characterized by a remarkably universal $t^{1/3}$ power-law temporal growth of the defect density. This behavior has become known as the Staebler-Wronski effect (SWE).

The SWE was analyzed by different methods. Some groups performed electron spin resonance (ESR) measurement on a-Si (a-Si:H) to experimentally detect the increase of the density of dangling bonds induced by light exposure [**161**,**162**,**163**]. Some of these papers also developed a phenomenological model to predict the SW defect-increase as a function of exposure time and light intensity. Other groups used the photocurrent method (PCM) to detect the change of defect density of a-Si under light exposure. In agreement with ESR experiments, PCM also revealed the increase of defect density under light exposure. While the ESR and PCM defect density measurements yielded analogous results, it is recalled here that they capture different type of defect states [**164**, **165**]. ESR detects all neutral defect states that only include dangling bonds (DBs), while PCM detects both neutral and charged defect states that include DBs and other types of defect states. Therefore PCM measurements revealed that the origin of defect states might be a result of different type of general structural disorders beyond DBs. [**166**, **167**]

Recently, Wronski argued that three distinct defect states, A/B/C, are needed to account for all the data, instead of the standard single "midgap dangling bond" defect [**168**]. The A/B states are efficient electron recombination centers, while the C states recombine holes efficiently. Wronski speculated that these states are differentiated by their different structures: dangling bonds, mono- and divacancies, as also advocated by Smets. Other groups also analyzed their data in terms of three distinct states [**61**,**64**]. However, they focused on the alternative picture that the defect states

may be the three charge states H+, H0, and H- of hydrogen. In addition to these experimental works, recent theoretical and computational papers also analyzed the defect states in a-Si, and they concluded that besides dangling bonds, highly strained bonds also contribute to midgap states significantly [**169**, **170**].

To summarize, while a fair amount of progress has been achieved in characterizing defect generation in a-Si, its underlying mechanism and connection to the different types of structural disorder and defects is far from being settled and understood. The problem is still open to question. For this reason, in this paper we analyze the above problem of defect generation in a-Si/c-Si heterojunction solar cells, with a possible relevance for PERC cell passivation.

7.2. Methods and Results

7.2.1. The SolDeg Platform. To address the above-described *Sol*ar cell *Deg*radation, we have developed the SolDeg platform to model electronic defect generation in a-Si/c-Si heterojunctions, which consists of the following hierarchical stages. (1) Creating a-Si/c-Si stacks. (2) Generating shocked clusters as likely hosts of electronic defects. (3) Identifying shocked clusters that actually host electronic defects. (4) Determining the energy barriers that control the generation of these electronic defects; and determining their distribution. (5) Determining the temporal evolution of the defect density from the energy barrier distribution. This SolDeg platform is described next in detail.

7.2.2. Creating the Amorphous/Crystalline Si Stacks: Machine-Learning Driven Molecular Dynamics. The SolDeg platform starts with creating a-Si/c-Si heterojunction structures, or stacks. We first created pure a-Si structures, which were carefully optimized in order to match lab-grown a-Si as closely as possible. Second, we placed these optimized a-Si structures on top of slabs of c-Si, and then annealed the interface region. This approach was chosen in order to create the most realistic a-Si atomic structures possible, while still yielding a reasonable aSi/cSi interface region. The details of this approach are as follows.

To create pure amorphous Si structures, one performs melt-quench molecular dynamics (MD) simulations. In a melt-quench MD simulation, a crystalline Si structure is heated past its melting point to generate liquid Si, which is then quenched down to low temperatures at an appropriate

rate. This method is widely used for generating amorphous Si networks. It is known that the choice of the interatomic potential used for these MD simulations has a substantial effect on the results. Classical parametric interatomic potentials, such as the Tersoff [**171**] and Stillinger-Weber (SW) [**172**] potentials, have a limited number of parameters/descriptors, and are typically fitted against experimental structural data under a specific set of conditions such as a particular material composition and temperature range. As such, their accuracy in reproducing a wider variety of structural properties of the specific material, or in simulating different temperature ranges or material structures than they were fitted to, often limits the precision of the results.

For example, the excess energy (energy compared to diamond-type Si) of the a-Si resulting from melt-quench simulations performed with these interatomic potentials is typically > 0.20 eV/atom, falling outside of the lab-grown a-Si excess energy range of $0.07 - 0.15$ eV/atom [**173**, **174**, **175**]. The defect densities, e.g. the density of dangling and floating bonds, also differ from typical lab-grown a-Si data. MD simulations with these interatomic potentials are also unable to reach DFT-level accuracy in determining elastic constants and defect formation energies. For all the above reasons, the MD-created a-Si systems need to be further optimized by Density Functional Theory (DFT) [**170**]. However, the need to use DFT slows down the computational time substantially, and thus limits the accessible system sizes substantially.

To improve the accuracy of our MD simulations in all aspects compared to using these standard interatomic potentials, we instead adopted a Machine-Learning driven general-purpose interatomic potential which has been created for Si [**176**]. This machine-learning driven approach uses the framework of the Gaussian approximation potential (GAP) with a smooth overlap of atomic positions (SOAP) kernel, and has been specifically developed so that GAP-based MD simulations yield DFT-level accuracy, even though they are 10x more efficient, thus enabling the faster simulation of larger systems [**177**, **178**]. Hereafter, we will refer to this potential simply as the Si GAP. It has been shown that the Si GAP captures more than a dozen experimentally measured quantities significantly better than any of the other available interatomic potentials [**176**]. We show below that adopting the Si GAP for our MD simulations yield superior a-Si structures after only a minimum level of DFT optimization. Now we proceed with the technical simulation details.

We generated the a-Si/c-Si stacks by MD simulations, carried out using the LAMMPS software package [**179**]. The simulation time step was 1 fs. Our melt-quench simulations started with crystalline Si cubic supercells containing 216 Si atoms, with three dimensional (3D) periodic boundary conditions. The lattice constant a_0 was chosen to be 5.43 Å, and the dimensions of the supercell $a = b = c = 3a_0$. This lattice constant was chosen to ensure that the mass density of the resulting a-Si structures was 1-3% lower than the mass density of corresponding c-Si structures, consistent with the mass density measured by experiments on a-Si/c-Si stacks.

The crystalline Si was first heated to 1800K to yield liquid Si. The liquid Si was subsequently re-solidified by cooling down to 1500K at a rate of 10^{13} K/s before being equilibrated at 1500K for 100 ps. This solid Si was quenched further down to 500K at a rate of 10^{12} K/s, following previous studies [**176**, **180**, **181**, **182**]. The first quench was performed in the constant-volume and variable-pressure (NVT) ensemble, while the second quench was performed in the variable-volume and constant-pressure (NPT) ensemble with fixed x and y cell-dimensions (to match the dimensions of the c-Si unit cell in the later steps), both using a Nosé-Hoover thermostat and barostat. We minimized the structural energy using a GAP-driven Hessian-free truncated Newton (HFTN) algorithm to relax all atomic positions into their local minima.

These relaxed a-Si structures were further optimized with DFT, specifically making use of the Quantum Espresso 6.2.1 software package [**183**, **184**]. We used the Broyden-Fletcher-Goldfarb-Shanno (BFGS) quasi-newton algorithm, based on the trust radius procedure, as the optimization algorithm.

The Perdew-Burke-Ernzerhof (PBE) exchange-correlation functional [**185**] was used in both the ionic relaxation and the electronic structure calculations using periodic boundary conditions. The core and valence electron interactions were described by the Norm-Conserving Pseudopotential function. Unless otherwise stated, an energy cutoff of 12 Ry was employed for the plane-wave basis set and a 2×2×2 k-point mesh was used with the Monkhorst-Pack grid method for the Brillouin-zone sampling in all the calculations. Methfessel-Paxton smearing [**186**] of width 0.05 Ry was applied to determine the band occupations and electronic density of states.

Motivated by Pedersen et al., we use the excess energy, the bond angle distribution, and the radial distribution function (RDF), as the most compelling criteria to validate our generated a-Si

structures against a-Si experiments [**188**]. In our structures the typical excess energies were around $0.13-0.14\,\text{eV/atom}$, well within the experimentally acceptable range of $0.07-0.15$ eV/atom. These remarkably low excess energies strongly validate the superiority of the Si GAP over traditional potentials, which yield excess energies above 0.20 eV/atom. The bond-angle distribution was centered at 109.1° with a width of ±10.5°. These values are also consistent with typical experimental values [**189**]. The average Si-Si bond length was $2.38\,\text{Å} \pm .04\,\text{Å}$. Assuming a Si-Si bond-length cutoff of 2.58 Å, slightly less than 10% longer than the average bond-length, the average number of dangling bonds in each supercell was 2.2, and the average number of floating bonds was 0.8. Dangling (floating) bonds are missing (extra) bonds of a Si atom relative to the standard number of 4. Finally, the structures were further validated by calculating the radial distribution function (RDF). The RDF measures the probability of finding the center of an atom at a given distance

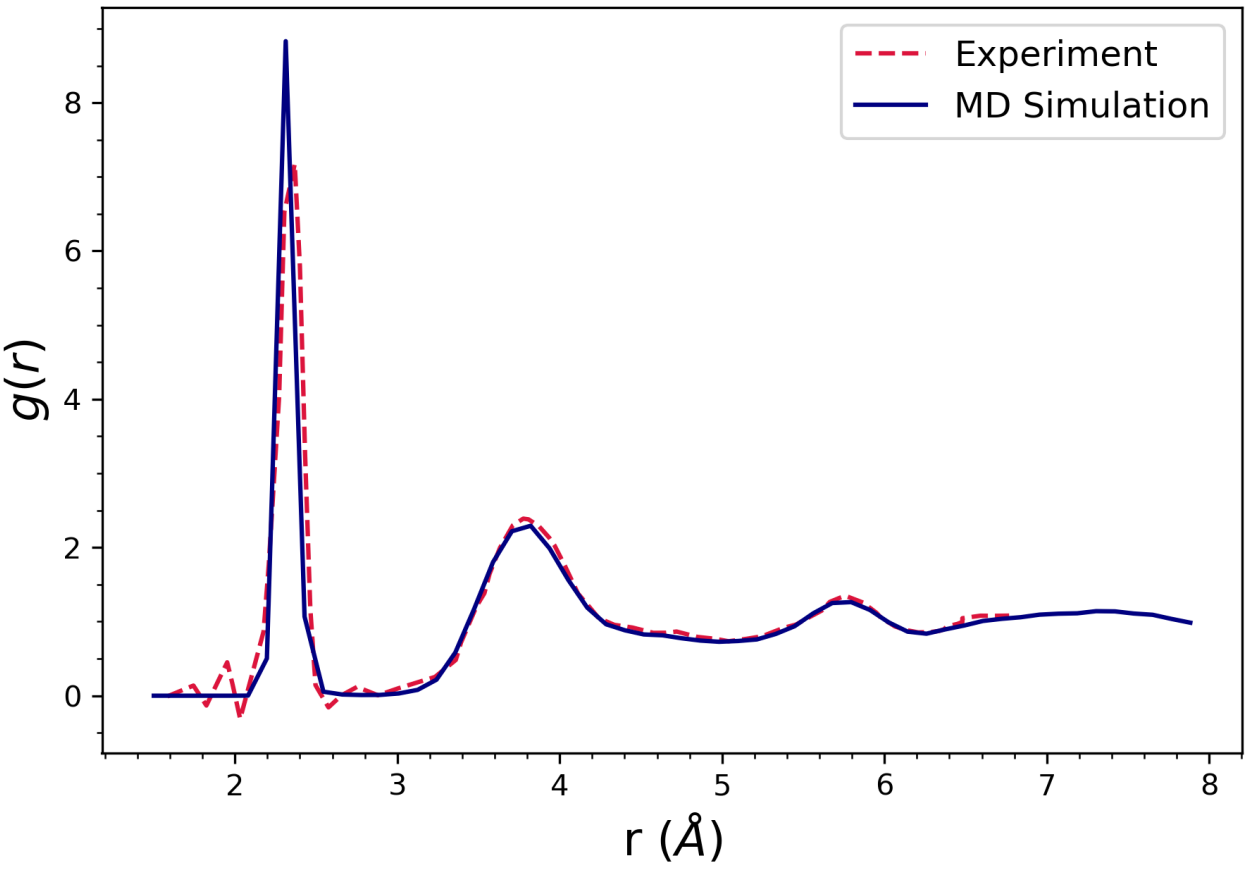

FIGURE 7.1. Radial distribution function $g(r)$ characterizing a typical melt-quench MD a-Si structure, plotted against the experimental values of ref. **187**

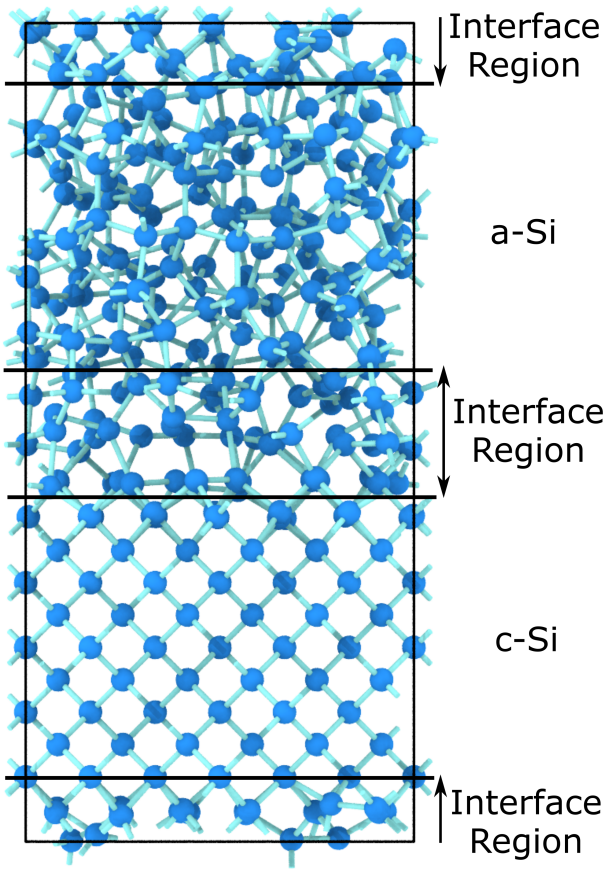

FIGURE 7.2. Rendering of a simulated Si-heterojunction structure. Periodic boundary conditions result in the presence of two distinct interface regions.

from the center of another atom as a function of their radial separation. For a-Si, the typical RDF exhibits a strong peak centered at 2.3 Å, and two weak peaks centered around 3.8 Å and 5.4 Å (the next-nearest and next-next-nearest neighbor distances in c-Si). As shown in Fig. 1, the RDFs calculated from our GAP-MD generated structures track the experimental data compellingly.

We created the Si-heterojunction structures by placing the DFT-optimized a-Si on top of c-Si slabs (of the same dimensions and number of atoms as the a-Si structures). See Fig. 7.2. Note that requiring periodic boundary conditions for the a-Si/c-Si stacks forces two a-Si/c-Si interfaces into the structure, as shown. At both interfaces, the a-Si was placed 1.36 Å ($a_0/4$) away from the edge of the c-Si slab. This distance was chosen by calculating the total energy of a series of structures where this distance was systematically varied, and choosing the distance which yielded the lowest total energy.

The resulting a-Si/c-Si interfaces are highly strained. For this reason, we relax each interface via thermal annealing. To avoid altering the structure of the carefully optimized a-Si layers, we only annealed a strip of width a_0 centered symmetrically at each a-Si/c-Si interface. The annealing was performed at 450K for 25 ps, and was followed by cooling down to 270K at a rate of 10^{13} K/s. Both steps were performed in the NVT ensemble with a timestep of 1 fs. In total, we created 50 a-Si/c-Si structures.

7.2.3. Defect Generation: Shocked Cluster Generation by the Cluster Blaster. Our overarching theory is that the HJ cell performance degradation is driven by the generation of electronic defects that act as recombination centers. We further posit that most of the electronic defects are generated by a small group of Si atoms in the a-Si transitioning from their moderately disordered cluster into a highly disordered cluster by thermal activation over an energy barrier. The transition into this highly disordered cluster can strain or break the Si bonds, thereby creating electronic defects, such as strained or dangling bonds.

We decided to create highly disordered, "shocked" clusters by heating the cluster very quickly to excessive temperatures, followed by a comparably quick cooling: a procedure we refer to as the "cluster blaster". Using LAMMPS [**179**] and the ML-based Silicon Gaussian Approximation Potential (GAP) [**176**], described in the previous section, we blasted clusters of 5 atoms in our a-Si/c-Si stack, centered at the crystalline/amorphous interface to a temperature of $T = 5000$K while keeping the rest of the structure frozen. We chose $T = 5000$K, because we found that temperatures significantly below this value were not efficient at generating electronic defects in our systems, to be described below. We allowed the shocked clusters to evolve at this elevated temperature for 20 ns so that they could explore their configuration space extensively. After 20 ns, the shocked clusters were quenched quickly, so that they could not escape whichever highly disordered metastable configuration they were nearest to. We then performed a Hessian-free truncated Newton optimization of the quenched shocked clusters, again using the Si GAP. This cluster blaster process was repeated at the interfaces of all of our 50 a-Si/c-Si stacks at about 30 different locations each, eventually creating about 1,500 shocked clusters with the cluster blaster.

7.2.4. Defect Generation: Analysis of the Shocked Clusters for Electronic Defects. The cluster blaster does not always induce electronic defects in the shocked clusters. To identify which cluster blasting induced electronic defects as well, the next stage of SolDeg is to measure the orbital localization of the electronic states in the a-Si/c-Si stacks with shocked clusters.

We determined the localization of the Kohn-Sham electronic orbitals in the a-Si/c-Si structures before and after the cluster blasting by using the inverse participation ratio (IPR) method. The IPR for an eigenstate Ψ_n is given as:

$$IPR_n = \frac{\Sigma_{i=1}^{I} a_{ni}^4}{(\Sigma_{i=1}^{I} a_{ni}^2)^2} \tag{7.1}$$

where a_{ni} is the coefficient of i^{th} basis set orbital in n^{th} Kohn-Sham orbital Ψ_n ($\Psi_n = \Sigma_{i=1}^{I} a_{ni}\phi_i$) and I is the total number of basis set orbitals used in the DFT calculation. The higher the IPR, the higher the degree of localization. The IPR for a state extended equally over all atoms is close to zero (O(1/N)), and for a state completely localized state on only one atom is one.

Fig. 7.3(a) shows the IPRs, calculated for all Kohn-Sham orbitals obtained by DFT as a function of their energy for a typical a-Si/c-Si stack. Visibly, the majority of the electronic states are localized in the energy region of 5.5-7 eV, lying between the conduction band and the valence band. This region can be identified as a mobility gap because the electronic states are localized within. In contrast, the majority of the states are delocalized inside the conduction and valence bands. It is recalled that the mobility gap often differs somewhat from the density of states (DOS) gap, since the electronic states in the tails of the conduction and valence bands can be localized, separated from the delocalized continuum of band states by a "mobility edge".

In order to determine the localization of the electronic orbitals more we rearrange Eq. 7.1 as follows:

$$IPR(\Psi_n) = \frac{\Sigma_{k=1}^{K}\Sigma_{j=1}^{J} a_{nkj}^4}{(\Sigma_{k=1}^{K}\Sigma_{j=1}^{J} a_{nkj}^2)^2} \tag{7.2}$$

where a_{nkj} is the coefficient of j^{th} atomic orbital belonging to the k^{th} atom in the n^{th} Kohn-Sham orbital. J is the total number of atomic orbitals used in DFT calculations, which belong only to the k^{th} atom in the supercell, and K is the total number of atoms inside the supercell. We

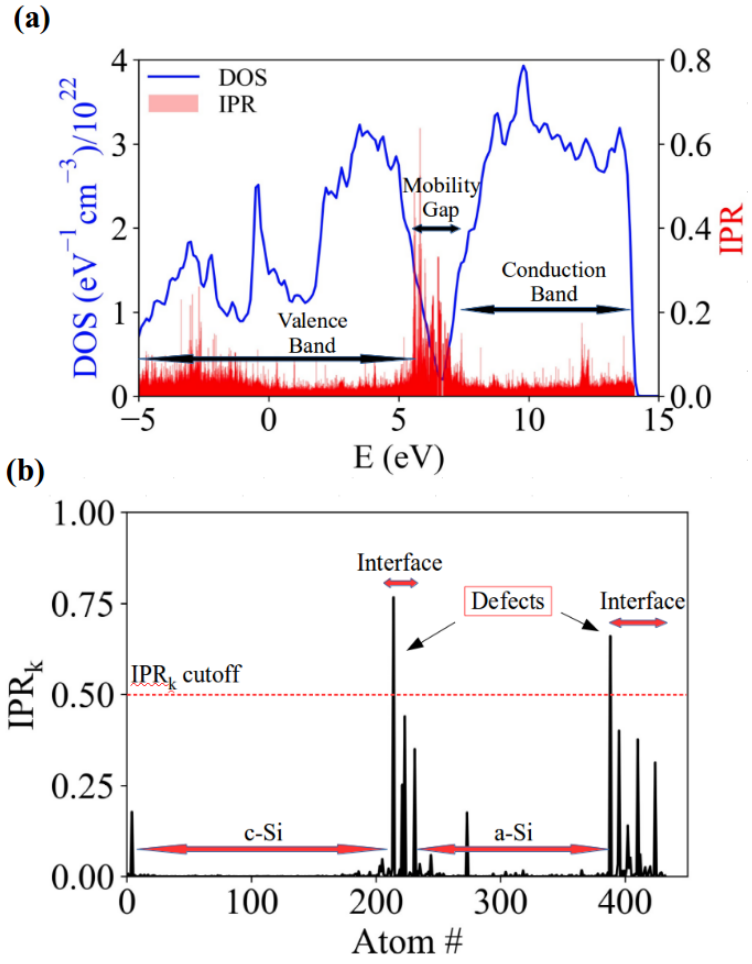

FIGURE 7.3. (a) IPR and (b) IPR_k of typical a-Si/c-Si structures.

introduced the concept of Eq. 7.2 because it is capable of identifying not only that an electronic state is localized, but the location of the atom where it is localized as well by defining a quantity IPR_{nkj} as follows: [**170**]

$$IPR_{nkj} = \frac{a_{nkj}^4}{(\Sigma_{k=1}^{K}\Sigma_{j=1}^{J}a_{nkj}^2)^2} \tag{7.3}$$

Here IPR_{nkj} is the contribution of the k^{th} atom through its j^{th} atomic orbital in the localization of the n^{th} Khon-Sham orbital. One notes that the denominator of Eq. 7.3 is the same for the all IPR_{nkj} for a given n. Thus, the number of IPR_{nkj} values for a given k atom for each Kohn-Sham

orbital is J. Denoting the number of Kohn-Sham orbitals as N, each atom in the supercell has NJ IPR_{nkj} values. In order to assign only one IPR value to each atom k, we choose the maximal IPR_{nkj} from among the NJ IPR_{nkj} values for a fixed k. We name this maximal value IPR_k:

$$IPR_k = MAX^k_{n,j}\{IPR_{nkj}\} \tag{7.4}$$

Fig. 7.3(b) shows IPR_k for a typical a-Si/c-Si structure, as a function of the atom number k, approximately translating into the z-coordinate of the atoms. As expected, almost all of the localized states are located at the interfaces. There are no localized states in the c-Si, and only one localized state in the a-Si. This localized state distribution is reasonable given the high degree of strain at the interface, in contrast to the low strain in the a-Si, and minimal strain in the c-Si. We identify electronic states as genuine electronic defects as long as they are mostly localized on a single atom, This is captured by their IPR_k value exceeding a threshold which we take as 0.5. With this threshold convention, visibly there is only one defect at each interface in Fig. 7.3(b).

Once the IPR calculations have been completed, we can determine whether electronic defects have been successfully created in the shocked clusters by the cluster blaster. As somewhat of a surprise, we found that quite often the cluster blasting in fact did the opposite: it annealed out an already existing electronic defect instead of creating one. Therefore, we broadened the scope of our search to identify pairs of initial and final states of the cluster blasting in which the number of electronic defects differed by precisely one. This protocol picked up both the creation and the annihilation of electronic defects in the shocked clusters. We chose to only track initial-final state pairs that differed by a single defect to avoid the need of tracking defect-defect interactions that may affect our results.

7.2.5. Determining Energy Barriers and Their Distribution with the Nudged Elastic Band Method. In the next stage of SolDeg, we determined the energy barriers that control the creation and annihilation of the identified electronic defects because thermal activation across these barriers controls the temporal increase of the overall electronic defect density in a-Si/c-Si stacks, aged in the dark. We will return to light-induced defect generation in a later paper.

Once pairs of initial and final states have been identified where a single electronic defect was either created or annihilated, we employed the nudged elastic band (NEB) method [**190**, **191**, **192**, **193**] to determine the energy barrier heights between these initial and final states. The nudged elastic band method connects two different local energy minima with several intermediate replica states, each connected to its nearest state neighbor with a "spring" that is nudged perpendicular to the path through state space to allow the "band" to find a saddle point. The NEB method is a standard tool for determining minimum energy paths between states in some fields, but to our knowledge, the NEB method has not been used in the solar field yet, so we will describe the method in some detail here.

NEB starts with an initial guess of a sequence of intermediate "replica" states between an initial and a final state. NEB then postulates an abstract "spring" between the adjacent replica states, to generate a tendency for sequence of replica states to evolve towards a compact, possibly lower energy path between the initial and final state.

The NEB method uses two force components to cause the replica sequence to evolve toward the sought-after minimum energy path (MEP). One of these, the longitudinal component of spring force that connects adjacent replica states is given by:

$$F_i^S = [k(\mathbf{R_{i+1}} - \mathbf{R_i}) - k(\mathbf{R_i} - \mathbf{R_{i-1}})] \cdot \hat{\tau}\hat{\tau} \tag{7.5}$$

where $\mathbf{R_i}$ represents the position of the i^{th} replica in the energy landscape, k is the spring constant, and $\hat{\tau}$ is the "longitudinal" unit vector, parallel with the "spring" at replica i.

The other, lateral force component is perpendicular to the "spring", exerted by the gradient of the energy surface. As such, this force component nudges the spring towards the MEP. In our SolDeg platform, the energy surface was computed with the Si GAP.

$$F_i^V = -\nabla V(\mathbf{R_i}) + \nabla V(\mathbf{R_i}) \cdot \hat{\tau}\hat{\tau} \tag{7.6}$$

where V is the potential energy landscape. The advantage of the NEB method over a standard elastic band method is that artifacts involved with the band cutting corners off the MEP are not a problem for the NEB method.

Our NEB simulations were performed in LAMMPS using the Si GAP [**176**]. We used 32 replicas for each simulation. In our simulations we kept the non-heated atoms fixed: only the heated atoms were allowed to move replica-by-replica. The energy stopping tolerance was 10^{-6} (unitless), and the force stopping tolerance was 10^{-6} eV/Å. The simulation timestep was 10 fs. We used the *fire* minimization algorithm, a damped dynamics method with a variable time step [**194**].

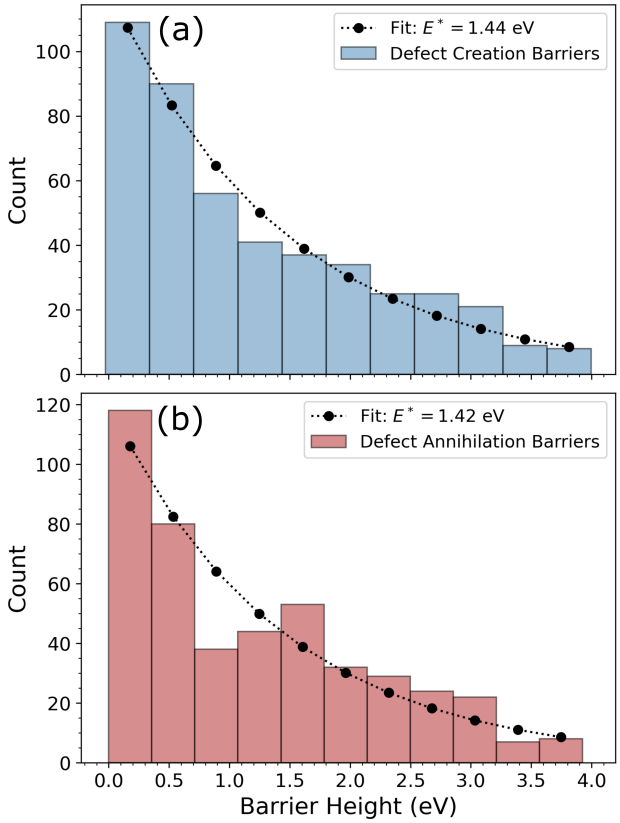

FIGURE 7.4. Energy barrier distributions for: (a) defect creation; and (b) defect annihilation. Black symbols and lines: exponential fit with: $P(E) = (1/E^*)\exp(-E/E^*)$

The results of our NEB calculation are shown in Fig. 7.4. The distribution of the barriers for the defect creation processes is shown in panel (a), while the distribution of the barriers for defect annihilation processes (a reverse transition across the defect creation barrier) is shown in panel (b).

Because of the similarity of the two distributions, both the creation and the annihilation processes will impact the time evolution of the defect density. Importantly, Fig. 7.4 reveals an extremely broad distribution of barriers, from meV to 4 eV. Such an extremely broad barrier distribution is the hallmark of glassy phenomena, and is the driving force behind the defect density growing not only on microscopic time scales but also on the time scale of years.

7.2.6. Determining the Temporal Evolution of the Defect Density N(t) From the Barrier Distribution. In the last stage of the SolDeg platform, we determined the temporal evolution of the defect density from microscopic times scales to 20 years, the standard length of solar cell performance guarantees.

In order to determine the defect density as a function of time, we turned to kinetic Monte Carlo methods. We begun by creating samples with 20,000 individual two-state "clusters" that each could transition from a non-defected state to a defected state by overcoming a defect creation energy barrier, and transition from a defected state to a non-defected state by overcoming a defect annihilation energy barrier. For each cluster transition, the energies for these creation and annihilation processes were drawn from the two barrier distributions determined in the previous section. We eliminated artificial fluctuations induced by the discrete binning of the barriers by representing the distributions with their smooth fitted forms, as shown in Fig. 7.4. The clusters transition over the barriers by thermal activation, with an associated rate of

$$\Gamma = \Gamma_0 e^{\frac{-E}{kT}}, \tag{7.7}$$

where Γ_0 is a characteristic attempt frequency of the cluster to overcome its energy barrier, taken here to be 10^{10} s^{-1}. These rates are calculated for each cluster and summed to determine the "total rate", Γ_{tot}. Next, an event is randomly selected from the possible pool of events, with the probability of selecting event i being equal to $P(i) = \frac{\Gamma_i}{\Gamma_{tot}}$. The time is then moved forward according to $\Delta t = \frac{-ln(r)}{\Gamma_{tot}}$, where r is a random number. This is equivalent to sampling a Poisson waiting time distribution.

The above described method becomes computationally prohibitive when the phenomena of interest are rare events, with rates of occurrence that are several orders of magnitude smaller than

typical events. Not only are these rare events exceptionally unlikely to be chosen by the KMC algorithm, but the number of simulation steps needed to evolve the simulation time far enough to see the rare events will be impossibly large. Using our base kinetic Monte Carlo algorithm, without any acceleration efforts, a million simulation steps only evolve the simulation time by one-hundredth of a second. This is completely inadequate to determine degradation that occurs on the scales of months or years.

Our solution to this problem was to implement the "accelerated super-basin kinetic Monte Carlo" (AS-KMC) algorithm [**195**]. The AS-KMC method adds the extra algorithmic step of checking whether any of the events that are part of a "super-basin" have been executed a pre-specified number of times. For such events, the AS-KMC increases the barrier height, thereby lowering their rate of occurrence. In conventional terms, a super-basin consists of clusters which are linked to each other by high-frequency events but are separated from the surrounding energy landscape by one or more high barriers, making the frequency of the escape from the basin dramatically lower. AS-KMC avoids getting stuck in a single super basin by boosting the probability of the system overcoming these high barriers. In our implementation, as the clusters are independent from each other, a superbasin is the set of fast transitions over the low energy sector of the barrier distribution for each cluster. The AS-KMC method increasing the barrier height in the low energy sector can be thought of as integrating out the fast degrees of freedoms in a renormalization group sense, thereby mapping the problem to a scaled problem where the slower transitions over the higher energy barriers are the typical processes. The formalism of our implementation of the AS-KMC method is as follows. Every N times that an event occurs, the transition rate Γ of that event is reduced by a factor α, such that $\Gamma' = \Gamma/\alpha$. Here α is taken as:

$$\alpha = 1 + (\mathrm{N}\,\delta)/|\ln(\delta)|. \tag{7.8}$$

where δ is the magnitude of the relative error in the new probability of escaping the superbasin once the internal activation barrier has been raised. We chose $N = 10$ and $\delta = 0.25$. As is clear from the above description of the KMC method of forwarding the time at each executed transition by the inverse of the executed rate, the scaling of the Γ rates scales the time itself. The integrating out of

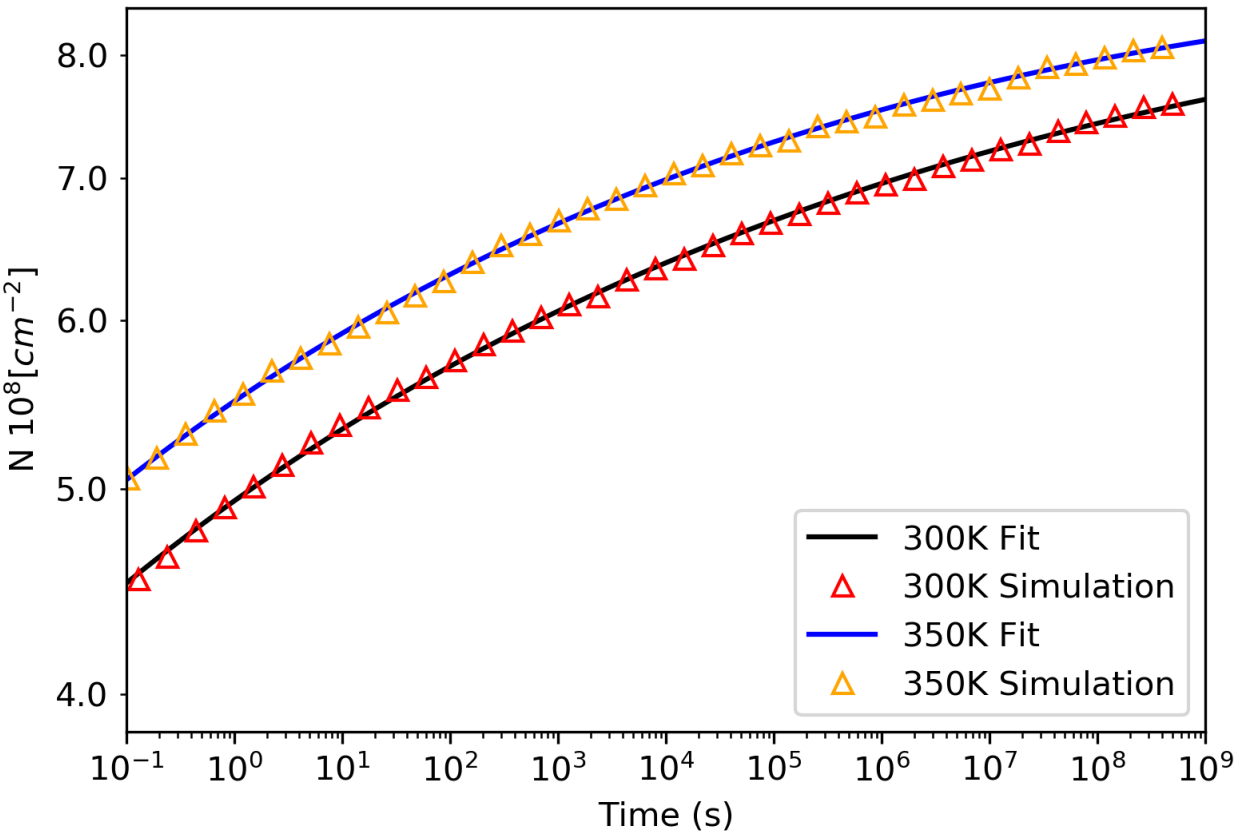

FIGURE 7.5. Defect density N(t) as a function of time. Defect saturation density was chosen as $N_{sat} = 1x10^9$ cm^{-2}. Orange: defect generation by AS-KMC at T=300K. Red: accelerated defect generation by AS-KMC at T=350K. Blue and green: Stretched exponential fits to AS-KMC results with stretching exponent $\beta(300\text{K}) = 0.019$, and $\beta(350\text{K}) = 0.022$.

the fast degrees of freedom and the rescaling of time together map the model to a "slower transitions only" model. As this integrating out and rescaling is repeated many times over, transitions over all time scales are properly accounted for by this AS-KMC method.

We reduced the noise by simulating the AS-KMC dynamics for 64 samples of 20,000 clusters each, and finally by averaging the results. Fig. 7.5 shows the time dependent defect density $N(t)$, determined by this method. The minimal fluctuations of $N(t)$ are representative of the effective error bars and thus show that the above approach averaged out the fluctuations very efficiently. The AS-KMC dynamics was performed for samples with temperature at T=300K (red), and T=350K (orange), in order to simulate defect generation at ambient temperatures and with standard accelerated testing protocols at elevated temperatures, as described below in detail.

In order to develop an analytic model and understanding for these simulation results, we recall that systems that exhibit very slow dynamics are often thought of as glassy systems with a broad distribution of energy barriers $P(E)$ [**196**]. In general, the distribution of energy barriers $P(E)$ can be translated into a distribution of "barrier crossing times" $P(\tau)$, and then coupled rate equations can be written down for defect creation and defect annihilation. The expectation value of cluster transition rates at time t can be determined by integrating over the barrier crossing time distribution $P(\tau)$ up to t which turns out to be time dependent instead of the usual constant rates, typical for well defined transition energies. [**197**, **198**] This rate equation for the defect density with time dependent rates can then be solved for $N(t)$.

The specific time dependence of $N(t)$ depends on the functional form of the energy barrier distribution $P(E)$. As seen in Fig. 7.4, our $P(E)$ distributions can be well-fitted with an exponential, $P(E) = (1/E^*)\exp(-E/E^*)$, with $E^* = 1.42$ eV for barrier creation and $E^* = 1.44$ eV for barrier annihilation. Following the above steps for an exponential energy barrier distribution yields a stretched exponential time dependence [**197**, **199**, **200**]:

$$N(t) = N_{sat}\left(1 - \exp\Big\{\Big[-(t/\tau_0)^{\beta}\Big]\Big\}\right), \tag{7.9}$$

where $\beta = k_B T/E^*$, and τ_0 is a short time cutoff. It is important to emphasize that here β was not a fitting parameter. Once we determined E^* from the $P(E)$ we computed earlier (Figs. 7.4a-b), this fixed the value of β. β being fixed makes it all the more remarkable that we were able to fit $N(t, 300\text{K})$ *over ten orders of magnitude* with $\beta(300\text{K}) = 0.019 = k_B * 300\text{K}/E^*$ since $E^* = 1.43$ eV, the average of the defect creation and defect annihilation energy scales; and analogously, fit $N(t, 350\text{K})$ with $\beta(350\text{K}) = 0.022$.

For completeness we note that we obtained very good fits setting τ_0 with $1/\Gamma_0$, but our fits improved by using shorter τ_0 cutoff values. Developing a physical interpretation for the best τ_0 is left for a later paper. Further, forcing power law or near-flat fits on $P(E)$ predicted power law and logarithmic time dependencies. Such forms can achieve reasonable fits for $N(t)$ over 2-4 orders of magnitude in time, but as the fitting range was extended, the stretched exponential fit produced the singularly best fit, and thus we conclude that the exponential for for $P(E)$ is the natural choice.

A stretched exponential time dependence was reported for the recombination lifetime at a-Si:H/c-Si interfaces [**201**] before, as well as related aging phenomena [**196**]. The measurement "annealing" temperature was T=450K, and the β exponent assumed values in the 0.29-0.71 range. Accordingly, the characteristic energy scale E^* of the barrier distribution that controlled this time dependence was in the range of $E^* = 50 - 125$ meV, an order of magnitude smaller than the Si defect energies that control the time evolution in this paper. We agree with the conclusion of the authors of Ref. **201**: their time dependence was probably controlled by hydrogen diffusion. Hydrogen was not considered in our model.

The main messages of Figs. 7.4a-b and Fig. 7.5 are as follows.

(1) It has been customary to think about degradation processes in Si solar cells as being controlled by chemical bonds with well-defined energies, at most with a narrow distribution. But our simulations of realistic a-Si/c-Si stack interfaces show that the bond energies of a large fraction of the Si atoms, especially those close to the interface, are weakened by stretching and twisting, many to the point of being broken. Therefore, the defect generation is controlled by a broad distribution of energy barriers instead of a narrow one. One is led to the conclusion that the solar cell degradation needs to be described in terms of such wide energy barrier distributions.

(2) We developed the SolDeg platform to answer the above need. SolDeg is capable of connecting the fast atomic motions that control defect structures and play out on the femtosecond time scale, with the slow, glassy transitions controlled by the wide distribution of energy barriers that take place over time scales up to gigaseconds, the order of 20 years. The ability of the SolDeg platform to bridge these 24 orders of magnitude in time makes it a uniquely powerful tool for a comprehensive study of defect generation in a-Si/c-Si stacks.

(3) We have shown that a simple, stretched exponential analytical form can successfully describe defect generation over an unparalleled range of ten orders of magnitude in time. This analytical form may turn out to be quite useful for the analysis of experimental degradation studies.

(4) As far as numerical values are concerned, the defect generation rate in the first month (starting from 10^5 seconds, about one day) is $\approx 1.5\%$/month that slows to 4%/year for the first year. This defect generation rate will be used to connect our theoretical work to experimental data as follows. The published NREL measurements capture degradation of fielded HJ a-Si/c-Si solar

cells in terms of V_{oc}, the open circuit voltage, with the result of 0.5%/year in relative terms [**59**]. The well-known relation connecting V_{oc} to the defect density reads:

$$V_{\mathrm{oc}} = \frac{kT}{q} \ln\left(\frac{J_L}{J_0}\right), \tag{7.10}$$

here J_0 is the dark saturation current, proportional to the defect density $N(t)$, and J_L is the light current. One expects that the primary driver of the performance degradation is the defect density, $N(t)$, thus, we can capture the degradation in natural, relative terms as

$$\frac{1}{V_{\mathrm{oc}}} \frac{dV_{\mathrm{oc}}}{dt} = \frac{-1}{\ln(J_L/J_0)} \frac{1}{N} \frac{dN}{dt}. \tag{7.11}$$

Using relevant values for J_L and J_0 reveals that $ln(\frac{J_L}{J_0})$ is realistically around 20, thus the 4%/year relative defect density growth rate gives a relative degradation rate for V_{oc} of about 0.2%/year. On one hand, it is a reassuring validation of the quantitative reliability of the SolDeg platform that our V_{oc} degradation rate came out to be comparable to the 0.5%/year change observed in fielded HJ modules [**59**]. On the other hand, the fact that our calculated degradation rate is notably lower than the observed value is consistent with the physical expectation that in commercial HJ cells the silicon is hydrogenated, and hydrogen migration is expected to be a primary driver of the defect generation. Further, exposure to illumination also enhances defect generation. The fact that our work has not included hydrogen or illumination yet comfortably accounts for the computed degradation rate being lower than the observed one. Finally, it is noted that while some published experiments report the above steady degradation rate of 0.5%/year over 7 years [**59**], other, shorter time studies report a strongly slowing degradation [**201**]. Our results are consistent with the latter, and thus we think that comparison with experiments should be done in terms of a full time dependence of $N(t)$ or V_{oc}. At any rate, the natural next step for the development of the SolDeg platform is to include hydrogen and illumination. This demanding work is already ongoing and will be reported soon.

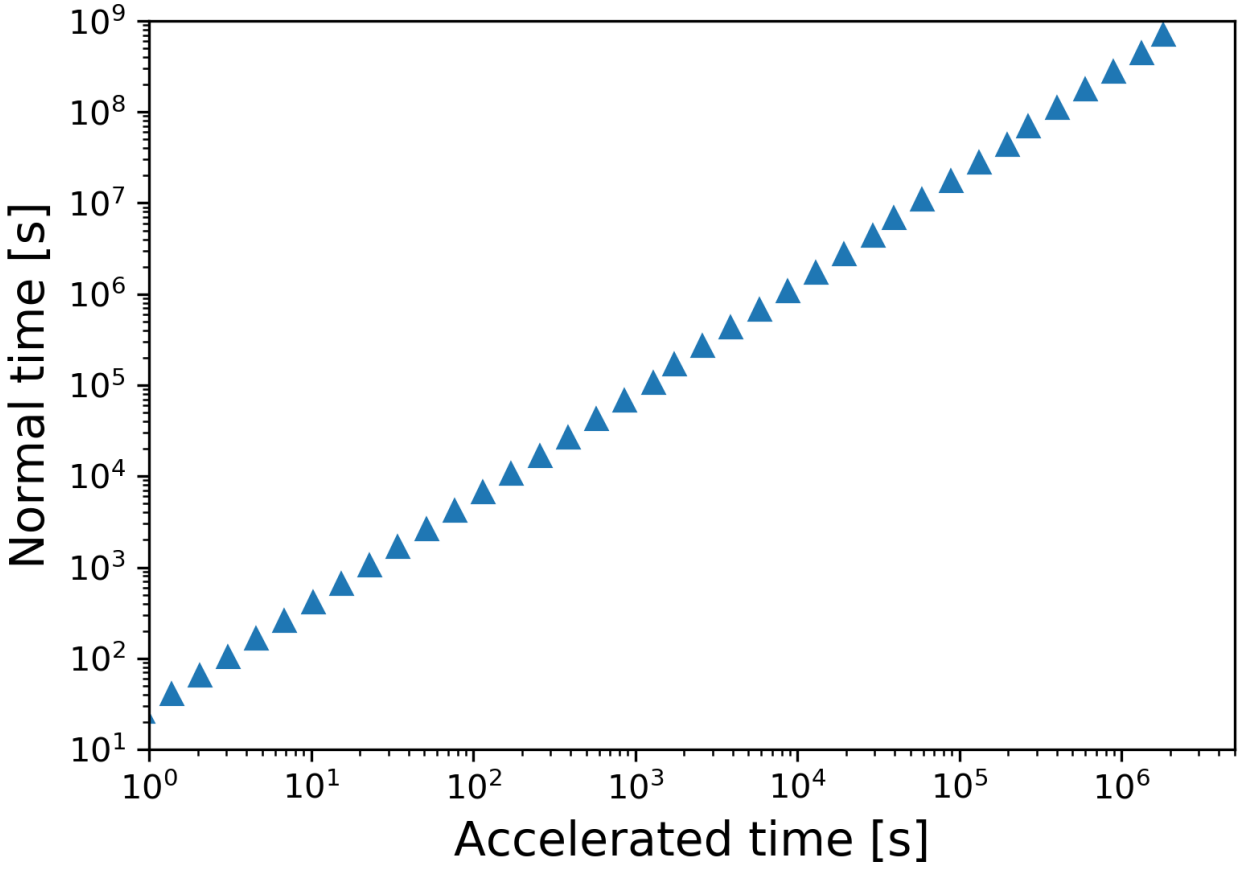

FIGURE 7.6. Time Correspondence Curve, translating accelerated degradation time to degradation time at standard temperature.

(5) The power of SolDeg can be further demonstrated by developing a quantitative guide to calibrate the widely used accelerated testing protocols of solar cells. Fig. 7.5 also shows the accelerated growth of the defect density in a HJ stack at the elevated temperature of T=350K. The two simulations were started with the same defect density at t=0: $N(T$=300K, t=0)=$N(T$=350K, t=0). Visibly, the T=300K and T=350K curves largely track each other: the difference is that $N(T$=350K, $t)$ reaches the same defect densities as $N(T$=300K, $t)$ at shorter times. This is why week-long accelerated testing can capture year-long defect generation under ambient/fielded conditions.

To turn this general observation into a quantitatively useful calibration tool, we created the Time Correspondence Curve (TCC). The TCC connects the times of accelerated testing with those times of normal, ambient degradation that produce the same defect density. In formula:

TCC plots the $t_{\text{accelerated}}$ – t_{normal} pairs for which $N(T{=}350\text{K}, t_{\text{accelerated}}) = N(T{=}300\text{K}, t_{\text{normal}})$. Fig. 7.6 shows the resulting TCC. For example, the TCC shows that $t_{\text{accelerated}}{=}10^6$ seconds of accelerated testing approximately generates the same density of defects as $t_{\text{normal}}{=}10^8$ seconds or normal degradation. In general, the TCC was created by taking horizontal slices across the two curves of Fig. 7.5 to find the corresponding pairs of times that generated the same defect density.

Even a cursory observation reveals that the TCC grows linearly on the log-log plot, i.e. as a power law over an extended, experimentally relevant time period:

$$t_{\text{accelerated}} \propto t_{\text{normal}}^{\nu} \tag{7.12}$$

where $\nu = 0.85 \pm 0.05$, an unexpected scaling relation with an unexpected precision. Just like in Fig. 7.5, this scaling relation is observed over the most remarkable ten orders of magnitude in time. Establishing such simple and practical correspondence relations can be a very helpful product of the SolDeg platform that can be widely used for calibrating accelerated testing protocols. Remarkably, the above-developed description in terms of an exponential $P(E)$ that led to an stretched exponential $N(t)$ that explained the results over ten orders of magnitude, also gives a straightforward explanation for this scaling relation. Direct observation of the stretched exponential formula reveals that $N(T{=}350\text{K}, t_{\text{normal}}^{300/350}) = N(T{=}300\text{K}, t_{\text{normal}})$, i.e. the stretched exponential form not only explains the existence of the scaling form of TCC, but makes a prediction for ν:

$$\nu = T_{\text{normal}}/T_{\text{accelerated}} = 300/350 = 0.85, \tag{7.13}$$

which is exactly the exponent what the direct analysis of the TCC determined. These considerations provide a remarkably self-consistent and powerful tool set to analyze degradation processes.

7.3. Experimental Studies of Degradation of a-Si:H/c-Si stacks

In this section, we explore the correspondence between our simulations and experiments on a-Si:H/c-Si heterojunction structures. Fig. 7.7(a) shows that for the interface defect density, a wide range of values have been reported in the literature [**202**, **203**, **204**, **205**]. This unusually wide

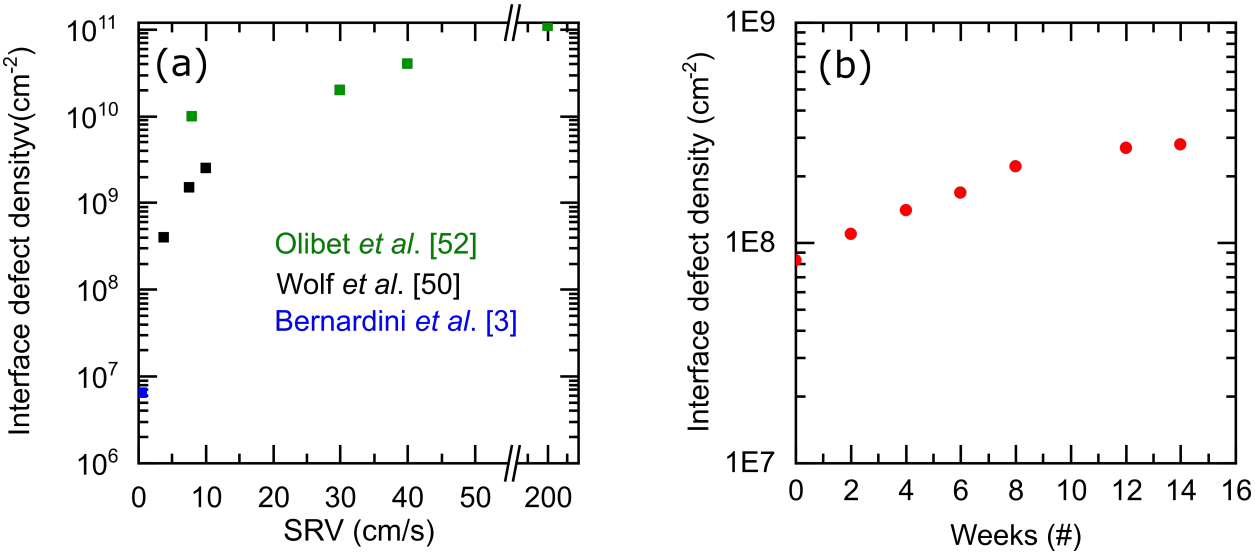

FIGURE 7.7. (a) Interface defect density and effective surface recombination velocity data reported in the literature for a-Si:H/c-Si interface at the time of deposition or after annealing. (b) Interface defect density measured in our a-Si:H/c-Si stacks, stored in the dark under standard ambient condition.

range is caused by many different factors, such as the different methods and protocols employed for depositing a-Si, the level of cleanliness of c-Si wafer before deposition, substrate morphology, orientation of c-Si, microstructure of the a-Si film, hydrogen content, bonding in a-Si, and storing conditions of samples [**206**,**207**,**208**,**209**]. However, there are not many studies available correlating the impact of such differences to long-term stability of a-Si/c-Si interface. For completeness, in Fig. 7.7(a) we also summarize the corresponding surface recombination velocities (SRV) from the cited papers. Disappointingly, very few of these papers have analyzed the time dependence of the interface defect density and that of the SRV. Therefore, it is difficult to draw lessons from these papers for the long term performance degradation of heterojunction structures.

Driven by these considerations, we have set out to fabricate our own a-Si:H/c-Si heterojunction structures to measure the long time evolution of the defect density and SRV. In order to experimentally isolate the processes associated with the time evolution of interface defect density and SRV from the processes occurring in other layers, and to be able to access these quantities with direct measurements, we created test structures that were simpler than Si HJ solar cells. This is to

isolate the changes happening at the interface and in the film over time from the influence of other layers present in the cell.

These simpler structures, or stacks, were comprised of c-Si of varying thickness (160–260 μm), passivated on both sides with hydrogenated intrinsic a-Si (a-Si:H(i)). We used double-side polished float zone (FZ) quality n-type c-Si wafers with (100) crystal orientation, 2.5 Ωcm resistivity and initial thickness of ∼275 μm. These wafers went through rigorous surface cleaning before deposition of 50 nm of a-Si:H(i) on both sides. Complete details about cleaning protocol and deposition conditions are found in [**210**]. After deposition, these samples were annealed at 280 °C for 30 mins in air in a muffle furnace. Then we measured injection-dependent effective minority carrier lifetime (τ_{eff}) on these samples at temperatures between 30 and 230 °C using the WCT-120TS tool from Sinton Instruments. Data was collected in transient mode due to the long lifetime of the samples. We performed linear fits for $1/\tau_{eff}$ vs $1/W$ data at each injection level to obtain temperature- and injection-dependent SRVs from their slopes. Here W is thickness of the c-Si. As a final step we extracted the interface defect density by fitting the amphoteric defect model proposed by Olibet *et al.* to the SRV *vs* temperature data at different injection levels. The input parameters, along with their best-fit values to the model, were the interface charge density ($Q = -1.3 \times 10^{11}\,\mathrm{cm}^{-2}$), the neutral electron-to-hole capture cross-section ratio ($\frac{\sigma_n^o}{\sigma_p^0} = \frac{1}{20}$), and the charged-to-neutral capture cross-section ratio ($\frac{\sigma_n^+}{\sigma_n^o} = \frac{\sigma_p^-}{\sigma_p^o} = 500$) with $\sigma_p^o = 10^{-16}\,\mathrm{cm}^{-2}$.

The resulting interface defect density values over time for the samples stored in dark and ambient conditions are shown in Fig. 7.7(b). We found that the magnitude of the fitted interface charge density remained the same over time, indicating no change in field effect passivation [**201**]. However, the interface defect density increased with time at the rate of $dN/dt = 5.6 \times 10^7 \mathrm{cm}^{-2}$/month. This translates to a rate of increase of $(1/N)\ dN/dt = 68\%$/month in relative terms for the first 3.5 months. Similar results have been reported previously by Bernardini et al., where the defect density increased from $(6.5 \pm 0.5) \times 10^5 \mathrm{cm}^{-2}$ to $(5.5 \pm 1.5) \times 10^7 \mathrm{cm}^{-2}$ over a period of 28 months for samples stored in dark, ambient conditions [**61**]. This translates to a rate of 17%/month in relative terms. While our study found a higher rate in the initial 3.5 months, we expect the defect generation rate to slow down considerably as time progresses, and converge to the results of Ref. [**61**]. The fact that the defect generation slows down was clearly established by our simulations as well, as shown

in Fig. 7.5, where we found that the rate of change in the early months is about 1.5%/month, slowing to an overall rate of 4%/year for the first year.

To make connection to previous results, we fitted our experimental data with a stretched exponential. Holovsky. et al. reported such fits with stretching exponent β in the 0.3-0.7 range, depending on deposition temperatures [**201**]. Our data are consistent with the stretching exponent in this range. However, the relatively limited temporal range of the data does not conclusively exclude β values outside this range either. We continue taking data that will narrow the range of the stretching exponent.

We note that the initial defect density in our samples was lower than those reported for as-deposited films in Fig. 7.7(a) by at least an order of magnitude. This could be due to the difference of the deposited a-Si:H film in terms of the crystallinity, hydrogen content, hydrogen bonding configuration and void fraction [**211**]. Whatever the reason may be, the notably low defect density is a compelling indicator for the high quality of our a-Si deposition protocol.

It is noted, of course, that the degradation rate observed in our test structures shown in Fig. 7.7(b) is not expected to directly correspond to the degradation rate observed in complete Si HJ cells. This is due to the additional layers present in Si HJ cells on top of a-Si:H(i) which may efficiently suppress the migration of hydrogen away from the a-Si:H/c-Si interface, as well as prevent oxidation of the a-Si:H(i) layer.

7.4. Conclusions

In this paper we reported the development of the SolDeg platform for the study of heterojunction solar cell degradation. SolDeg layers several techniques on top of each other, in order to determine the dynamics of electronic defect generation on very long time scales. The first layer of SolDeg was to adapt LAMMPS Molecular Dynamics simulations to create a-Si/c-Si stacks. Our simulations used femtosecond time-steps. For the interatomic potential, we used the machine-learning-based Gaussian approximation potential (GAP). Next, we optimized these stacks with density functional theory calculations. In SolDeg's next layer we created about 1,500 shocked clusters in the stacks by cluster blasting. We then analyzed the just-generated shocked clusters by the inverse participation ratio (IPR) method to conclude that cluster blasting generated electronic defects in about 500 of the

1,500 shocked clusters. Next, we adapted the nudged elastic band (NEB) method to determine the energy barriers that control the creation and annihilation of these electronic defects. We performed the NEB method for about 500 shocked clusters on our way to determine the distribution of these energy barriers. A simple exponential form gave a good fit for $P(E)$. Finally, we developed an accelerated super-basin kinetic Monte Carlo (AS-KMC) approach to determine the time dependence of the electronic defect generation, as controlled by the broad energy barrier distribution.

Our main conclusions were as follows. (1) The degradation of a-Si/c-Si heterojunction solar cells via defect generation is controlled by a very broad distribution of energy barriers, extending from the scale of meV to 4 eV. (2) We developed the SolDeg platform that can track the microscopic dynamics of defect generation $N(t)$ from femtoseconds to gigaseconds, over 24 orders of magnitude in time. This makes SolDeg a uniquely powerful tool for a comprehensive study of defect generation in a-Si/c-Si stacks and solar cells. (3) We have shown that a simple, stretched exponential analytical form can successfully describe the defect generation $N(t)$ over ten orders of magnitude in time. (4) We found that in relative terms $V_{\rm oc}$ degrades at a rate of 0.2%/year over the first year. It is a reassuring validation of the quantitative reliability of the SolDeg platform that our V_{oc} degradation rate came out to be comparable to the 0.5%/year change observed in fielded HJ modules [**59**]. The difference is most likely attributable to the SolDeg platform not yet including hydrogen and illumination. The project to include both has already started and will be reported in a later publication. (5) Further, we developed the Time Correspondence Curve to calibrate and validate accelerated testing of solar cells. This TCC connects the times of accelerated testing with those times of normal, fielded degradation that produce the same defect density. Intriguingly, we found a compellingly simple scaling relationship between accelerated and normal times $t(\text{accelerated}) \propto t(\text{normal})^{0.85}$, which can be used to calibrate accelerated testing protocols, making it a more quantitative assessment tool. (6) We ourselves also carried out experimental work on defect generation in a-Si/c-Si HJ stacks. We found that the degradation rate was high on the short, initial time scales, but slowed considerably at longer time scales. A possible explanation is that our samples had unusually low initial defect densities, in which case hydrogen diffusion may generate defects more efficiently.

The next chapter will discuss the development of a Si-H interatomic potential to continue this project by incorporating hydrogen into the SolDeg platform, and determine the dynamics of the

defect generation anew. We will follow this by validating and calibrating the improved SolDeg platform by a rigorous comparison to our experimental data. Once the driving forces of defect generation and degradation are reliably captured and characterized by the SolDeg platform and by our experiments, we plan to develop strategies to mitigate these degradation processes.

CHAPTER 8

Training a Machine-Learning Driven Gaussian Approximation Potential for Si-H Interactions

8.1. Motivation

One of the primary tools for materials modeling is the use of atomistic simulation methods. The most accurate of these methods are those based in electronic-structure theory, such as density functional theory (DFT), which are highly accurate at the cost of significant computational expense and unfavorable scaling behavior. Simulations of more than a few hundred atoms, or with millions of energy or force evaluations, instead are conducted using parameterized empirical interatomic potentials. The potentials are typically quite simple in their formulation, and are usually optimized to yield high levels of accuracy in reproducing a few carefully chosen observables on a particular subset of structures. The limitations of the functional forms of these potentials necessitate that a balance be struck between maximizing the accuracy for selected properties deemed the most crucial, and transferability in measuring other observables or simulating structures which the potential was not fitted to.

The imperfectness of these solutions, presenting a constant trade-off between accuracy or speed, has motivated the adoption of machine-learning (ML) methods to fit functions with non-parametric forms to DFT measured microscopic quantities. The goal of these methods is to create interatomic potentials with DFT levels of accuracy over a wide range of structures and observables, while maintaining a factor of 10x or more improvement over DFT capabilities in both simulation speed and number of simulation atoms. The functional forms of these potentials are highly flexible, due to their non-parametric nature, and can be fit to a wide range of structures.

The well-known limitation of ML models is that they are limited in their transferability. The flexibility of their functional form enables the use of a broad training database, which can encompass a wide variety of structures, and highly accurate interpolation between the constituent structures.

However, the nature of this flexibility means that the ML model will be highly accurate for the structures within the training database, a good fit for structures near the database, and increasingly less accurate the farther away from the training database a structure lies. Training a truly "general-purpose" potential thus requires a very large database size, and even then is not wholly transferable to situations which it has never encountered.

This problem of extrapolation is what motivated the development of the Gaussian approximation potential (GAP) framework. In previous GAP publications, it has been shown that the combination of a kernel-based fit which nimbly adapts to previously un-encountered simulation environments, and using an adaptive training database, does an excellent job in making up for these shortcomings [**176**, **177**, **178**]. Here, the term "adaptive training database" refers to, in an iterative process over time, growing the training database from the GAP learns. In this process, the GAP is fitted to an initial training set, and then is used to perform calculations such as structure optimizations or basic MD simulations. The results of these calculations are then validated against DFT calculations, and any ill-fitting results, corresponding to structures not contained in the interpolative structure space of the training set, are added to the training database. The progress of the potential is measured by computing the error (relative to DFT) of GAP measurements of energies, forces and virial stresses on a separate reference database. This process can be repeated as many times as necessary to yield satisfactory levels of accuracy, either on macroscopic observables or on the aforementioned microscopic quantities. This method has the advantage of only growing the training database in areas where the ML model fits poorly, rather than blindly training the model on a vast number of reference structures.

8.2. Technical Details

In this work we train our ML model by fitting a Gaussian approximation potential (GAP) using a SOAP (Smooth Overlap of Atomic Positions) kernel with a core predefined pair potential. This pair potential is chosen to be purely repulsive, and is given by cubic splines that are fitted to the interaction of pairs of atoms in vacuum as computed by DFT. Pair potentials are given for all 3 relevant atomic pairs: Si-Si, Si-H, and H-H. Including these core repulsive pair potentials serves a dual purpose. First, much of the interaction energy between atoms can be described by a simple

pair potential, which describes exchange repulsion at close atomic approach, and some effects of chemical bonding at further distances. Second, this exchange repulsion piece of the potential is difficult to capture with kernel fitting in high dimensions due to the steepness of the energy curve in that region, and thus capturing it with a core potential enhances numerical efficiency.

The total GAP energy for the system is thus a sum of the predefined repulsive pair potential and the many-body term which is given by the linear sum over the kernel basis functions:

$$E = \sum_{i<j} V^{(2)}(r_{ij}) + \sum_{i} \sum_{s}^{M} \alpha_s K(R_i, R_s) \tag{8.1}$$

where i and j range over the number of atoms in the system, $V^{(2)}$ is the 2-body repulsive pair potential, r_{ij} is the distance between atoms i and j, K is the SOAP kernel basis function, and R_i is the collection of relative position vectors corresponding to the neighbors of atom i which is termed a *neighborhood*. The final sum ranges over the set of M *representative* atoms, selected from the input data set, whose environments are chosen to serve as a basis in which the potential is expanded. The coefficients α_s are determined by solving a linear system that is obtained when available data are substituted into the equation. These data are the total energies and gradients (forces and stresses) of the system, calculated by density-functional theory (DFT). The representative environments over which Eq. 1 is taken are selected by choosing basis environments which are maximally dissimilar to each other, such that the variety of the entire set of possible environments is well represented by interpolation over a small number of basis environments.

The kernel value determines the similarity between two neighborhoods, which is largest when the two neighborhoods are identical, and smallest when the two neighborhoods are maximally different. To compare the two neighborhoods, the neighborhood R_i of atom i is represented by it's neighbor density:

$$\rho_i(\mathbf{r}) = \sum_{i'} f_{\text{cut}}(r_{ii'}) e^{-(\mathbf{r}-\mathbf{r}_{ii'})/2\sigma^2_{\text{atom}}} \tag{8.2}$$

These neighbor densities are not calculated directly, but are instead represented by an expansion in a basis of spherical harmonics and radial functions.

The SOAP kernel used here to compare two neighborhoods is calculated from the integrated overlap of the neighbor densities:

$$\tilde{K}(R_i, R_j) = \int_{\hat{R}\in \mathrm{SO}(3)} d\hat{R} \left| \int d\mathbf{r} \rho_i(\mathbf{r}) \rho_j(\hat{R}\mathbf{r}) \right|^2 \tag{8.3}$$

The final kernel is calculated by normalizing $\tilde{K}$ and raising it to an integer power:

$$K(R_i, R_j) = \delta^2 \left| \frac{\tilde{K}(R_i, R_j)}{\sqrt{\tilde{K}(R_i, R_i)\tilde{K}(R_j, R_j)}} \right|^\zeta \tag{8.4}$$

For further details of the GAP methodology, refer to Ref. **176**.

8.3. Fitting a GAP to Si-H

8.3.1. Training and Reference structures. When training ML models, it is important to have two sets of structures which the ML model sees. One of these is the adaptive training set, the set of structures, iteratively growing over time, to which the GAP is fitted. The other is the reference set, a set of structures which is used for evaluation purposes. The ML model is never trained on this set of structures, but it does make comparative measurements against DFT, the accuracy of which is used to measure the progress of the potential.

The base training and reference structure sets were assembled by adding H to pure Si structures of various phases. Approximately 150 structures are contained in the initial training set, and approximately 110 structures are contained in the reference set. These pure Si structures were taken both from the previous chapter on a-Si/c-Si interface degradation, as well as from the reference database on which the published Si-only GAP was trained [**176**]. The representative phases of Si were: 1) Amorphous Silicon; 2) Liquid Silicon; 3) Diamond Silicon with a vacancy; 4) Diamond Silicon with a divacancy; 5) Diamond Silicon with an interstitial Si; 6) Amorphous/Crystalline Silicon interface structures. The atomic concentration of H added was between 6 and 12 at.% for the liquid and amorphous phases. and between 4 and 8 at. % for the diamond phases, as sufficient H was added to passivate all dangling or strained bonds. Since we specifically want to model

hydrogen-related defects, structures with plus or minus an additional H atom were also added into both the training database and reference database.

It should be noted that the training set also contains a single structure with an isolated Si atom, and a single structure with an isolated H atom. Isolated here means the structure possesses a large enough unit cell that the atom is effectively in isolation. Including these isolated atomic structures is essential because the potential is fit to the binding energy, not the total energy (i.e. the binding energy plus the energy of isolated atoms). As such, it is necessary to properly account for the individual atomic energies when fitting the potential.

8.3.2. DFT Calculations. DFT was used to calculate the total energy, forces on each atom, and the virial stress of each of the atomic structures contained in the training set. These 3 pieces of information are what the GAP is fitted to structure-by-structure.

The DFT calculations were performed using the Quantum Espresso 6.2.1 software package [**183**, **184**, **212**]. The main parameters of the electronic-structure calculations we performed are as follows: the Perdew-Burke-Ernzerhof (PBE) exchange-correlation functional was used with periodic boundary conditions [**185**]. The core and valence electron interactions were described by the Norm-Conserving Pseudopotential function. The calculations were performed with Marzari-Vanderbilt electronic smearing [**213**]. This smearing method was chosen as it ensures that the DFT energies and forces are consistent. An energy cutoff of 42 Ry was employed for the plane-wave basis set, and a Monkhorst-Pack grid method was used to define the k-point mesh which samples the Brillouin-Zone. The k-point spacing was chosen to be $.2\text{Å}^{-1}$.

Care was taken to ensure that the energy/atom calculated for each structure was accurate to within 1 meV/atom. That is, ± 1 meV/atom of the value that would emerge from calculations with an exceptionally large cutoff energy and k-point density.

The PWSCF module of Quantum Espresso software was employed to perform DFT Born– Oppenheimer molecular dynamics (DFT-BOMD) simulations. The self-consistent Hellmann-Feynman theorem was used in order to calculate the interatomic forces at the electronic ground state at each time step. The same exchange-correlation functional as the single point DFT calculations was used. An energy cutoff of 36 Ry was used for the plane-wave basis set, and the first Brillouin zone was

Element	$n_{\max}$	$l_{\max}$	δ	ζ	r_{cut}	w	σ_{atom}
Si	10	6	3	4	5.0	1.0	0.5
H	9	6	1	4	3.5	0.5	0.4

TABLE 8.1. Table of SOAP kernel parameter values, for each atomic type

Phase	σ_{energy} [eV/atom]
Amorphous Silicon	0.005
Liquid Silicon	0.0015
a-Si/c-Si Interface	0.005
Diamond Si Phases	0.001
Isolated Atom	0.0001

TABLE 8.2. Table of σ_{energy} values for each structure type.

sampled using only the Γ point. A Gaussian smearing width of 0.01 Ry to the density of states was implemented to avoid convergence problems with metallic configurations.

8.3.3. GAP Fitting. As described in the technical details, we used a SOAP (Smooth Overlap of Atomic Positions) kernel in combination with a repulsive pair potential to fit our GAP. Two SOAP kernels were used, one for the Si atoms, and one for the H atoms. Several input parameters are needed for each SOAP kernel. These include: 1) $n_{\max}$ and $l_{\max}$, the maximum number of radial and angular indices for the spherical harmonic expansion of the neighbor densities; 2) δ, a hyperparameter which corresponds to the energy scale of the many-body term in the SOAP kernel; 3) ζ, the integer power to which the SOAP kernel is raised; 4) the cutoff radius r_{cut} and an associated transition width w, characterizing the point beyond which, and how fast, the cutoff function smoothly goes to zero in the calculation of the neighbor densities; 5) σ_{atom}, the smearing parameter for the neighbor density function. For the values of these parameters used, see Table 8.1.

Also important to the fitting are the chosen regularization parameters, σ. These parameters represent the desired accuracy of the potential in fitting to the data, and correspondingly also determine the relative weight of each structure in the fitting procedure. Separate σ values are assigned for the energies (σ_{energy}), forces (σ_{force}), and virial stresses (σ_{virial}). It is possible to input these σ values to the potential in a number of different ways, including as single values for all

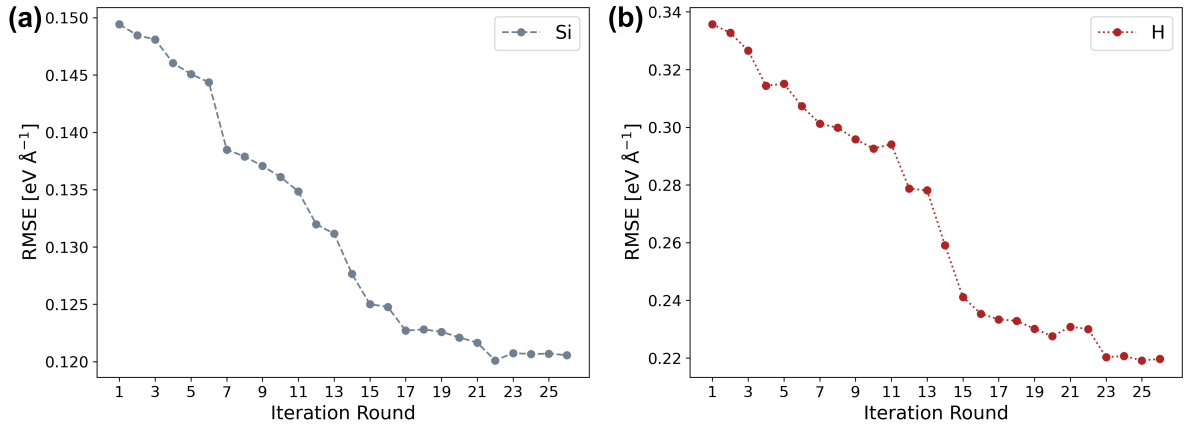

FIGURE 8.1. Iterative progression of the average of the RMSE of the (a) Si and (b) H cartesian force components, measured with respect to DFT on the reference structure set.

structures, or on a "structure type" basis, assigning single values to all structures in a single phase (for instance, liquid Si). Our approach was slightly different than these methods: we instead chose to assign the σ values on a structure-by-structure basis. The σ_{energy} values were chosen to be the same for all structures in a given phase, see Table 8.2 for these values. σ_{force} was assigned on a per-atom basis as:

$$\sigma_{\text{force}} = \begin{cases} 0.1 & ,|F| < 2.0\,\text{eVÅ}^{-1} \\ 0.05|F| & ,|F| \geq 2.0\,\text{eVÅ}^{-1} \end{cases}, \tag{8.5}$$

where $|F|$ is the magnitude of the force vector on that respective atom. σ_{virial} was assigned on a per-structure basis as:

$$\sigma_{\text{virial}} = \begin{cases} 0.025 N_{\text{atoms}} & ,\max\left(|\tau_i|\right) < 1.0\,\text{eV} \\ 0.025 N_{\text{atoms}} * \max\left(|\tau_i|\right) & ,\max\left(|\tau_i|\right) \geq 1.0\,\text{eV} \end{cases} \tag{8.6}$$

where N_{atoms} is the number of atoms in the structure, and $\max\left(|\tau_i|\right)$ is the max norm of the virial stress tensor.

8.3.4. Iterative Training. As described in the motivation section above, the conventional wisdom is that a ML model needs to be trained on a broad database of structures, containing as many structures as possible, in order to be usable in a general sense. To mitigate this, we have

adopted an adaptive training procedure, wherein the potential is used to conduct MD simulations on the structures already contained in the training database, and the results of these simulations are validated against DFT measurements of energies, forces, and virial stresses. Ill-fitting results are then added to the training database, thus growing the training database in an iterative manner. Using this procedure, it is not necessary to add thousands of structures, as the potential will

Iteration	Structure Type
1	Optimized structures (all phases)
2	Optimized structures (all phases)
3	Low T anneal of a-Si:H
4	High T anneal of liq-Si:H
5	High T anneal of liq-Si:H
6	Med T anneal (1100K) of a-Si:H
7	Heating a-Si:H from 500K to 800K at 10^{13} K/s
8	Heating a-Si:H from 800K to 1100K at 10^{13} K/s
9	Heating a-Si:H from 1100K to 1400K at 10^{13} K/s
10	Heating a-Si:H from 1100K to 1400K at 10^{13} K/s
11	Heating a-Si:H from 800K to 1400K at 10^{12} K/s
12	Added new a-Si:H structures
13	Add new a-Si:H structures
14	Added c-Si/a-Si:H interface structures
15	Added c-Si/a-Si:H interface structures
16	Added new c-Si divacancy structures
17	Added new liq-Si:H structures
18	Added new c-Si vacancy structures
19	Added new c-Si interstitial structures
20	Low T anneal of c-Si/a-Si:H interface structures
21	Optimization of c-Si/a-Si:H interface structures
22	NPT high T anneal of liq-Si:H structures
23	NVT high T anneal of liq-Si:H structures
24	Quenching liq-Si:H from 2000K to 1500K at 10^{13} K/s
25	Annealing quenched liq-Si:H structures at 1500K
26	Quenching liq-Si:H from 1500K to 1400K at 10^{12} K/s

TABLE 8.3. Structure types added each iteration.

naturally gravitate towards regions of configuration space where it is ill-fitting on its own, without any external input or danger of over-fitting.

All MD simulations were performed using the LAMMPS software package built with QUIP package support [**179**, **214**, **215**].

The error metric used to evaluate the accuracy of the GAP compared to DFT is the weighted root mean square error (RMSE). As the desired accuracy of the GAP varies from structure to structure, as determined by the Σ values, the RMSE itself loses some meaning, as structures with a high RMSE value may also have a high σ value. To account for this, we weight the RMSE by σ^2:

$$RMSE_{\text{weighted}} = \left(\frac{\sum_{i=1}^{N} (x_{i,\text{GAP}} - x_{i,\text{DFT}})^2 / \sigma_i^2}{N} \right)^{1/2}$$

Here, N is the number of data points, x_{GAP} is the value measured by GAP, and x_{DFT} is the value measured by DFT.

26 full rounds of iterative training were conducted. See Fig. 8.1 for an iteration-by-iteration progression of the average of the RMSE measured for each force component when comparing the Si-H GAP to DFT on the reference database, for both Si and H separately. Primarily, the new structures have been added in the same procedure as described above, conducting basic MD simulations in order to find structures where the GAP struggles to match DFT measurements. However, beginning in iteration 12, the method of adding H to pure Si structures was refined from the beginning of the training procedure, and subsequently a few sets of such structures from various phases were added to the training set. Once this process was complete, the training set once again was expanded by conducting MD simulations on constituent structures. See Table 8.3 for a list of all additions to the training set which have been conducted thus far. For a visualization of the RMSE accuracy of the Si-H GAP relative to DFT when making energy measurements per atom on the reference set, after iteration 26, see Fig. 8.2.

Of note here is the increase in accuracy that occurs in iteration 7. This increase in accuracy was driven by changing the method by which the regularization parameters were assigned. Previously, the per-structure or per-atom σ values mentioned in the GAP fitting section were not calculated on a per-structure or per-atom basis, but were instead assigned to be the same value for all structures in a given phase. In addition, the force σ fitting protocol was changed to be dependent upon

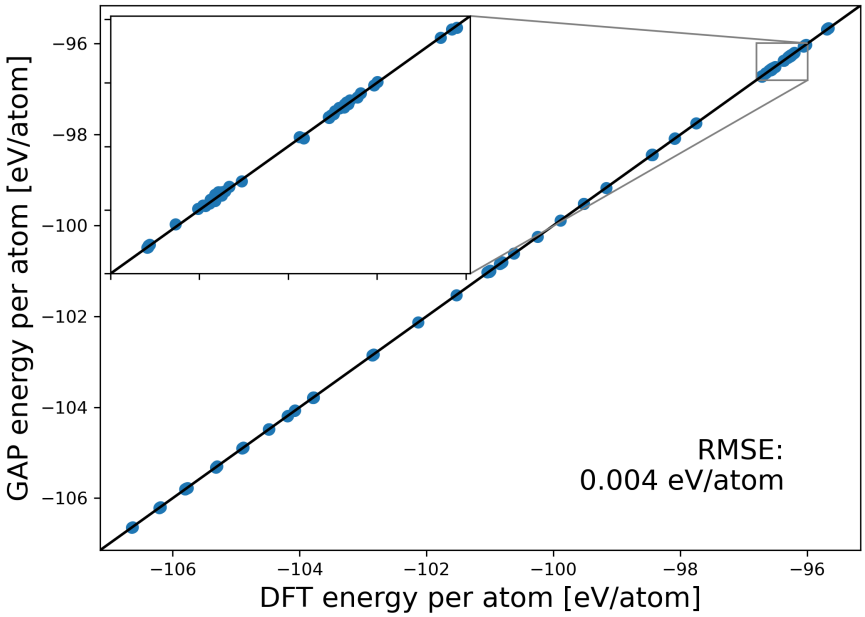

FIGURE 8.2. Comparison between GAP and DFT measurements of the energies/atom on the reference set of structures, after iteration 23.

the magnitude of the atomic force measured by DFT, increasing accuracy as tightly as possible. This change in accuracy meant that the average RMSE now more closely matches the desired regularization, as the regularisation in fitting to structures with large forces and stresses was relaxed. This method has led to a sizeable reduction in the RMSE.

8.3.5. Determining the Usability of the Si-H GAP. The final step in assessing the usability of the potential is to conduct MD simulations representative of how the potential will ultimately be used, and assess the accuracy of the relevant observables in comparison to both DFT and lab results. Our primary goal in developing this Si-H GAP was to use it to create highly accurate a-Si:H structures via a melt-quench procedure, and to subsequently use it to measure defect creation/annihilation energy barriers via the use of the nudged elastic band method.

As such, the most critical round of assessment is the evaluation of the representative liq-Si:H and a-Si:H structures emerging from fully GAP-driven melt-quench procedures. There are several different metrics for evaluating the "realness" of the resulting structures. These include: 1) the radial distribution function (RDF), or correspondingly the partial pair correlation function when multiple atomic species are present; 2) the bond length and angle distributions; 3) the excess energy,

measured relative to c-Si; 4) the vibrational spectra. Of these, there is widespread debate concerning which is the most important metric, with different proponents arguing in favor of either the RDF, or the vibrational spectra [**216**]. It is significantly easier to measure the RDF computationally, but experimental comparison is difficult, requiring x-ray diffraction measurements of the structure factor $S(Q)$ out to at least 40Å [**187**]. Conversely it is much easier to measure the vibrational spectra experimentally using Raman and FTIR spectroscopy [**217**], but it is a substantial challenge computationally. In this paper we report measurements of the partial pair correlation function, leaving vibrational spectra measurements to future work.

8.3.5.1. *Liquid.* To simulate the structure of liquid Si infused with H, we performed constant volume (NVT ensemble) molecular dynamics simulations as implemented in the LAMMPS software package, built with QUIP package support [**179**, **214**, **215**]. One calculation was performed using the Si-H GAP, and one calculation was performed using a Si-H Tersoff potential [**218**, **219**] to provide a point of comparison. Each simulation started with a cubic supercell of side-length 5.26 Å, containing 64 Si atoms and 8 H atoms placed at random, corresponding to a density of 2.58 g/cm^3. The coordinates of these atoms were optimized with the given interatomic potential, before equilibriating at 2000K for 150000 0.5 fs timesteps. Structural data was gathered over an additional 10000 0.25 fs timesteps.

Reference DFT data was gathered from an analogous DFT-BOMD simulation performed using Quantum Espresso. Just as above, the starting configuration consisted of 64 Si and 8 H atoms located at random nonoverlapping positions, in a cubic supercell of side-length 5.26 Å. Simulations consisted of equilibriating the structure at 2000K over 100000 0.25 ps timesteps using the Verlet algorithm, rescaling the velocities at every step to keep the temperature fixed at 2000 K. After equilibriation, structural data was gathered over an additional 6000 0.25 ps time steps.

The partial pair coordination functions are presented in Fig. 8.3. Results are given for the Si-Si partial pair correlation function as well as the Si-H partial pair correlation function. The GAP is in excellent agreement with the DFT in both cases, matching peak locations and heights. The Tersoff potential is visibly in much worse agreement.

The angular distribution functions, also known as the $g_3(r, \theta)$ bond-angle distribution functions, are presented in Fig. 8.4. The cutoff bond length is taken to be the first minimum value of the

partial pair correlation functions after their initial peaks, 3.1 Å for Si-Si, and 2.2 Å for Si-H. Again, the GAP is in excellent agreement with the DFT on both cases, completely reproducing the notable features and closely tracking the DFT results. Again the Tersoff potential is visibly in much worse agreement.

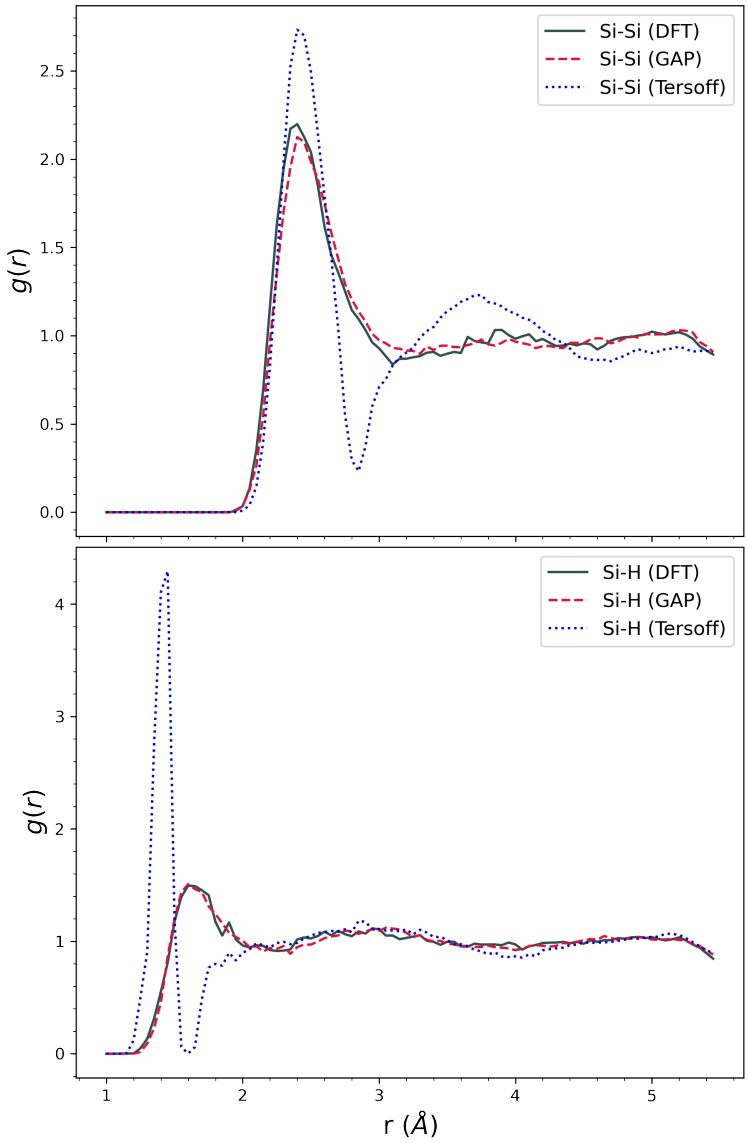

FIGURE 8.3. Partial pair correlation functions of equilibriated liquid Si infused with H, with a density of 2.58 g/cm^3, and T=2000K. Top: Si-Si; bottom: Si-H. Comparison provided between the GAP, a Si-H Tersoff potential, and DFT.

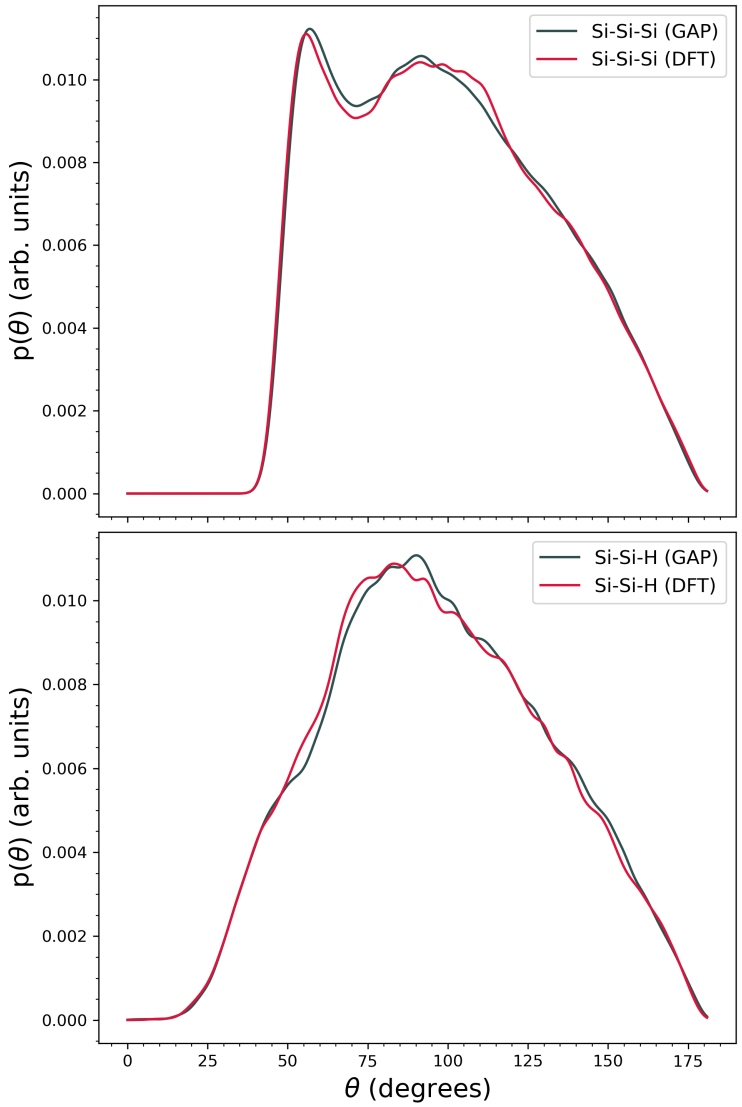

FIGURE 8.4. Angular distribution functions, or $g_3(r, \theta)$, of equilibriated liquid Si infused with H, with a density of 2.58 g/cm^3, and T=2000K. Top: Si-Si-Si; bottom: Si-Si-H. Comparison provided between the Si-H GAP, a Si-H Tersoff potential, and DFT.

Finally, coordination statistics of the Si atoms are presented in Fig. 8.5. Results are only given for the Si-H GAP and DFT. Here the coordination includes both neighboring Si atoms and neighboring H atoms, and the coordination shell for each atomic species is again defined using the first minimum of the corresponding partial pair correlation function. On this front the GAP is also in excellent agreement with the DFT.

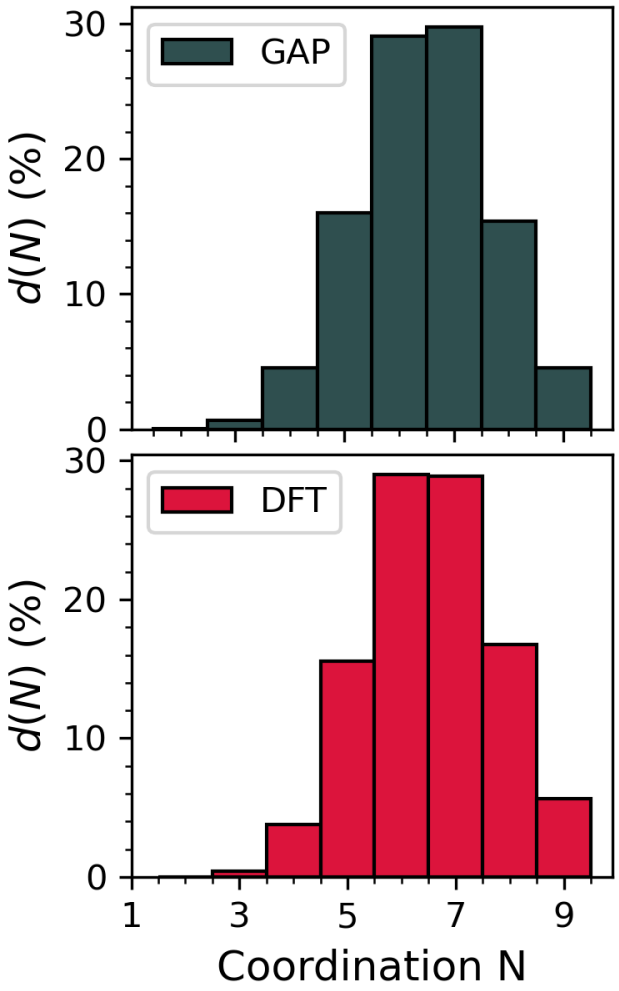

FIGURE 8.5. Averaged coordination statistics of Si atoms in equilibriated liquid Si infused with H, with a density of 2.58 g/cm^3, and T=2000K. Top: GAP; bottom: DFT.

It can be noted that all of these structural quantities are very similar to those of pure liquid Si. See for instance Ref. **220** for a point of comparison.

8.3.5.2. *Amorphous.* To simulate the structure of a-Si:H, we performed both constant volume (NVT ensemble) and constant pressure (NPT) molecular dynamics simulations, again as implemented in the LAMMPS software package with QUIP package support. One calculation was performed using the Si-H GAP, and one calculation was performed using a Si-H Tersoff potential [**218**, **219**] to provide a point of comparison. Each simulation started with the same general procedure as the previous section to create liquid Si infused with H, except with a larger supercell

containing 216 Si atoms and 28 H atoms, and an initial density of 2.3 g/cm^3. Once the liquid structures were equilibriated, the same general procedure was followed for each potential, except the Tersoff calculations used cooling rates which were reduced by a factor of two for further accuracy. The GAP procedure is as follows.

Once the liquid structure was equilibriated, it was cooled in the NVT ensemble down from 2000K to 1500K at a rate of 10^{13} K/s with a timestep of 1 fs. Further equilibriation was then performed at 1500K for 100 ps, before the structure was cooled down to 500K at a rate of 10^{12} K/s. Both of these steps were also performed in the NVT ensemble. To collect structural data, the structure was relaxed to the local energy minimum in atomic positions, then equilibriated for 20000 1 fs timesteps in the NPT ensemble at 0 pressure and 500K, before gathering the structural data over an additional 10000 timesteps.

No reference DFT-BOMD data was gathered for these simulations. Instead, experimental neutron scattering measurements [**221**] and DFT data from another paper [**182**] were used. This is both because using experimental data when available is preferential, and DFT-MD simulations with the number of timesteps given above are extremely computationally expensive, with reduced necessity if there is available reference DFT data to compare against.

The partial pair coordination functions are presented in Fig. 8.6. Results are given for the Si-Si partial pair correlation function as well as the Si-H partial pair correlation function. All structural Si-Si data gives the same key features, with three strong peaks at about 2.4 Å, 3.8 Å, and 5.6 Å, corresponding the first, second and third neighbor peaks. Similarly, all structural Si-H data also gives the same key features, with four peaks at about 1.5 Å, 3.1 Å, 4.9 Å, and 6.5 Å. The GAP is in excellent agreement with the reference DFT in both cases, matching peak locations and heights. Additionally, it slightly improves on the reference DFT in matching the experimental Si-H partial pair correlation function. The Tersoff potential is notably improved in its fit compared to the liquid-Si:H case, particularly when looking at the Si-Si partial pair correlation function, but remains quite poor in its fit of the Si-H partial pair correlation function.

Further structural measurements were taken after performing additional relaxation with DFT, using the same parameters as described in section III.B. The Si-Si-Si and Si-Si-H bond-angle distributions were found to be Gaussian, 109.5$\pm$10.7° and 105$\pm$12° respectively. The coordination of the

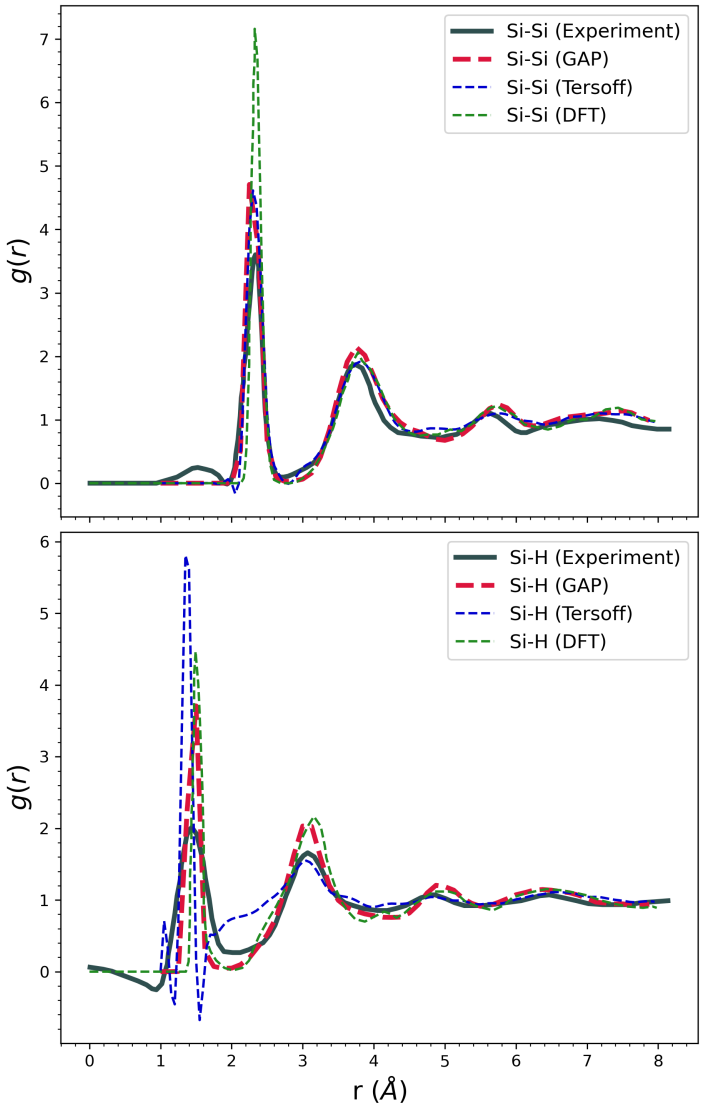

FIGURE 8.6. Partial pair correlation functions of a-Si:H. Top: Si-Si; bottom: Si-H. Results provided for GAP and Tersoff simulations, and reference results generated by a neutron scattering experiment [**221**] and DFT calculations [**182**] are shown for comparison.

central Si atoms was found to be 1.8% 3-fold coordinated, 98% 4-fold coordinated, and 0.2% 5-fold coordinated. The excess energy of the supercell, the energy difference of the supercell compared to a supercell containing hydrogenated crystalline silicon with the same number of Si and H atoms, was found to be 0.09 eV/atom. This is well within the measured a-Si:H experimental range of 0.06 to 0.13 eV/atom [**175**]. As expected, it is lower than the excess energies of 0.13 to 0.14 eV/atom of

pure amorphous silicon structures that we generated using the Si-only GAP [**176**] in the previous chapter, as the presence of the H atoms relieves some of the atomic strain.

8.4. Conclusion

This work clearly demonstrates the utility of using a non-parameterized ML model, here trained by fitting a Gaussian approximation potential with a SOAP kernel to DFT data. The Si-H GAP was not only able to closely match DFT measurements of microscopic quantities such as energies, forces and virial stresses, but it was also able to reproduce structural characteristics such as partial pair correlation functions and the vibrational spectra. Reference structural data taken from Tersoff MD calculations was also provided, and highlighted the improvement that is gained by adopting the non-parameterized model and more accurately matching the target potential energy surface. While the computational complexity, and hence cost, of using a GAP is much higher than a traditional parameterized interatomic potential, it remains significantly faster than DFT-MD, with a much tighter alignment in all key metrics.

The potential presented here is limited in a few ways. (i) It was not developed to be a general-purpose interatomic potential, and thus does not include structural phases beyond the key phases which are needed in order to reliably produce experimentally accurate a-Si:H. For instance, it does not include the various surface reconstructions of diamond Si. Fortunately, future training would simply be a matter of adding additional structures to the training set, and thus the potential can be adapted as needed. (ii) Long-range interactions beyond 5 Å for Si and 3.5 Å for H are not included. This limits the maximum accuracy of the potential, as it runs into locality limits. For a discussion of this phenomenon, see Ref. **222**. Properly including a long-range interaction and integrating it into the short-range interactions is still an outstanding problem with the underlying GAP framework. (iii) The training database was assembled by hand, and did not include any automated procedures for constructing the database. Using an active learning approach would reduce the DFT cost, as DFT would only be performed on an "as needed" basis, and would speed up the training of the potential.

Those issues aside, the merits of the presented potential are undeniable: for the specific structural phases considered, it is more accurate than any potential before it. Few Si-H interatomic

potentials have been developed, and they are not commonly used. This is surprising, as the majority of experimental amorphous silicon structures contain at least trace amounts of atomic H. This potential will thus be able to fill an immediate role.

CHAPTER 9

Conclusions

9.1. Nanoparticles

9.1.1. Summary. In Chapter 2, the Hierarchical Nanoparticle Transport Simulator, HINTS, was introduced. HINTS was used to perform studies on carrier transport in disordered nanoparticle (NP) or nanocrystal (NC) solids.

Chapter 3 used HINTS to model the transport in binary nanocrystal solids (BNS), and study the impact of several factors on this transport. It was observed that the BNS mobility exhibited a minimum at a large-NC-fraction $f_{\mathrm{LNC}} = 0.25{=}0.25$. This was attributed to a percolation picture where, as the LNC fraction f_{LNC} within the small-NC (SNC) matrix starts growing from zero, the few LNCs act as deep traps for the electrons traversing the SNC matrix. Increasing the f_{LNC} concentration of these traps decreases the mobility. However, as the increasing f_{LNC} reaches the above percolation threshold, the LNCs form sample-spanning networks that enable electrons to traverse the entire BNS via low-energy, low disorder LNC pathways. This new percolating transport channel leads to the recovery of the mobility. Trends in the effects of temperature, electron density, charging energy, ligand length, and disorder on the mobility minimum were accounted for by a new physical picture in which capturing an electron renormalizes a deep trap LNCs into either a shallow trap or a kinetic obstacle, depending on the value of the charging energy $\mathrm{E_C}$ relative to the NC energy difference Δ. A central prediction of this model is that the position of the mobility minimum shifts to a larger LNC fraction $f_{\mathrm{LNC}} > f_{\mathrm{P}}$ as the electron density increases, but its depth is modified differently depending on whether $\mathrm{E_C} < \Delta$, or $\mathrm{E_C} > \Delta$. The work in this chapter was published with Davis Unruh as the second author, and can be found at Ref. **223**.

Chapter 4 used complementary HINTS and DMFT work to construct a phase diagram of PbSe NP solids on the filling–disorder plane. Several phase transitions were observed, both in the HINTS work which built from the localized phases, and the DMFT work which built from the extended

phase. We distinguished a Disorder-driven MIT at $n \neq 1$, and an Interaction-driven MIT at $n = 1$. In particular, at $n = 1$, HINTS showed that at large interactions the Mott-localized–to–Disorder-localized transition occurs with a persistent gap. Similar transitions were predicted by the disordered Mott-Hubbard model, and thus we showed that adapting the vast body of knowledge developed for the disordered Mott-Hubbard model for NP solids can and will produce many new insights into the physics of NP solids, and thus can be used to develop strategies to improve their optoelectronic properties. The work in this chapter was published with Davis Unruh as the first author, and can be found at Ref. **81**.

Chapter 5 combined electron tomographic reconstruction and HINTS simulations to meaningfully statiscally analyze the structural disorder in 3D epitaxially-connected PbSe quantum dot superlattice films. On the experimental side, testing correlations between neck number, neck diameter, inter-QD distance, and QD location in the film lead to the discovery of a strong association between neck number and both the average and standard deviation of the nearest neighbor QD distance, demonstrating that QDs with more necks tend to have more ordered local environments. This underscores the need for more complete, uniform necking, which will require fabrication of more perfect oleate-capped SLs and greater control of the kinetics of the phase transition from the oleate-capped SL to the epi-SL. These experimental results were complemented by the theoretical work, which was able to combine nearest-neighbor hopping/tunneling transport in a simulation of the exact tomographic reconstruction. Complementary simulations were also performed on monocrystalline and bicrystalline analogues and showed that SL grain boundaries have limited impact on the electron mobility as long as the grains remain interconnected by necked QDs that form percolating neck networks. An encouraging message of this result is that high mobilities can still be achieved in QD SLs even if they have a high density of grain boundaries, and thus small grain sizes, by increasing the QD attachment density, or neck connectivity, across the SL grain boundaries. To complete the picture, it is natural to expect that once the neck networks connect most of the QDs of the epi-SL to the point that carriers delocalize into mini-bands, further mobility enhancements can be achieved by reducing the density of conventional SL grain boundaries as well. The work in this chapter was published with Davis Unruh as the lead theory author, and can be found at Ref. **80**.

Chapter 6, which wrapped up the nanoparticle work in this dissertation, reported the development of the TRIDENS method which adds three further hierarchial layers on top of the HINTS method in order to simulate extended defects on experimental length scales. In TRIDENS, we first introduced planar defects into thousands of individual NP superlattices (SLs), and constructed the distribution of NP SL mobilities by performing HINTS transport simulations. Second, the defected NP SLs were assembled into a resistor network with more than 10^4 NP SLs, and the overall mobility was measured. Third, and finally, the TRIDENS results were analyzed by finite size scaling to explore whether the percolation transition, separating the phase where the low-mobility-defected NP SLs percolate from the phase where the high-mobility-undefected NP SLs percolate, drives a low-mobility-insulator-to-high-mobility-insulator transport crossover that can be extrapolated to genuinely macroscopic length scales.

Our extensive TRIDENS analysis generated the following results. The introduction of planar defects into NP SLs reduced their mobility by a factor of up to 5. On average, grain boundary defects hinder transport about twice as much as twin planes. This result makes sense, as grain boundaries are more disruptive to lattice periodicity than twin planes, and transport across the grain boundaries involves longer hops between more distant NPs, whereas transport across twin planes proceeds across many NPs shared by the grains on the two sides of the twin plane, and thus it involves regular hop lengths. It is noteworthy that even a reduction of mobility by a factor of 5 is not a qualitative, order-of-magnitude suppression of the transport that indicate a Metal-Insulator-Transition: those are driven by the loss of phase coherence. This finding was bolstered by the resistor network-level analysis, which showed that the introduction of planar defects immediately started to reduce the network mobility. This finding suggests that even small concentrations of planar defects are not shorted out in NP solids, and thus every reduction of the density of planar defects will lead to further improvements of the transport in NP solids. Finally, finite size scaling analysis of the TRIDENS network mobilities demonstrated that increasing the density of the undefected NP SLs drives an underlying, structural/geometric percolation transition in the NP solid, which in turn does indeed drive a low-mobility-insulator-to-high-mobility-insulator transport crossover. The work in this chapter was published with Davis Unruh as the second author, and can be found at Ref. **224**.

9.2. Silicon heterojunctions

9.2.1. Summary. The last two chapters reported two stages of the development of the SolDeg platform for the study of heterojunction solar cell degradation. All of this work has been submitted, separately for the two chapters, for publication with Davis Unruh as the first author. Chapter 7 started by reporting the development of the base SolDeg platform, which was used to study silicon-only heterojunction degradation. SolDeg layered several techniques on top of each other, in order to determine the microscopic dynamics of electronic defect generation from femtoseconds to gigaseconds. The main conclusions were as follows. (1) The degradation of a-Si/c-Si heterojunction solar cells via defect generation is controlled by a very broad distribution of energy barriers, extending from the scale of meV to 4 eV. (2) We have shown that a simple, stretched exponential analytical form can successfully describe the defect generation $N(t)$ over ten orders of magnitude in time. (3) It was found that in relative terms V_{oc} degrades at a rate of 0.2%/year over the first year. (4) In the newly developed time correspondence curve, which connected accelerated testing to normal, fielded degradation, we found a compellingly simple scaling relationship between accelerated and normal times $t(\mathrm{accelerated}) \propto t(\mathrm{normal})^{0.85}$, which can be used to calibrate accelerated testing protocols, making it a more quantitative assessment tool. (5) Experimental work on defect generation in a-Si/c-Si HJ stacks was also carried out. It was found that the degradation rate was high on initial time scales, but slowed considerably at longer time scales. This was attributed to low initial defect densities, in which case hydrogen diffusion will have a stronger effect than it would normally.

Notably, the simulated SolDeg V_{oc} degradation rate was only half that of fielded HJ modules. This difference was suspected to be due to the SolDeg platform not yet including hydrogen or illumination. In response, in Chapter 8 the machine-learning led development of a Si-H interatomic potential using the framework of a Gaussian approximation potential was reported. The training process has been successful in creating an interatomic potential which accurately reproduces DFT measurements of atomic energies, forces, and virial stresses. Validation tests show that the potential can create liquid-Si:H and a-Si:H with the same characteristics as DFT and experiment, respectively. Using this new potential the next stage of SolDeg, adding H and studying H-induced defect generation in a-Si:H/c-Si heterojunctions, can begin.

APPENDIX A

Binary NC Experimental Methods

Chemicals. Lead oxide (PbO, 99.999%), selenium (99.99%), oleic acid (OA, tech. grade, 90%), diphenylphosphine (DPP, 98%), trioctylphosphine (TOP, tech. grade, > 90%), 1-octadecene (ODE, 90%), 1,2-ethanedithiol (EDT, > 98%), trimethylaluminum (97%), and anhydrous solvents were purchased from Aldrich and used as received. Millipore water was degassed with three freeze-pump-thaw cycles before loading into the atomic layer deposition (ALD) system.

Nanocrystal Synthesis. PbSe nanocrystals (NCs) were synthesized and purified using standard air-free techniques. 1.5 g of PbO, 5 g of oleic acid, and 10 g of 1-octadecene was stirred in a three-neck flask at 180°C for 1 hr. 9.5 milliliters of a 1 M solution of trioctylphosphine selenide containing 0.2 milliliters of diphenylphosphine was then rapidly injected into the hot solution. To control the NC size, the NCs were allowed to grow at 160°C for preselected times (several minutes). The reaction was then quenched with a water bath and 15 milliliters of anhydrous hexane. The NCs were purified by three rounds of dispersion/precipitation in hexane/ethanol and stored as a powder in a glovebox for later use.

NC Film Deposition. NC solutions of various LNC number fraction were prepared by suspending appropriate amounts of LNC and SNC powder in dry hexane at a total concentration of 2 mg mL-1. A mechanical dip coater (DC Multi-4, Nima Technology) installed inside of a glovebox was used to prepare NC films via layer-by-layer deposition [48]. Briefly, substrates (glass or prepatterned FET substrates, cleaned by sonication in isopropanol and dried under N2 flow) were alternately dipped into the NC solution and a 1 mM solution of 1,2-ethanedithiol (EDT) in dry acetonitrile. We fabricated films with thicknesses of 30 ± 5 nm for field-effect transistors and 50-100 nm for optical measurements. The fraction and spatial distribution of large NCs in each film type was measured by SEM imaging (FEI Magellan 400) of dip-coated, oleate-capped NC monolayers prior to ligand exchange with EDT.

Atomic Layer Deposition Infilling. The NC transistors were infilled and overcoated with 20 nm of amorphous Al2O3 deposited in a homemade cold-wall traveling wave ALD system within a glovebox from trimethylaluminum and water at a substrate temperature of 54°C and an operating base pressure of about 88 mTorr. Pulse and purge times were 9 ms and 60 s, respectively.

Other Characterization. Transmission electron microscopy (TEM) imaging was performed on a Philips CM20 operating at 200 kV. Optical absorption spectra were acquired with a PerkinElmer Lambda 950 spectrophotometer operating in transmission mode.

APPENDIX B

DMFT Nanoparticle Simulation Methods

We study a four orbital (labeled by $a, b = 1, 2, 3, 4$) Hubbard model with diagonal disorder. The Hamiltonian reads:

$$H = \sum_{\langle i,j\rangle,a,\sigma} t_{ij} d^{\dagger}_{i,a,\sigma} d_{j,a,\sigma} + \sum_{i,a,\sigma} (w_i - \mu) n_{i,a,\sigma} + \sum_i H^{\rm int}_i. \tag{B.1}$$

Here i, j label sites in a lattice and $\langle i, j\rangle$ limit the summation over nearest neighbors only, $n_{i,a,\sigma} = d^{\dagger}_{i,a,\sigma} d_{i,a,\sigma}$ is the density of electrons of spin σ in orbital a on site i, μ is the chemical potential, and t_{ij} is the (nearest neighbor) hopping. The disorder is introduced through the (quenched) random site potential energy w_i, which for simplicity we assume to be independent of orbital and spin index.

For the interaction term, we take the simplest of the standard Slater-Kanamori form

$$H^{\rm int} = \sum_a U n_{a,\uparrow} n_{a,\downarrow} + \sum_{a\neq b,\sigma,\sigma'} U n_{a,\sigma} n_{b,\sigma'} \tag{B.2}$$

where U is the density-density Coulomb interaction. Inter-orbital and Hund's couplings are usually included in the study of materials, where the physics is dominated by electrons in the transition-metal t_{2g} orbitals. The model without disorder has been extensively studied [**225**, **226**, **227**, **228**, **229**, **230**] in that context, and the role of Hund's coupling and rotational invariance has been highlighted. For the NP solid, spin-orbit interactions are not important. Only the 8-fold degeneracy (4 orbitals plus spin) and density-density Coulomb repulsion are relevant.

We solve the model using the single-site dynamical mean-field approximation (DMFT), which neglects the momentum dependence of the self-energy and where the local single-particle Green function is determined self-consistently [**231**]. If in this approach the effect of local disorder is taken into account through the arithmetic mean of the local density of states, one obtains, in the

absence of interactions, the well known coherent potential approximation (CPA). This method is appropriate for our current purpose, namely, to study the effect of disorder on the mobility of the correlated metal state as a function of the occupation, and its effect on the gap at n=1. The CPA-DMFT method, however, does not capture the physics of Anderson localization, and other disorder-DMFT approaches have been proposed. For instance, "statistical DMFT," where not only the averages but the probability distribution itself are determined self-consistently, or "Typical Medium Theory" where geometric averages are considered [**98**, **115**, **116**, **117**, **119**, **120**, **121**, **122**]. These methods are numerically more costly and more relevant to the specific study of the Mott-Anderson transition. The extension of our work in those directions is an interesting perspective.

Here we will consider quenched, uncorrelated, local site energies w_i drawn from a probability distribution function given by:

$$P(w_i) = \frac{1}{2W}\Theta(W - |w_i|) \tag{B.3}$$

with Θ the Heaviside step function. We will set the disorder strength $W \ll U$ where CPA is a good approximation.

In DMFT for disordered electrons, a quasiparticle is characterized by a local but site dependent self-energy $\Sigma_i(i\omega_n)$, with ω_n the fermionic Matsubara frequencies. To obtain those self-energies the problem is mapped into an ensemble of Anderson impurity problems embedded in a self-consistently calculated conduction bath. Here we adopt a semicircular density of state (DOS) so that, in this particular case, the hybridization function is given by:

$$\Delta(i\omega_n) = t^2 G_{\text{avg}}(i\omega_n) \tag{B.4}$$

and the average local Green's function, G_{avg}, is obtained from the self-consistency condition:

$$G_{\text{avg}}(i\omega_n) = \left\langle \frac{1}{i\omega_n + \mu - w_i - \Delta(i\omega_n) - \Sigma_i(i\omega_n)} \right\rangle \tag{B.5}$$

where $\langle \dots \rangle$ stands for the arithmetic average over the distributions of w_i. Since we are dealing with a rather demanding 4-orbital model, we take ten random values of site energies at each self-consistency loop.

The simulations were performed using the continuous-time quantum Monte Carlo implemented in ref **113**, which samples a diagrammatic expansion of the partition function in powers of the impurity-bath hybridization [**232**].

To calculate the mobility we obtain the dc conductivity σ from DMFT:

$$\sigma = \sigma_0 \int_{-\infty}^{\infty} \mathrm{d}\varepsilon \int_{-\infty}^{\infty} \mathrm{d}\omega D(\varepsilon)\rho(\omega,\varepsilon)^2 \left(-\frac{\partial f}{\partial \omega}\right) \tag{B.6}$$

where σ_0 is a constant, f the Fermi function, $D(\varepsilon)$ is the DOS, $\rho(\omega,\varepsilon) = -\frac{1}{\pi}G(i\omega_n \to \omega + i0^+, \varepsilon)$ is the spectral function and $G(i\omega_n,\varepsilon)$ is given by:

$$G(i\omega_n,\varepsilon) = \frac{1}{i\omega_n + \mu - \varepsilon - \Sigma_{\mathrm{avg}}(i\omega_n)} \tag{B.7}$$

with Σ_{avg} obtained from the Dyson equation:

$$\Sigma_{\mathrm{avg}}(i\omega_n) = i\omega_n + \mu - t^2 G_{\mathrm{avg}}(i\omega_n) - [G_{\mathrm{avg}}(i\omega_n)]^{-1}\,. \tag{B.8}$$

In the calculation we set the units of energy such that $t = 0.5$, $U = 7$ and $W = 1$.

Bibliography

[1] NREL. Best research-cell efficiencies. `https://www.nrel.gov/pv/assets/pdfs/best-research-cell-efficiencies.20200104.pdf`, 2020. Accessed: 2020-04-29.

[2] Dirk C Jordan, Chris Deline, Steve Johnston, Steve R Rummel, Bill Sekulic, Peter Hacke, Sarah R Kurtz, Kristopher O Davis, Eric John Schneller, Xingshu Sun, et al. Silicon heterojunction system field performance. *IEEE Journal of Photovoltaics*, 8(1):177–182, 2017.

[3] Graham H Carey, Ahmed L Abdelhady, Zhijun Ning, Susanna M Thon, Osman M Bakr, and Edward H Sargent. Colloidal quantum dot solar cells. *Chem. Rev.*, 115(23):12732–12763, 2015.

[4] Alex Abelson, Caroline Qian, Trenton Salk, Zhongyue Luan, Kan Fu, Jian-Guo Zheng, Jenna L. Wardini, and Matt Law. Collective topo-epitaxy in the self-assembly of a 3d quantum dot superlattice. *Nature Materials*, 19(1):49+, Jan 2020.

[5] Daishun Ling, Michael J. Hackett, and Taeghwan Hyeon. Surface ligands in synthesis, modification, assembly and biomedical applications of nanoparticles. *Nano Today*, 9(4):457–477, 2014.

[6] Danylo Zherebetskyy, Marcus Scheele, Yingjie Zhang, Noah Bronstein, Christopher Thompson, David Britt, Miquel Salmeron, Paul Alivisatos, and Lin-Wang Wang. Hydroxylation of the surface of pbs nanocrystals passivated with oleic acid. *Science*, 344(6190):1380–1384, 2014.

[7] Dmitri V. Talapin, Jong-Soo Lee, Maksym V. Kovalenko, and Elena V. Shevchenko. Prospects of colloidal nanocrystals for electronic and optoelectronic applications. *Chem. Rev.*, 110(1):389–458, January 2010.

[8] Maksym V. Kovalenko, Liberato Manna, Andreu Cabot, Zeger Hens, Dmitri V. Talapin, Cherie R. Kagan, Victor I. Klimov, Andrey L. Rogach, Peter Reiss, Delia J. Milliron, et al. Prospects of nanoscience with nanocrystals. *ACS Nano*, 9(2):1012–1057, 2015.

[9] A. J. Nozik. Quantum dot solar cells. *Physica E: Low-dimensional Systems and Nanostructures*, 14(1-2):115 – 120, 2002.

[10] Prashant V. Kamat. Quantum dot solar cells. semiconductor nanocrystals as light harvesters†. *J. Phys. Chem. C*, 112(48):18737–18753, 2008.

[11] Yasuhiro Shirasaki, Geoffrey J Supran, Moungi G Bawendi, and Vladimir Bulović. Emergence of colloidal quantum-dot light-emitting technologies. *Nat. Photonics*, 7(1):13–23, 2013.

[12] Dmitri V. Talapin and Christopher B. Murray. Pbse nanocrystal solids for n- and p-channel thin film field-effect transistors. *Science*, 310(5745):86–89, 2005.

[13] Frederik Hetsch, Ni Zhao, Stephen V. Kershaw, and Andrey L. Rogach. Quantum dot field effect transistors. *Mater. Today*, 16(9):312–325, September 2013.

[14] William Shockley and Hans J. Queisser. Detailed balance limit of efficiency of p-n junction solar cells. *Journal of Applied Physics*, 32(3):510–519, 1961.

[15] Martin A. Green. *Third generation photovoltaics: advanced solar energy conversion*. Springer Series in Photonics. Springer, 2006.

[16] Lazaro A. Padilha, John T. Stewart, Richard L. Sandberg, Wan Ki Bae, Weon-Kyu Koh, Jeffrey M. Pietryga, and Victor I. Klimov. Carrier multiplication in semiconductor nanocrystals: Influence of size, shape, and composition. *Acc. Chem. Res.*, 46(6):1261–1269, 2013.

[17] S. Wippermann, M. Vörös, D. Rocca, A. Gali, G. Zimanyi, and G. Galli. High-pressure core structures of si nanoparticles for solar energy conversion. *Phys. Rev. Lett.*, 110:046804, Jan 2013.

[18] Márton Vörös, Dario Rocca, Giulia Galli, Gergely T. Zimanyi, and Adam Gali. Increasing impact ionization rates in si nanoparticles through surface engineering: A density functional study. *Phys. Rev. B*, 87:155402, Apr 2013.

[19] Márton Vörös, Stefan Wippermann, Bálint Somogyi, Adam Gali, Dario Rocca, Giulia Galli, and Gergely T. Zimanyi. Germanium nanoparticles with non-diamond core structures for solar energy conversion. *J. Mater. Chem. A*, 2:9820–9827, 2014.

[20] Marco Govoni, Ivan Marri, and Stefano Ossicini. Carrier multiplication between interacting nanocrystals for fostering silicon-based photovoltaics. *Nat. Photonics*, 6:672 – 679, 2012.

[21] R. D. Schaller and V. I. Klimov. High efficiency carrier multiplication in pbse nanocrystals: Implications for solar energy conversion. *Phys. Rev. Lett.*, 92:186601, May 2004.

[22] Octavi E. Semonin, Joseph M. Luther, Sukgeun Choi, Hsiang-Yu Chen, Jianbo Gao, Arthur J. Nozik, and Matthew C. Beard. Peak external photocurrent quantum efficiency exceeding 100% via meg in a quantum dot solar cell. *Science*, 334(6062):1530–1533, 2011.

[23] Charles Smith and David Binks. Multiple exciton generation in colloidal nanocrystals. *Nanomaterials*, 4(1):19–45, 2014.

[24] Saba Saeed, Chris de Weerd, Peter Stallinga, F. C. M. Spoor, Arjan J. Houtepen, Laurens D. A. Siebbeles, and Tom Gregorkiewicz. Carrier multiplication in germanium nanocrystals. *Light Sci. Appl.*, 4:e251, 2015.

[25] Marton Vörös, Giulia Galli, and Gergely T. Zimanyi. Colloidal nanoparticles for intermediate band solar cells. *ACS Nano*, 9:6882 – 6890, 2015.

[26] S. M. Hubbard, C. D. Cress, C. G. Bailey, R. P. Raffaelle, S. G. Bailey, and D. M. Wilt. Effect of strain compensation on quantum dot enhanced gaas solar cells. *Applied Physics Letters*, 92(12):123512, 2008.

[27] X Lan, O Voznyy, M Liu, J Xu, A Proppe, G Walters, F Fan, H Tan, M Liu, and E Sargent. 10.6% certified colloidal quantum dot solar cells via solvent-polarity-engineered halide passivation. *Nano Lett.*, 16(7):4630–4634, 2016.

[28] Shuang Jiao, Jun Du, Zhonglin Du, Donghui Long, Wuyou Jiang, Zhengxiao Pan, Yan Li, and Xinhua Zhong. Nitrogen-doped mesoporous carbons as counter electrodes in quantum dot sensitized solar cells with a conversion efficiency exceeding 12%. *J. Phys. Chem. Lett.*, 8(3):559–564, 2017.

[29] Erin M. Sanehira, Ashley R. Marshall, Jeffrey A. Christians, Steven P. Harvey, Peter N. Ciesielski, Lance M. Wheeler, Philip Schulz, Lih Y. Lin, Matthew C. Beard, and Joseph M. Luther. Enhanced mobility $cspbi_3$ quantum dot arrays for record-efficiency, high-voltage photovoltaic cells. *Sci. Adv.*, 3(10), 2017.

[30] M. Hao, Y. Bai, S. Zeiske, et al. Ligand-assisted cation-exchange engineering for high-efficiency colloidal $cs_{1-x}fa_xpbi_3$ quantum dot solar cells with reduced phase segregation. *Nat. Energy*, 5:79–88, 2020.

[31] Yao Liu, Markelle Gibbs, James Puthussery, Steven Gaik, Rachelle Ihly, Hugh W. Hillhouse, and Matt Law. Dependence of carrier mobility on nanocrystal size and ligand length in PbSe nanocrystal solids. *Nano Lett.*, 10(5):1960–1969, May 2010.

[32] E. Kalesaki, W. H. Evers, G. Allan, D. Vanmaekelbergh, and C. Delerue. Electronic structure of atomically coherent square semiconductor superlattices with dimensionality below two. *Phys. Rev. B*, 88:115431, Sep 2013.

[33] Kevin Whitham, Jun Yang, Benjamin H Savitzky, Lena F. Kourkoutis, Frank Wise, and Tobias Hanrath. Charge transport and localization in atomically coherent quantum dot solids. *Nat. Mater.*, 15:557–563, 2016.

[34] Ruili Wang, Yuequn Shang, Pongsakorn Kanjanaboos, Wenjia Zhou, Zhijun Ning, and Edward H. Sargent. Colloidal quantum dot ligand engineering for high performance solar cells. *Energy Environ. Sci.*, 9:1130–1143, 2016.

[35] Jaeyoung Jang, Wenyong Liu, Jae Sung Son, and Dmitri V. Talapin. Temperature-dependent hall and field-effect mobility in strongly coupled all-inorganic nanocrystal arrays. *Nano Lett.*, 14:653–662, 2014.

[36] Jong-Soo Lee, Maksym V. Kovalenko, Jing Huang, Dae Sung Chung, and Dmitri V. Talapin. Band-like transport, high electron mobility and high photoconductivity in all-inorganic nanocrystal arrays. *Nat. Nanotech.*, 6:348–352, 2011.

[37] Chia-Hao M. Chuang, Patrick R. Brown, Vladimir Bulović, and Moungi G. Bawendi. Improved performance and stability in quantum dot solar cells through band alignment engineering. *Nat. Mater.*, 13:796 – 801, 2014.

[38] Daniel M Kroupa, Márton Vörös, Nicholas P Brawand, Brett W McNichols, Elisa M Miller, Jing Gu, Arthur J Nozik, Alan Sellinger, Giulia Galli, and Matthew C Beard. Tuning colloidal quantum dot band edge positions through solution-phase surface chemistry modification. *Nature communications*, 8:15257, 2017.

[39] Ting Chen, K. V. Reich, Nicolaas J Kramer, Han Fu, Uwe R Kortshagen, and B. I. Shklovskii. Metal-insulator transition in films of doped semiconductor nanocrystals. *Nat. Mater.*, 15(3):299–303, 2016.

[40] Ji-Hyuk Choi, Aaron T. Fafarman, Soong Ju Oh, Dong-Kyun Ko, David K. Kim, Benjamin T. Diroll, Shin Muramoto, J. Greg Gillen, Christopher B. Murray, and Cherie R. Kagan. Bandlike transport in strongly coupled and doped quantum dot solids: A route to high-performance thin-film electronics. *Nano Lett.*, 12(5):2631–2638, May 2012.

[41] Elise Talgorn, Yunan Gao, Michiel Aerts, Lucas T Kunneman, Juleon M Schins, TJ Savenije, Marijn A van Huis, Herre SJ van der Zant, Arjan J Houtepen, and Laurens DA Siebbeles. Unity quantum yield of photogenerated charges and band-like transport in quantum-dot solids. *Nat. Nanotechnol.*, 6(11):733–739, 2011.

[42] Matteo Cargnello, Aaron C Johnston-Peck, Benjamin T Diroll, Eric Wong, Bianca Datta, Divij Damodhar, Vicky VT Doan-Nguyen, Andrew A Herzing, Cherie R Kagan, and Christopher B Murray. Substitutional doping in nanocrystal superlattices. *Nature*, 524(7566):450–453, 2015.

[43] Benjamin H. Savitzky, Robert Hovden, Kevin Whitham, Jun Yang, Frank Wise, Tobias Hanrath, and Lena F. Kourkoutis. Propagation of structural disorder in epitaxially connected quantum dot solids from atomic to micron scale. *Nano Lett.*, 16:5714–5718, 2016.

[44] Yao Liu, Jason Tolentino, Markelle Gibbs, Rachelle Ihly, Craig L Perkins, Yu Liu, Nathan Crawford, John C Hemminger, and Matt Law. Pbse quantum dot field-effect transistors with air-stable electron mobilities above 7 cm2 v–1 s–1. *Nano Lett.*, 13(4):1578–1587, 2013.

[45] Soong Ju Oh, Nathaniel E. Berry, Ji-Hyuk Choi, E. Ashley Gaulding, Taejong Paik, Sung-Hoon Hong, Christopher B. Murray, and Cherie R. Kagan. Stoichiometric control of lead chalcogenide nanocrystal solids to enhance their electronic and optoelectronic device performance. *ACS Nano*, 7:2413–2421, 2013.

[46] Wiel H Evers, Juleon M Schins, Michiel Aerts, Aditya Kulkarni, Pierre Capiod, Maxime Berthe, Bruno Grandidier, Christophe Delerue, Herre SJ Van Der Zant, Carlo Van Overbeek, et al. High charge mobility in two-dimensional percolative networks of pbse quantum dots connected by atomic bonds. *Nat. Commun.*, 6:8195, 2015.

[47] K. V. Reich, Tianran Chen, and B. I. Shklovskii. Theory of a field-effect transistor based on a semiconductor nanocrystal array. *Phys. Rev. B*, 89:235303, Jun 2014.

[48] R. E. Chandler, A. J. Houtepen, J. Nelson, and D. Vanmaekelbergh. Electron transport in quantum dot solids: Monte carlo simulations of the effects of shell filling, coulomb repulsions, and site disorder. *Phys. Rev. B*, 75(8):085325, February 2007.

[49] I. Carbone, S. A. Carter, and G. T. Zimanyi. Monte carlo modeling of transport in PbSe nanocrystal films. *J. Appl. Phys.*, 114(19):193709, November 2013.

[50] Luman Qu, Márton Vörös, and Gergely T. Zimanyi. Metal-insulator transition in nanoparticle solids: Insights from kinetic monte carlo simulations. *Sci. Rep.*, 7(1):7071, 2017.

[51] Luman Qu, Chase Hansen, Marton Vörös, and Gergely T. Zimanyi. Commensuration effects in layered nanoparticle solids. *Phys. Rev. B*, 101(4), JAN 17 2020.

[52] Frank K.A. Nyarko, G. Takyi, and Emeka H. Amalu. Robust crystalline silicon photovoltaic module (c-si pvm) for the tropical climate: Future facing the technology. *Scientific African*, 8:e00359, 2020.

[53] Yuqiang Liu, Yajuan Li, Yiliang Wu, Guangtao Yang, Luana Mazzarella, Paul Procel-Moya, Adele C. Tamboli, Klaus Weber, Mathieu Boccard, Olindo Isabella, Xinbo Yang, and Baoquan Sun. High-efficiency silicon heterojunction solar cells: Materials, devices and applications. *Materials Science and Engineering: R: Reports*, 142:100579, 2020.

[54] Stefaan De Wolf, Antoine Descoeudres, Zachary C. Holman, and Christophe Ballif. High-efficiency silicon heterojunction solar cells: A review. *Green*, 2(1):7–24, 2012.

[55] Arno Smets, Klaus-Dieter Jäger, Olindo Isabella, René van Swaaij, and Miro Zeman. *Solar energy: the physics and engineering of photovoltaic conversion, technologies and systems*. UIT Cambridge, 2016.

[56] Jan Haschke, Olivier Dupré, Mathieu Boccard, and Christophe Ballif. Silicon heterojunction solar cells: Recent technological development and practical aspects - from lab to industry. *Solar Energy Materials and Solar Cells*, 187:140–153, 2018.

[57] International Technology Roadmap for Photovoltaic (ITRPV). Results 2020. `https://itrpv.vdma.org/`, 2020. Accessed: 2020-05-03.

[58] D. C. Jordan and S. R. Kurtz. Photovoltaic degradation rates—an analytical review. *Progress in Photovoltaics: Research and Applications*, 21(1):12–29, 2013.

[59] Chris Deline, Steve Johnston, Steve R. Rummel, Bill Sekulic, Dirk C Jordan, Steve R Rummel, Peter Hacke, Sarah R Kurtz, Kristopher O Davis, Eric John Schneller, Xingshu Sun, Muhammad A Alam, and Ronald A Sinton. Silicon heterojunction system field performance. *IEEE Journal of Photovoltaics*, 8(1):177–182, 2018.

[60] T. Ishii, S. Choi, R. Sato, Y. Chiba, and A. Masuda. Annual degradation rates of recent c-si pv modules under subtropical coastal climate conditions. In *2018 IEEE 7th World Conference on Photovoltaic Energy Conversion (WCPEC) (A Joint Conference of 45th IEEE PVSC, 28th PVSEC 34th EU PVSEC)*, pages 705–708, 2018.

[61] Simone Bernardini and Mariana I. Bertoni. Insights into the degradation of amorphous silicon passivation layer for heterojunction solar cells. *Phys. Status Solidi A*, 216(4):1800705, 2019.

[62] Silvia Martin De Nicolas, Stefaan De Wolf, Christophe Ballif, Jakub Holovský, and Silvia Martín De Nicolás. Amorphous/crystalline silicon interface stability: Correlation between infrared spectroscopy and electronic passivation properties. *Adv. Mater. Interfaces*, 7(20):2000957, 2020.

[63] Phillip Hamer, Moonyong Kim, Catherine Chan, Alison Ciesla Nee Wenham, Daniel Chen, Alison Ciesla nee Wenham, Fiacre Rougieux, Yuchao Zhang, Malcolm Abbott, and Brett Hallam. Hydrogen-induced degradation: Explaining the mechanism behind light- and elevated temperature-induced degradation in n- and p-type silicon. *Sol. Energy Mater. Sol. Cells*, 207:110353, 2020.

[64] Hongbo Tong, Haitao Zhu, Chao Ding, Hua Li, Ran Chen, Daniel Chen, Brett Hallam, Chee Mun Chong, Stuart Wenham, and Alison Ciesla. 23.83% efficient mono-perc incorporating advanced hydrogenation. *Prog. Photovolt.*, 28(12):1239–1247, 2020.

[65] Phillip G. Hamer, Moonyong Kim, Tsun H. Fung, Gabrielle Bourret-Sicotte, Daniel Chen, Phillip G Hamer, Tsun H Fung, Shaoyang Liu, Catherine E Chan, Alison Ciesla, Ran Chen, Malcolm D Abbott, Brett J Hallam, and Stuart R Wenham. Hydrogen induced degradation: A possible mechanism for light- and elevated temperature- induced degradation in n-type silicon. *Sol. Energy Mater. Sol. Cells*, 185:174–182, 2018.

[66] Inuk Kang and Frank W Wise. Electronic structure and optical properties of pbs and pbse quantum dots. *J. Opt. Soc. Am. B*, 14(7):1632–1646, 1997.

[67] J. M. An, A. Franceschetti, and A. Zunger. Electron and hole addition energies in PbSe quantum dots. *Phys. Rev. B*, 76(4):045401, Jul 2007.

[68] Christophe Delerue and Michel Lannoo. *Nanostructures: Theory and Modeling*. Springer-Verlag Berlin Heidelberg, 2004.

[69] Arjan J. Houtepen, Daan Kockmann, and Daniël Vanmaekelbergh. Reappraisal of variable-range hopping in quantum-dot solids. *Nano Lett.*, 8(10):3516–3520, 2008.

[70] Dong Yu, Congjun Wang, Brian L. Wehrenberg, and Philippe Guyot-Sionnest. Variable range hopping conduction in semiconductor nanocrystal solids. *Phys. Rev. Lett.*, 92(21):216802, May 2004.

[71] A. B. Bortz, M. H. Kalos, and J. L. Lebowitz. A new algorithm for monte carlo simulation of ising spin systems. *J. Comput. Phys.*, 17:10–18, 1975.

[72] Yingjie Zhang, Danylo Zherebetskyy, Noah D. Bronstein, Sara Barja, Leonid Lichtenstein, David Schuppisser, Lin-Wang Wang, A. Paul Alivisatos, and Miquel Salmeron. Charge percolation pathways guided by defects in quantum dot solids. *Nano Lett.*, 15:3249–3253, 2015.

[73] Angang Dong, Xincheng Ye, Jun Chen, and Christopher B. Murray. Two-dimensional binary and ternary nanocrystal superlattices: The case of monolayers and bilayers. *Nano Lett.*, 11:1804–1809, 2011.

[74] Yaoting Wu, Siming Li, Natalie Gogotsi, Tianshuo Zhao, Blaise Fleury, Cherie R. Kagan, Christopher B. Murray, and Jason B. Baxter. Directional carrier transfer in strongly coupled binary nanocrystal superlattice films formed by assembly and in situ ligand exchange at a liquid–air interface. *J. Phys. Chem. C*, 121:4146–4157, 2017.

[75] Elena V. Shevchenko, Dmitri V. Talapin, Nicholas A. Kotov, Stephen O'Brien, and Christopher B. Murray. Structural diversity in binary nanoparticle superlattices. *Nature*, 439:7072, 2006.

[76] Hadrien Lepage, Anne Kaminski-Cachopo, Alain Poncet, and Gilles le Carval. Simulation of electronic transport in silicon nanocrystal solids. *J. Phys. Chem. C*, 116:10873–10880, 2012.

[77] Hadrien Lepage. *Modélisation de solides à nanocristaux de silicium*. PhD thesis, institut national des sciences appliquées de Lyon, 2013.

[78] Jihye Lee, One Choi, and Eunji Sim. Nonmonotonic size-dependent carrier mobility in pbse nanocrystal arrays. *J. Phys. Chem. Lett.*, 3:714–719, 2012.

[79] Marcus Scheele, Jesse H. Engel, Vivian E. Ferry, David Hanifi, Yi Liu, and A. Paul Alivisatos. Nonmonotonic size dependence in the hole mobility of methoxide-stabilized pbse quantum dot solids. *ACS Nano*, 7:6774–6781, 2013.

[80] Xiaolei Chu, Hamed Heidari, Alex Abelson, Davis Unruh, Chase Hansen, Gergely Qian, Caroline an Zimanyi, Matt Law, and Adam J. Moulé. Structural characterization of a polycrystalline epitaxially-fused colloidal quantum dot superlattice by electron tomography. *J. Mater. Chem. A*, 8:18254, 2020.

[81] Davis Unruh, Alberto Camjayi, Chase Hansen, Joel Bobadilla, Marcelo J. Rozenberg, and Gergely T. Zimanyi. Disordered mott–hubbard physics in nanoparticle solids: Transitions driven by disorder, interactions, and their interplay. *Nano Lett.*, 20:8569–8575, 2020.

[82] Aleksandar Donev, Salvatore Torquato, and Frank H. Stillinger. Neighbor list collision-driven molecular dynamics simulation for nonspherical hard particles. i. algorithmic details. *J. Comp. Phys.*, 202:737–764, 2005.

[83] Jacek Jasieniak, Marco Califano, and Scott E. Watkins. Size-dependent valence and conduction band-edge energies of semiconductor nanocrystals. *ACS Nano*, 5:5888–5902, 2011.

[84] Elisa M. Miller, Daniel M. Kroupa, Jianbing Zhang, Ashley R. Schulz, Philip an Marshall, Antoine Kahn, Stephan Lany, Joseph M. Luther, Matthew C. Beard, Craig L. Perkins, and Jao van de Lagemaat. Revisiting the valence and conduction band size dependence of pbs quantum dot thin films. *ACS Nano*, 10:3302–3311, 2016.

[85] Yao Liu, Markelle Gibbs, Craig L. Perkins, Jason Tolentino, Mohammad H. Zarghami, Jorge Bustamante Jr., and Matt Law. Robust, functional nanocrystal solids by infilling with atomic layer deposition. *Nano Lett.*, 11:5349–5355, 2011.

[86] Robert M. Ziff and Salvatore Torquato. Percolation of disordered jammed sphere packings. *J. Phys. A. Math. Theor.*, 50:085001, 2017.

[87] Moon Sung Kang, Ayaskanta Sahu, David J. Norris, and C. Daniel Frisbie. Size- and temperature-dependent charge transport in PbSe nanocrystal thin films. *Nano Lett.*, 11(9):3887–3892, 2011.

[88] C. Delerue, M. Lannoo, and G. Allan. Excitonic and quasiparticle gaps in si nanocrystals. *Phys. Rev. Lett.*, 84:2457–2460, Mar 2000.

[89] M. Lannoo, C. Delerue, and G. Allan. Screening in semiconductor nanocrystallites and its consequences for porous silicon. *Phys. Rev. Lett.*, 74:3415–3418, Apr 1995.

[90] Patrick A. Lee and T. V. Ramakrishnan. Disordered electronic systems. *Rev. Mod. Phys.*, 57:287–337, Apr 1985.

[91] A M. Finkel'shtein. Influence of coulomb interaction on the properties of disordered metals. *Zh. Eksp. Teor. Fiz.*, 84(1):168–189, 1983.

[92] B L. Altshuler, A G. Aronov, and P A. Lee. Interaction effects in disordered fermi systems in 2 dimensions. *Phys. Rev. Lett.*, 44(19):1288–1291, 1980.

[93] C. Castellani, G. Kotliar, and P. A. Lee. Fermi-liquid theory of interacting disordered-systems and the scaling theory of the metal-insulator-transition. *Phys. Rev. Lett.*, 59(3):323–326, JUL 20 1987.

[94] Günter Schmid. *Nanoparticles: From Theory to Application*. John Wiley & Sons, 2006.

[95] Heng Liu, Alexandre Pourret, and Philippe Guyot-Sionnest. Mott and efros-shklovskii variable range hopping in CdSe quantum dots films. *ACS Nano*, 4(9):5211–5216, Sep 2010.

[96] A. L. Efros and B. I. Shklovskii. Critical behaviour of conductivity and dielectric constant near the metal-non-metal transition threshold. *phys. stat. sol. (b)*, 76(2):475–485, 1976.

[97] M C O. Aguiar, V. Dobrosavljević, E. Abrahams, and G. Kotliar. Critical behavior at the mott-anderson transition: A typical-medium theory perspective. *Phys. Rev. Lett.*, 102:156402, Apr 2009.

[98] Helena Bragança, M. C. O. Aguiar, J. Vučičević, D. Tanasković, and V. Dobrosavljević. Anderson localization effects near the mott metal-insulator transition. *Phys. Rev. B*, 92:125143, 2015.

[99] Krzysztof Byczuk, Walter Hofstetter, and Dieter Vollhardt. Mott-hubbard transition versus anderson localization in correlated electron systems with disorder. *Phys. Rev. Lett.*, 94:056404, Feb 2005.

[100] Sampaio, K. C. Beverly, and J. R. Heath. Dc transport in self-assembled 2d layers of ag nanoparticles. *The Journal of Physical Chemistry B*, 105(37):8797–8800, 2001.

[101] Tim Byrnes, Na Young Kim, Kenichiro Kusudo, and Yoshihisa Yamamoto. Quantum simulation of fermi-hubbard models in semiconductor quantum-dot arrays. *Phys. Rev. B*, 78:075320, Aug 2008.

[102] C. A. Stafford and S. Das Sarma. Collective coulomb blockade in an array of quantum dots: A mott-hubbard approach. *Phys. Rev. Lett.*, 72:3590–3593, May 1994.

[103] Andrew Shabaev, Alexander L Efros, and Alexei L Efros. Dark and photo-conductivity in ordered array of nanocrystals. *Nano Lett.*, 13(11):5454—5461, 2013.

[104] F. Remacle. On electronic properties of assemblies of quantum nanodots. *J. Phys. Chem. A*, 104(20):4739–4747, 2000.

[105] F. Remacle and R. D. Levine. Electronic response of assemblies of designer atoms: The metal-insulator transition and the role of disorder. *J. Am. Chem. Soc.*, 122(17):4084–4091, 2000.

[106] Cherie R. Kagan and Christopher B. Murray. Charge transport in strongly coupled quantum dot solids. *Nat. Nanotechnol.*, 10:1013—-1026, 2015.

[107] S V Kravchenko and M P Sarachik. Metal–insulator transition in two-dimensional electron systems. *Reports on Progress in Physics*, 67(1):1–44, dec 2003.

[108] C. Castellani, C. Di Castro, and P. A. Lee. Metallic phase and metal-insulator transition in two-dimensional electronic systems. *Phys. Rev. B*, 57:R9381–R9384, Apr 1998.

[109] J M. An, A. Franceschetti, S V. Dudiy, and A. Zunger. The peculiar electronic structure of pbse quantum dots. *Nano Lett.*, 6(12):2728–2735, 2006.

[110] Marcelo J. Rozenberg. Integer-filling metal-insulator transitions in the degenerate hubbard model. *Phys. Rev. B*, 55:R4855–R4858, Feb 1997.

[111] Antoine Georges, Gabriel Kotliar, Werner Krauth, and Marcelo Rozenberg. Dynamical mean-field theory of strongly correlated fermion systems and the limit of infinite dimensions. *Rev. Mod. Phys.*, 68(1):13–125, 1996.

[112] Emanuel Gull, Andrew J. Millis, Alexander I. Lichtenstein, Alexey N. Rubtsov, Matthias Troyer, and Philipp Werner. Continuous-time monte carlo methods for quantum impurity models. *Rev. Mod. Phys.*, 83(2):349–404, 2011.

[113] Kristjan Haule. Quantum monte carlo impurity solver for cluster dynamical mean-field theory and electronic structure calculations with adjustable cluster base. *Phys. Rev. B*, 75:155113, 2007.

[114] Philipp Werner, Emanuel Gull, and Andrew J. Millis. Metal-insulator phase diagram and orbital selectivity in three-orbital models with rotationally invariant hund coupling. *Phys. Rev. B*, 79:115119, Mar 2009.

[115] V. Janis˘ and D. Vollhardt. Coupling of quantum degrees of freedom in strongly interacting disordered electron systems. *Phys. Rev. B*, 46:15712–15715, Dec 1992.

[116] V. Dobrosavljević and G. Kotliar. Strong correlations and disorder in d=∞ and beyond. *Phys. Rev. B*, 50:1430–1449, Jul 1994.

[117] M. Ulmke, V. Janiš, and D. Vollhardt. Anderson-hubbard model in infinite dimensions. *Phys. Rev. B*, 51:10411–10426, Apr 1995.

[118] V. Dobrosavljević and G. Kotliar. Mean field theory of the mott-anderson transition. *Phys. Rev. Lett.*, 78:3943–3946, May 1997.

[119] M. C. O. Aguiar, V. Dobrosavljević, E. Abrahams, and G. Kotliar. Effects of disorder on the non-zero temperature mott transition. *Phys. Rev. B*, 71:205115, May 2005.

[120] Miloš M. Radonjić, D. Tanasković, V. Dobrosavljević, and K. Haule. Influence of disorder on incoherent transport near the mott transition. *Phys. Rev. B*, 81:075118, Feb 2010.

[121] Krzysztof Byczuk, Walter Hofstetter, and Dieter Vollhardt. Anderson localization vs. mott-hubbard metal-insulator transition in disordered, interacting lattice fermion systems. *Int. J. Mod. Phys. B*, 24(12n13):1727–1755, 2010.

[122] Helena Bragança, M. C. O. Aguiar, J. Vučičević, D. Tanasković, and V. Dobrosavljević. Anderson localization effects near the mott metal-insulator transition. *Phys. Rev. B*, 92:125143, Sep 2015.

[123] Philippe Guyot-Sionnest. Electrical transport in colloidal quantum dot films. *J. Phys. Chem. Lett.*, 3(9):1169–1175, 2012.

[124] Iwan Moreels, Karel Lambert, Dries Smeets, David De Muynck, Tom Nollet, José C Martins, Frank Vanhaecke, Andre Vantomme, Christophe Delerue, Guy Allan, et al. Size-dependent optical properties of colloidal pbs quantum dots. *ACS Nano*, 3(10):3023–3030, 2009.

[125] William J Baumgardner, Kevin Whitham, and Tobias Hanrath. Confined-but-connected quantum solids *via* controlled ligand displacement. *Nano Lett.*, 13(7):3225–3231, 2013.

[126] Wiel H Evers, Bart Goris, Sara Bals, Marianna Casavola, Joost De Graaf, Rene Van Roij, Marjolein Dijkstra, and Daniël Vanmaekelbergh. Low-dimensional semiconductor superlattices formed by geometric control over nanocrystal attachment. *Nano Lett.*, 13(6):2317–2323, 2012.

[127] CS Suchand Sandeep, Jon Mikel Azpiroz, Wiel H Evers, Simon C Boehme, Iwan Moreels, Sachin Kinge, Laurens DA Siebbeles, Ivan Infante, and Arjan J Houtepen. Epitaxially connected pbse quantum-dot films: Controlled neck formation and optoelectronic properties. *ACS Nano*, 8(11):11499–11511, 2014.

[128] Mark P Boneschanscher, Wiel H Evers, Jaco J Geuchies, Thomas Altantzis, Bart Goris, Freddy T Rabouw, SAP Van Rossum, Herre SJ van der Zant, Laurent DA Siebbeles, Gustaaf Van Tendeloo, et al. Long-range orientation and atomic attachment of nanocrystals in 2d honeycomb superlattices. *Science*, 344(6190):1377–1380, 2014.

[129] Man Zhao, Fangxu Yang, Chao Liang, Dawei Wang, Defang Ding, Jiawei Lv, Jianqi Zhang, Wenping Hu, Chenguang Lu, and Zhiyong Tang. High hole mobility in long-range ordered 2d lead sulfide nanocrystal monolayer films. *Adv. Funct. Mater.*, 26(28):5182–5188, 2016.

[130] Jaco J Geuchies, Carlo Van Overbeek, Wiel H Evers, Bart Goris, Annick De Backer, Anjan P Gantapara, Freddy T Rabouw, Jan Hilhorst, Joep L Peters, Oleg Konovalov, et al. In situ study of the formation mechanism of two-dimensional superlattices from pbse nanocrystals. *Nat. Mater.*, 15(12):1248, 2016.

[131] Willem Walravens, Jonathan De Roo, Emile Drijvers, Stephanie Ten Brinck, Eduardo Solano, Jolien Dendooven, Christophe Detavernier, Ivan Infante, and Zeger Hens. Chemically triggered formation of two-dimensional epitaxial quantum dot superlattices. *ACS Nano*, 10(7):6861–6870, 2016.

[132] Man Zhao, Defang Ding, Fangxu Yang, Dawei Wang, Jiawei Lv, Wenping Hu, Chenguang Lu, and Zhiyong Tang. Ligand effects on electronic and optoelectronic properties of two-dimensional pbs necking percolative superlattices. *Nano Res.*, 10(4):1249–1257, 2017.

[133] Benjamin E Treml, Benjamin H Savitzky, Ali M Tirmzi, Jessica Cimada DaSilva, Lena F Kourkoutis, and Tobias Hanrath. Successive ionic layer absorption and reaction for postassembly control over inorganic interdot bonds in long-range ordered nanocrystal films. *ACS Appl. Mater. Interfaces*, 9(15):13500–13507, 2017.

[134] Daniel M Balazs, Bartosz M Matysiak, Jamo Momand, Artem G Shulga, Maria Ibáñez, Maksym V Kovalenko, Bart J Kooi, and Maria Antonietta Loi. Electron mobility of 24 $cm^2v^{-1}s^{-1}$ in pbse colloidal-quantum-dot superlattices. *Adv. Mater.*, 30(38):1802265, 2018.

[135] Carlo Van Overbeek, Joep L Peters, Susan AP Van Rossum, Marc Smits, Marijn A Van Huis, and Daniel Vanmaekelbergh. Interfacial self-assembly and oriented attachment in the family of pbx (x= s, se, te) nanocrystals. *J. Phys. Chem. C*, 122(23):12464–12473, 2018.

[136] Benjamin T Diroll, Nicholas J Greybush, Cherie R Kagan, and Christopher B Murray. Smectic nanorod superlattices assembled on liquid subphases: Structure, orientation, defects, and optical polarization. *Chem. Mater.*, 27(8):2998–3008, 2015.

[137] Davide Altamura, Vaclav Holý, Dritan Siliqi, Indira Chaitanya Lekshmi, Concetta Nobile, Giuseppe Maruccio, P Davide Cozzoli, Lixin Fan, Fabia Gozzo, and Cinzia Giannini. Exploiting gisaxs for the study of a 3d ordered superlattice of self-assembled colloidal iron oxide nanocrystals. *Cryst. Growth Des.*, 12(11):5505–5512, 2012.

[138] Kevin Whitham and Tobias Hanrath. Formation of epitaxially connected quantum dot solids: Nucleation and coherent phase transition. *J. Phys. Chem. Lett.*, 8(12):2623–2628, 2017.

[139] Heiner Friedrich, Cedric J Gommes, Karin Overgaag, Johannes D Meeldijk, Wiel H Evers, Bart de Nijs, Mark P Boneschanscher, Petra E de Jongh, Arie J Verkleij, Krijn P de Jong, et al. Quantitative structural analysis of binary nanocrystal superlattices by electron tomography. *Nano Lett.*, 9(7):2719–2724, 2009.

[140] Mark P Boneschanscher, Wiel H Evers, Weikai Qi, Johannes D Meeldijk, Marjolein Dijkstra, and Daniel Vanmaekelbergh. Electron tomography resolves a novel crystal structure in a binary nanocrystal superlattice. *Nano Lett.*, 13(3):1312–1316, 2013.

[141] Wiel H Evers, Heiner Friedrich, Laura Filion, Marjolein Dijkstra, and Daniel Vanmaekelbergh. Observation of a ternary nanocrystal superlattice and its structural characterization by electron tomography. *Angew. Chem., Int. Ed.*, 48(51):9655–9657, 2009.

[142] Joep L Peters, Thomas Altantzis, Ivan Lobato, Maryam Alimoradi Jazi, Carlo Van Overbeek, Sara Bals, Daniel Vanmaekelbergh, and Sophia Buhbut Sinai. Mono-and multilayer silicene-type honeycomb lattices by oriented attachment of pbse nanocrystals: Synthesis, structural characterization, and analysis of the disorder. *Chem. Mater.*, 30(14):4831–4837, 2018.

[143] Benjamin H Savitzky, Kevin Whitham, Kaifu Bian, Robert Hovden, Tobias Hanrath, and Lena F Kourkoutis. Three-dimensional arrangement and connectivity of lead-chalcogenide nanoparticle assemblies for next generation photovoltaics. *Microsc. Microanal.*, 20(S3):542–543, 2014.

[144] Jeannot Trampert and Jean-Jacques Leveque. Simultaneous iterative reconstruction technique: Physical interpretation based on the generalized least squares solution. *J. Geophys. Res.: Solid Earth*, 95(B8):12553–12559, 1990.

[145] Wim van Aarle, Willem Jan Palenstijn, Jan De Beenhouwer, Thomas Altantzis, Sara Bals, K Joost Batenburg, and Jan Sijbers. The astra toolbox: A platform for advanced algorithm development in electron tomography. *Ultramicroscopy*, 157:35–47, 2015.

[146] Chien-Chun Chen, Chun Zhu, Edward R White, Chin-Yi Chiu, MC Scott, BC Regan, Laurence D Marks, Yu Huang, and Jianwei Miao. Three-dimensional imaging of dislocations in a nanoparticle at atomic resolution. *Nature*, 496(7443):74, 2013.

[147] Han Fu, K. V. Reich, and B. I. Shklovskii. Hopping conductivity and insulator-metal transition in films of touching semiconductor nanocrystals. *Phys. Rev. B*, 93:125430, Mar 2016.

[148] Angang Dong, Jun Chen, Patrick M Vora, James M Kikkawa, and Christopher B Murray. Binary nanocrystal superlattice membranes self-assembled at the liquid–air interface. *Nature*, 466(7305):474, 2010.

[149] Angang Dong, Yucong Jiao, and Delia J Milliron. Electronically coupled nanocrystal superlattice films by in situ ligand exchange at the liquid–air interface. *ACS Nano*, 7(12):10978–10984, 2013.

[150] Mark C Weidman, Detlef-M Smilgies, and William A Tisdale. Kinetics of the self-assembly of nanocrystal superlattices measured by real-time in situ x-ray scattering. *Nat. Mater.*, 15(7):775, 2016.

[151] Tobias Hanrath, Joshua J Choi, and Detlef-M Smilgies. Structure/processing relationships of highly ordered lead salt nanocrystal superlattices. *ACS Nano*, 3(10):2975–2988, 2009.

[152] Danielle K Smith, Brian Goodfellow, Detlef-M Smilgies, and Brian A Korgel. Self-assembled simple hexagonal ab2 binary nanocrystal superlattices: Sem, gisaxs, and defects. *J. Am. Chem. Soc.*, 131(9):3281–3290, 2009.

[153] Darren Dunphy, Hongyou Fan, Xuefa Li, Jin Wang, and C Jeffrey Brinker. Dynamic investigation of gold nanocrystal assembly using in situ grazing-incidence small-angle x-ray scattering. *Langmuir*, 24(19):10575–10578, 2008.

[154] Arthur RC McCray, Benjamin H Savitzky, Kevin Whitham, Tobias Hanrath, and Lena F Kourkoutis. Orientational disorder in epitaxially connected quantum dot solids. *ACS nano*, 13(10):11460–11468, 2019.

[155] Yu Wang, Xinxing Peng, Alex Abelson, Penghao Xiao, Caroline Qian, Lei Yu, Colin Ophus, Peter Ercius, Lin-Wang Wang, Matt Law, et al. Dynamic deformability of individual pbse nanocrystals during superlattice phase transitions. *Sci. Adv.*, 5(6):eaaw5623, 2019.

[156] Junfeng Wang, Zongzheng Zhou, Wei Zhang, Timothy M Garoni, and Youjin Deng. Bond and site percolation in three dimensions. *Phys. Rev. E*, 87(5):052107, 2013.

[157] Willem Walravens, Eduardo Solano, Filip Geenen, Jolien Dendooven, Oleg Gorobtsov, Athmane Tadjine, Nayyera Mahmoud, Patrick Peiwen Ding, Jacob PC Ruff, Andrej Singer, et al. Setting carriers free, healing faulty interfaces promotes delocalization and transport in nanocrystal solids. *ACS nano*, 13(11):12774–12786, 2019.

[158] Eric B. Hostetler, Ki-Joong Kim, Richard P. Oleksak, Robert C. Fitzmorris, Daniel A. Peterson, Padmavathi Chandran, Chih-Hung Chang, Brian K. Paul, David M. Schut, and Gregory S. Herman. Synthesis of colloidal pbse nanoparticles using a microwave-assisted segmented flow reactor. *Materials Letters*, 128:54 – 59, 2014.

[159] N Sh Izmailian, R Kenna, and F Y Wu. The two-point resistance of a resistor network: a new formulation and application to the cobweb network. *Journal of Physics A: Mathematical and Theoretical*, 47(3):035003, dec 2013.

[160] D. L. Staebler and C. R. Wronski. Reversible conductivity changes in discharge-produced amorphous si. *Appl. Phys. Lett.*, 31(4):292–294, 1977.

[161] H. Dersch, J. Stuke, and J. Beichler. Light-induced dangling bonds in hydrogenated amorphous silicon. *Appl. Phys. Lett.*, 38(6):456–458, 1981.

[162] M. Stutzmann, W. B. Jackson, and C. C. Tsai. Light-induced metastable defects in hydrogenated amorphous silicon: A systematic study. *Phys. Rev. B*, 32:23–47, Jul 1985.

[163] J. Melskens, A. Schnegg, A. Baldansuren, K. Lips, M. P. Plokker, S. W. H. Eijt, H. Schut, M. Fischer, M. Zeman, and A. H. M. Smets. Structural and electrical properties of metastable defects in hydrogenated amorphous silicon. *Phys. Rev. B*, 91:245207, Jun 2015.

[164] Tatsuo Shimizu, Masaki Shimada, Hidekazu Sugiyama, and Minoru Kumeda. Relation between electron-spin-resonance and constant-photocurrent-method defect densities in hydrogenated amorphous silicon. *Jpn. J. Appl. Phys.*, 40(Part 1, No. 1):54–58, jan 2001.

[165] Tatsuo Shimizu, Masaki Shimada, and Minoru Kumeda. Comparative study of defect densities evaluated by electron spin resonance and constant photocurrent method in undoped and n-doped hydrogenated amorphous silicon. *Jpn. J. Appl. Phys.*, 41(Part 1, No. 5A):2829–2833, may 2002.

[166] T. Gotoh, S. Nonomura, M. Nishio, S. Nitta, M. Kondo, and A. Matsuda. Experimental evidence of photoinduced expansion in hydrogenated amorphous silicon using bending detected optical lever method. *Appl. Phys. Lett.*, 72(23):2978–2980, 1998.

[167] Kousaku Shimizu, Tsuguhiro Shiba, Takashi Tabuchi, and Hiroaki Okamoto. Reversible photo-induced structural change in hydrogenated amorphous silicon. *Jpn. J. Appl. Phys.*, 36(Part 1, No. 1A):29–32, jan 1997.

[168] Xinwei Niu and Christopher R Wronski. The limited relevance of swe dangling bonds to degradation in high-quality a-si:h solar cells. *IEEE J. Photovolt.*, 4(3):778–784, 2014.

[169] P. A. Khomyakov, Wanda Andreoni, N. D. Afify, and Alessandro Curioni. Large-scale simulations of *a*-si:h: The origin of midgap states revisited. *Phys. Rev. Lett.*, 107:255502, Dec 2011.

[170] Reza V. Meidanshahi, Stuart Bowden, and Stephen M. Goodnick. Electronic structure and localized states in amorphous si and hydrogenated amorphous si. *Phys. Chem. Chem. Phys.*, 21:13248–13257, 2019.

[171] J. Tersoff. New empirical approach for the structure and energy of covalent systems. *Phys. Rev. B*, 37:6991–7000, 1988.

[172] Frank H. Stillinger and Thomas A. Weber. Computer simulation of local order in condensed phases of silicon. *Phys. Rev. B*, 31:5262–5271, 1985.

[173] S. Roorda, S. Doorn, W. C. Sinke, P. M. L. O. Scholte, and E. van Loenen. Calorimetric evidence for structural relaxation in amorphous silicon. *Phys. Rev. Lett.*, 62:1880–1883, Apr 1989.

[174] S. Roorda, W. C. Sinke, J. M. Poate, D. C. Jacobson, S. Dierker, B. S. Dennis, D. J. Eaglesham, F. Spaepen, and P. Fuoss. Structural relaxation and defect annihilation in pure amorphous silicon. *Phys. Rev. B*, 44:3702–3725, Aug 1991.

[175] F. Kail, J. Farjas, P. Roura, C. Secouard, O. Nos, J. Bertomeu, and P. Roca i Cabarrocas. The configurational energy gap between amorphous and crystalline silicon. *phys. status solidi (RRL)*, 5(10-11):361–363, 2011.

[176] Albert P. Bartók, James Kermode, Noam Bernstein, and Gabor Csányi. Machine learning a general-purpose interatomic potential for silicon. *Phys. Rev. X*, 8:041048, 2018.

[177] Albert P. Bartók, Mike C. Payne, Risi Kondor, and Gábor Csányi. Gaussian approximation potentials: The accuracy of quantum mechanics, without the electrons. *Phys. Rev. Lett.*, 104:136403, 2010.

[178] Albert P. Bartók, Risi Kondor, and Gábor Csányi. On representing chemical environments. *Phys. Rev. B*, 87:184115, 2013.

[179] Steve Plimpton. Fast parallel algorithms for short-range molecular dynamics. *J. Comput. Phys.*, 117:1–19, 1995.

[180] Manabu Ishimaru, Shinji Munetoh, and Teruaki Motooka. Generation of amorphous silicon structures by rapid quenching: A molecular-dynamics study. *Phys. Rev. B*, 56:15133–15138, Dec 1997.

[181] I. Štich, R. Car, and M. Parrinello. Amorphous silicon studied by ab initio molecular dynamics: Preparation, structure, and properties. *Phys. Rev. B*, 44:11092–11104, Nov 1991.

[182] K. Jarolimek, R. A. de Groot, G. A. de Wijs, and M. Zeman. First-principles study of hydrogenated amorphous silicon. *Phys. Rev. B*, 79:155206, Apr 2009.

[183] P. Giannozzi et al. Quantum espresso: a modular and open-source software project for quantum simulations of materials. *J. Phys.: Condens. Matter*, 21:395502, 2009.

[184] P. Giannozzi et al. Advanced capabilities for materials modelling with quantum espresso. *J. Phys.: Condens. Matter*, 29:465901, 2017.

[185] John P. Perdew, Kieron Burke, and Matthias Ernzerhof. Generalized gradient approximation made simple. *Phys. Rev. Lett.*, 77:3865–3868, 1996.

[186] M. Methfessel and A. T. Paxton. High-precision sampling for brillouin-zone integration in metals. *Phys. Rev. B*, 40:3616–3621, Aug 1989.

[187] Khalid Laaziri, S. Kycia, S. Roorda, M. Chicoine, J. L. Robertson, J. Wang, and S. C. Moss. High resolution radial distribution function of pure amorphous silicon. *Phys. Rev. Lett.*, 82:3460–3463, Apr 1999.

[188] Andreas Pedersen, Laurent Pizzagalli, and Hannes Jónsson. Optimal atomic structure of amorphous silicon obtained from density functional theory calculations. *New J. Phys.*, 19(6):063018, jun 2017.

[189] J. Fortner and J. S. Lannin. Radial distribution functions of amorphous silicon. *Phys. Rev. B*, 39:5527–5530, Mar 1989.

[190] Graeme Henkelman and Hannes Jónsson. Improved tangent estimate in the nudged elastic band method for finding minimum energy paths and saddle points. *J. Chem. Phys.*, 113:9978, 2000.

[191] Graeme Henkelman, Blas P. Uberuaga, and Hannes Jónsson. A climbing image nudged elastic band method for finding saddle points and minimum energy paths. *J. Chem. Phys.*, 113:9901, 2000.

[192] Aiichiro Nakano. A space–time-ensemble parallel nudged elastic band algorithm for molecular kinetics simulation. *Comp. Phys. Comm.*, 178:280–289, 2008.

[193] E. Maras, O. Trushin, A. Stukowski, T. Ala-Nissila, and H. Jónsson. Global transition path search for dislocation formation in ge on si(001). *Comp. Phys. Comm.*, 205:13–21, 2016.

[194] Erik Bitzek, Pekka Koskinen, Franz Gähler, Michael Moseler, and Peter Gumbsch. Structural relaxation made simple. *Phys. Rev. Lett.*, 97:170201, 2006.

[195] Abhijit Chatterjee and Arthur F. Voter. Accurate acceleration of kinetic monte carlo simulations through the modification of rate constants. *J. Chem. Phys.*, 132:194101, 2010.

[196] Ariel Amir, Stefano Borini, Yuval Oreg, and Yoseph Imry. Huge (but finite) time scales in slow relaxations: Beyond simple aging. *Phys. Rev. Lett.*, 107:186407, Oct 2011.

[197] RJ Freitas, K Shimakawa, and T Wagner. The dynamics of photoinduced defect creation in amorphous chalcogenides: The origin of the stretched exponential function. *J. Appl. Phys.*, 115(1):013704, 2014.

[198] D. C. Johnston. Stretched exponential relaxation arising from a continuous sum of exponential decays. *Phys. Rev. B*, 74:184430, Nov 2006.

[199] M Campos, JA Giacometti, and M Silver. Deep exponential distribution of traps in naphthalene. *Appl. Phys. Lett.*, 34(3):226–228, 1979.

[200] John T Bendler and Michael F Shlesinger. Derivation of the kohlrausch-williams/watts decay law from activation-energy dispersion. *Macromolecules*, 18(3):591–592, 1985.

[201] Stefaan De Wolf, Sara Olibet, and Christophe Ballif. Stretched-exponential a-si:h/c-si interface recombination decay. *Appl. Phys. Lett.*, 93(3):032101, 2008.

[202] Ruy S. Bonilla, Bram Hoex, Phillip Hamer, and Peter R. Wilshaw. Dielectric surface passivation for silicon solar cells: A review. *phys. status solidi (a)*, 214(7):1700293, 2017.

[203] Sara Olibet, Evelyne Vallat-Sauvain, and Christophe Ballif. Model for a-si:h/c-si interface recombination based on the amphoteric nature of silicon dangling bonds. *Phys. Rev. B*, 76:035326, Jul 2007.

[204] Sara Olibet, Evelyne Vallat-Sauvain, Luc Fesquet, Christian Monachon, Aïcha Hessler-Wyser, Jérôme Damon-Lacoste, Stefaan De Wolf, and Christophe Ballif. Properties of interfaces in amorphous/crystalline silicon heterojunctions. *phys. status solidi (a)*, 207(3):651–656, 2010.

[205] T. F. Schulze, H. N. Beushausen, C. Leendertz, A. Dobrich, B. Rech, and L. Korte. Interplay of amorphous silicon disorder and hydrogen content with interface defects in amorphous/crystalline silicon heterojunctions. *Appl. Phys. Lett.*, 96(25):252102, 2010.

[206] M. Stuckelberger, M. Despeisse, G. Bugnon, J.-W. Schüttauf, F.-J. Haug, and C. Ballif. Comparison of amorphous silicon absorber materials: Light-induced degradation and solar cell efficiency. *J. Appl. Phys.*, 114(15):154509, 2013.

[207] Jakub Holovský, Silvia Martín De Nicolás, Stefaan De Wolf, and Christophe Ballif. Amorphous/crystalline silicon interface stability: Correlation between infrared spectroscopy and electronic passivation properties. *Adv. Mater. Interfaces*, 7(20):2000957, 2020.

[208] T. F. Schulze, L. Korte, F. Ruske, and B. Rech. Band lineup in amorphous/crystalline silicon heterojunctions and the impact of hydrogen microstructure and topological disorder. *Phys. Rev. B*, 83:165314, Apr 2011.

[209] A. H. M. Smets, W. M. M. Kessels, and M. C. M. van de Sanden. Vacancies and voids in hydrogenated amorphous silicon. *Appl. Phys. Lett.*, 82(10):1547–1549, 2003.

[210] Simone Bernardini. *Efficiency-limiting recombination mechanisms in high-quality crystalline silicon for solar cells*. PhD thesis, Arizona State University, 2018.

[211] Z. Wu, L. Zhang, W. Liu, R. Chen, Z. Li, F. Meng, and Z. Liu. Role of hydrogen in modifying a-si: H/c-si interface passivation and band alignment for rear-emitter silicon heterojunction solar cell. *J. Mater. Sci. Mater. Electron.*, 31:9468–9474, 2020.

[212] P. Giannozzi et al. Quantum espresso toward the exascale. *J. Chem. Phys.*, 152:154105, 2020.

[213] Nicola Marzari, David Vanderbilt, Alessandro De Vita, and M. C. Payne. Thermal contraction and disordering of the al(110) surface. *Phys. Rev. Lett.*, 82:3296–3299, Apr 1999.

[214] `http://lammps.sandia.gov`.

[215] `https://github.com/libAtoms/QUIP`.

[216] F. Gaspari, I. M. Kupchak, A. I. Shkrebtii, and J. M. Perz. Modeling noncrystalline materials: Use of vibrational spectra as a protocol for validation. *Phys. Rev. B*, 79:224203, 2009.

[217] K. O. Bugaev, A. A. Zelenina, and V. A. Volodin. Vibrational spectroscopy of chemical species in silicon and silicon-rich nitride thin films. *Int. J. Spectrosc.*, 2012:281851, 2011.

[218] J. Tersoff. Modeling solid-state chemistry: Interatomic potentials for multicomponent systems. *Phys. Rev. B*, 39:5566–5568, Mar 1989.

[219] F. de Brito Mota, J. F. Justo, and A. Fazzio. Hydrogen role on the properties of amorphous silicon nitride. *Journal of Applied Physics*, 86(4):1843–1847, 1999.

[220] I. Štich, R. Car, and M. Parrinello. Structural, bonding, dynamical, and electronic properties of liquid silicon: An ab initio molecular-dynamics study. *Phys. Rev. B*, 44:4262–4274, Sep 1991.

[221] R. Bellisent, A. Menelle, W.S. Howells, Adrian C. Wright, T.M. Brunier, R.N. Sinclair, and F. Jansen. The structure of amorphous si:h using steady state and pulsed neutron sources. *Physica B: Condensed Matter*, 156-157:217–219, 1989.

[222] Volker L. Deringer and Gábor Csányi. Machine learning based interatomic potential for amorphous carbon. *Phys. Rev. B*, 95:094203, Mar 2017.

[223] Luman Qu, Davis Unruh, and Gergely T. Zimanyi. Percolative charge transport in binary nanocrystal solids. *Phys. Rev. B*, 103:195303, May 2021.

[224] Chase Hansen, Davis Unruh, Miguel Alba, Caroline Qian, Alex Abelson, Matt Law, and Gergely T. Zimanyi. Hierarchical carrier transport simulator for defected nanoparticle solids. *Sci. Rep.*, 11:7458, 2021.

[225] P. Lombardo, A.-M. Daré, and R. Hayn. Effect of hund's exchange on the spectral function of a triply orbital degenerate correlated metal. *Phys. Rev. B*, 72:245115, 2005.

[226] P. Werner, E. Gull, and A. J. Millis. Metal-insulator phase diagram and orbital selectivity in three-orbital models with rotationally invariant hund coupling. *Phys. Rev. B*, 79:115119, 2009.

[227] T. Kita, T. Ohashi, and N. Kawakami. Mott transition in three-orbital hubbard model with orbital splitting. *Phys. Rev. B*, 84:195130, 2011.

[228] L. de' Medici, J. Mravlje, and A. Georges. Janus-faced influence of hund's rule coupling in strongly correlated materials. *Phys. Rev. Lett.*, 107:256401, 2011.

[229] L. Huang, L. Du, and X. Dai. Complete phase diagram for three-band hubbard model with orbital degeneracy lifted by crystal field splitting. *Phys. Rev. B*, 86:035150, 2012.

[230] A. E. Antipov, I. S. Krivenko, V. I. Anisimov, A. I. Lichtenstein, and A. N. Rubtsov. Role of rotational symmetry in the magnetism of a multiorbital model. *Phys. Rev. B*, 86:115107, 2012.

[231] A. George, G. Kotliar, W. Krauth, and M. J. Rozenberg. Dynamical mean-field theory of strongly correlated fermion systems and the limit of infinite dimensions. *Rev. Mod. Phys.*, 68:13, 1996.

[232] E. Gull, A. J. Millis, A. I. Lichtenstein, A. N. Rubtsov, M. Troyer, and P. Werner. Continuous-time monte carlo methods for quantum impurity models. *Rev. Mod. Phys.*, 83:349, 2011.